SENSITIVITY OF LATTICE PHYSICS MODELLING OF THE CANADIAN PT-SCWR TO CHANGES IN LATERAL COOLANT DENSITY GRADIENTS IN A CHANNEL

SENSITIVITY OF LATTICE PHYSICS MODELLING OF THE CANADIAN PT-SCWR TO CHANGES IN LATERAL COOLANT DENSITY GRADIENTS IN A CHANNEL

By MICHAEL G. SCRIVEN, B. ENG.

A Thesis Submitted to the School of Graduate Studies in Partial Fulfilment of the Requirements for the Degree Master of Applied Science

McMaster University MASTER OF APPLIED SCIENCE (2014) Hamilton, Ontario
(Engineering Physics)
TITLE: Sensitivity of Lattice Physics Modelling of the Canadian PT-SCWR to Changes in Lateral Coolant Density Gradients in a Channel
AUTHOR: Michael G Scriven, B.Eng. (McMaster University)
SUPERVISOR: Professor John Luxat and Professor David Novog
NUMBER OF PAGES: xi, 107

Abstract

The Pressure Tube Super Critical Water Reactor (PT-SCWR) is a design with a light water coolant operating at 25 MPa above the thermodynamic critical pressure, with a separated low pressure and temperature moderator, facilitated by a High Efficiency Channel consisting of a pressure tube and a porous ceramic insulator tube. The 2011 AECL reference design is considered along with a 2012 benchmark. In the 2011 reference design the coolant is permitted to flow through the insulator. The insulator region has a temperature gradient from 881 K at the inner liner tube to 478 K at the pressure tube wall. The density of light water varies by an order of magnitude depending on the local enthalpy of the fluid. The lateral coolant density is estimated as a radial function at five axial positions with the lattice physics codes WIMS-AECL and Serpent. The lateral coolant density variations in the insulator region of the PT-SCWR cause strong reactivity and CVR effects which vary heavily on axial location due to the changes in the estimated mass of coolant and the physical relocation of the coolant closer to the moderator, as the coolant is estimated to be least dense closer to the fuel region of the coolant flow. The beta version of Serpent 2 is used to explore the lateral coolant densities in the subchannel region of the insulator in the 2012 version of the PT-SCWR. A more advanced coolant density analysis with FLUENT is used to estimate the subchannel coolant density variation, which is linked to SERPENT 2s multi-physics interface, allowing the lattice code to measure the sensitivity of the model to the analysis of the subchannels. This analysis increases the reactivity of the PT-SCWR through the displacement of the coolant. Serpent 2 is accepted as a valid lattice code for PT-SCWR analysis.

Acknowledgements

I'd like to thank my professors, Dr. John Luxat and Dr. David Novog, for the great deal of assistance and support. I would also like to thank Dr. Guy Marleau, Dr. Alex Rashkovan, David Hummel and Darryl McClure. Without them this thesis would never have been written, and would never have come to fruition. The greatest thanks are left to Sneha Bernard and my parents for their support in these trying times.

Contents

List of Figures

List of Tables

Chapter 1

Introduction and Problem Statement

The modern power generation nuclear reactor types in use today are Generation II and Generation III designs. Future conceptual nuclear reactor designs, termed Generation IV reactors, are currently in varying levels of design stages. These advanced reactors are intended for widespread deployment beyond 2030, and are being designed to meet wide ranging criteria involving enhanced safety, economics, sustainability, and proliferation resistance [3]. The Generation IV International Forum (GIF) is a cooperative endeavour intended to perform the research and development (R&D) for the advanced nuclear designs.[4]

The Pressure Tube type Super Critical Water Reactor (PT-SCWR) is a reactor design based on a light water coolant operating above its thermodynamic critical point of 22.1 MPa and 647 K. This allows for a very high thermodynamic efficiency and a direct coolant cycle, which eliminates the need for steam generators, steam separators and dryers.[5] The SCWR is a potential next generation nuclear fission reactor, which was selected for study for the Generation IV International Forum (GIF), intended to achieve enhanced safety, reliability, economics, sustainability, and proliferation resistance [6].

Atomic Energy of Canada Limited (AECL®) has collaborated with Natural Resources Canada (NRCan) and the Natural Sciences and Engineering Research Council (NSERC) to develop a pre-conceptual design of the PT-SCWR. This design is light-water cooled, with a heavy water moderator and operates using a batch fueled Plutonium/Thorium cycle. The design employs a High Efficiency Channel (HEC) concept with an outer pressure tube in direct contact with the moderator and a ceramic Yttria-Stabilized Zirconia (YSZ) insulator to provide thermal insulation of the PT from the high temperature coolant. The porous insulator region provides the necessary thermal isolation between the high temperature coolant and low temperature moderator, eliminating the need for a separate calandria tube. The design used as a basis for this thesis has a proposed insulator has a volumetric porosity of 76%, open to the coolant [7]. A more advanced design, used in chapters 3 and 5 slightly modifies this design, closing the porous liner tube, preventing the coolant from entering the insulator region. The Yttria in the insulator region in

these chapters is also removed as a simplification.[8] Table 1.1 summarizes some of the general properties of the PT-SCWR design[9].

Table 1.1: General Properties of the SCWR

Coolant	High Temperature H_2O	Fuel channels	336 vertical 5m
Moderator	D_2O	Refueling Scheme	3-cycle batch
Insulator	76% Porous YSZ	Thermal Power	2540 MW
Pressure	25 MPa	Ave Channel Power	7560 kW

The Super Critical Water Reactor has a number of major advantages through plant simplification, thermal efficiency, enhanced safety, reduced proliferation, and the usage of the Thorium fuel cycle. [4]

Plant simplification is achieved through the high outlet temperature and direct cycle, eliminating the need for steam generators, separators and dryers. This allows for a significant capital cost reduction. The nuclear steam supply system, including containment, is among the most expensive capital cost, nearly 40% of the overall costs of a plant.[10] The thorium cycle is a more sustainable option, with a multitude of advantages from increased abundance compared to uranium as well as more ideal thermal conductivity. The thorium fuel cycle is also more resistant to nuclear proliferation, as it contains the uranium isotope U-232, producing very strong gamma rays through its decay chain. This increases the complexity of producing a weapon out of U-233.[11]

1.1 General Description of PT-SCWR

Figure 1.1 is a diagram of the 78-Element fuel concept of the PT-SCWR design used as a basis for this thesis [9]. Note that the design has been updated before the release of this thesis.[8] For example, other designs exist such as a 64 element design where the coolant flows through an enlarged central pin, before returning in a double-flow configuration in the coolant region with the fuel pins, a re-entrant channel.[12] Further designs may be in development or already released, but they are not considered here. It is notable that the advanced designs utilize closed pour insulators which eliminate the lateral coolant density gradients in the insulator region. However, this thesis provides insight on the neutronic behaviour of designs with open pours in the ceramic liner.

Due to the continuous evolution of the Canadian PT-SCWR design over the last 10 years, this thesis examines two fuel channel designs that were explored by AECL over this period. The first design, used in chapter 4, permits coolant flow through

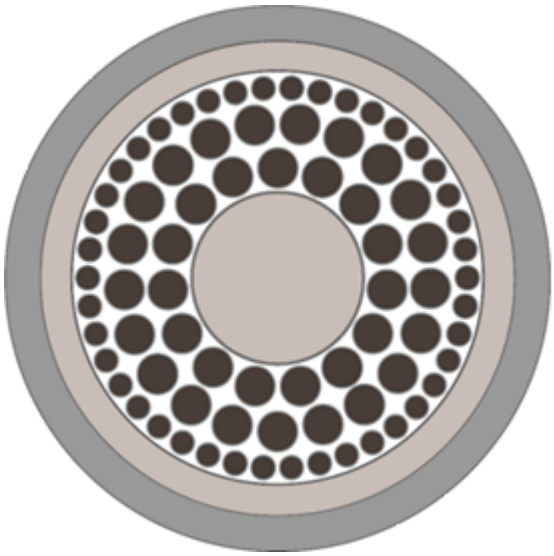

Figure 1.1: PT-SCWR 78-Element fuel concept

the porous insulator region. This design is described in the work of McDonald.[7] A conceptual paper from AECL in 2007 contains some detail of the reasoning for design decisions of these iterations of the Canadian SCWR and is a major source of much information on the earlier SCWR concepts. [1]

The fuel channel design used in chapters 3 and 5 is nearly identical but was modified to be suitable for a national code-to-code benchmark prepared by AECL. The benchmark and its activities were established to resolve some of the observed neutronic differences seen in literature for this design. It is described by AECL [8], and the results from this benchmark can be found in publications from McMaster [13] and l'École Polytechnique de Montréal [14]. The most significant change in the fuel channel design used in the benchmark is the lack of coolant in the insulator region since the liner tube is no longer porous.

The Canadian SCWR has a number of design constraints. As a result of the extremely high coolant pressure, 25 MPa, online refuelling is no longer feasible since it is not practicable to maintain that pressure with the temporary, short-term seals used by a refuelling machine. The PT-SCWR must be fuelled through batch refuelling, matching the procedure used for current boiling water reactors (BWR) and pressurized water reactors (PWR). The fuel channel are orientated vertically to facilitate batch refuelling. For designs considered here the inlet of the coolant is located at the top of the core, using an inlet plenum, with outlet feeders at the bottom of the core. The coolant flow travels with gravity in the current design. [7] Subsequent designs using a re-entrant channel utilize inlet and outlet headers which are both located at the top of the core.

Light water at such high pressures and temperatures becomes corrosive. The pressure involved in the SCWR is significant, up to 25 MPa in normal operation, and up to 625deg C. This significantly restricts the material options. There is a significant amount of materials research under way to identify appropriate materials for a variety of components in the SCWR, especially cladding for the fuel sheath. The material chosen for the works cited in this thesis uniformly use Stainless Steel 310 as the fuel cladding. Stainless Steel has superior corrosion properties in comparison Zircaloy-IV but increased neutron absorption.[7][9]

Light water is used as the coolant in the SCWR. Light water has a much higher neutron absorption cross-section than heavy water. The batch refueling adds additional neutron costs and more neutron-absorbing materials throughout the core means that the fuel must be enriched. Natural uranium is not a feasible option for the fuel. [7]

The High Efficiency Channel design is the PT-SCWR version considered for this thesis, with some modifications in chapters 3 and 5. In this design, the pressure tube is in direct contact with the moderator, unlike the modern CANDU reactor designs which protect the pressure tube with a calandria tube. The pressure tube here is partially protected from the coolant temperature with a ceramic insulator. The insulator used is a Yttra-stabilized Zirconia, which is 10 wt% Yttria and 90 wt% Zirconia (ZrO_2). The insulator reduces the amount of heat rejected to the moderator. [9][7][1].

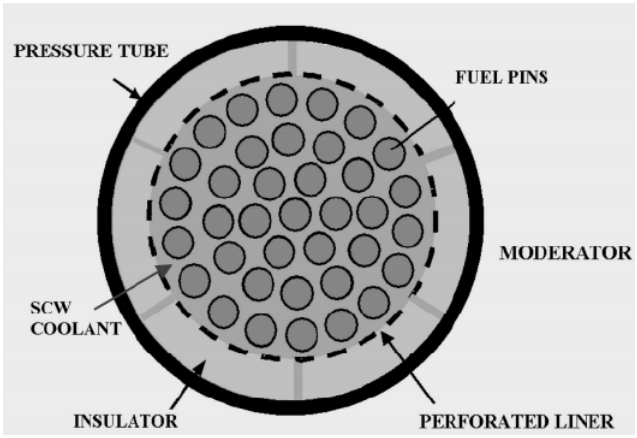

Figure 1.2: High Efficiency Channel [1]

The liner tube does not have strong material considerations, as it sees little stress in this concept. It is perforated in order to permit the flow of coolant through the insulator region. SS310 is used for the liner tube. In the initial concept used in Chapter 4, the liner tube is perforated 70%. In the design used in Chapters 3 and 5, the liner tube has no perforations, to prevent the flow of coolant into the insulator region. [1][8] Figure 1.2 displays the 2011 reference design where the Liner Tube is

perforated, permitting coolant flow in the porous insulator region.

Between the liner tube and pressure tube is an insulating material, designed to prevent heat loss to the moderator, and to absorb the majority of the temperature gradient, protecting the pressure tube. The insulator does not need to bear the weight the pressure, but does need to bear the load of the fuel bundles. The material selected is a Porous Yttria-Stabilized Zirconia (YSZ). This material has a low neutron cross-section, low thermal conductivity and a high resistance to corrosion.[1]

The insulator region is 66.6 wt% Zirconium, 7.9 wt% Yttrium, and 25.5 wt% Oxygen in Chapter 4. It is 76% porous with the porous region filled with supercritical coolant with densities that vary laterally[1]. In the benchmark-based design in Chapters 3 and 5, the Yttrium is removed from the insulator region. The pressure tube is made of Excel, a Zirconium alloy. Excel is 94.9 wt% Zr, 3.5 wt% Sn, 0.8 wt% Mb and 0.8 wt% Nb. The moderator is 99.833 wt% D_2O, with the remainder H_2O.[9]

The pressure tube is the pressure boundary, and must contain the 25 MPa of pressure in the SCWR during normal and constant operation. The pressure tube is in contact with the moderator. The work of Chow and Khartabil considers the use of a zirconium alloy named Excel, developed at AECL. It is high strength and creep resistant. It is used throughout this work as the pressure tube material.[1]

The fuel cycle selected throughout this work is the Plutonium-driven once-through Thorium cycle (OTT). This cycle is primarily described in the work of J Pencer and B Hyland at the International Conference on the Future of HWRs in 2011. This fuel mixture was determined as part of an optimization of exit burnup, CVR and lattice pitch. This mixture is therefore likely to have changed since 2011 due to multiple changes in the design of the SCWR since this optimization step. However, the fuel analyzed in this thesis is fixed and described below.[15]

The fuel is 13 wt% PuO_2 and 87 wt% ThO_2. The thorium is pure Th-232. The plutonium has an isotopic composition corresponding to recycled LWR fuel, as defined in both the pre-conceptual design and the benchmark.[2][9] Table 1.2 indicates the Pu composition

The thorium-based fuel cycle is selected by AECL as a result of the improved characteristics in safety, resource management, and proliferation resistance. Thorium Dioxide compares favourably against Uranium Dioxide, with improved chemical stability, fission product release thermal conductivity and coefficient of thermal expansion. Thorium has longer burnup characteristics, balanced against the significant downside that thorium is merely a fertile fuel, not fissile. [15]

[1] Radially

Table 1.2: Isotopic composition of Pu driver fuel derived from recycled LWR Fuel[2]

Nuclide	Weight %
Pu-238	2.75
Pu-239	51.96
Pu-240	22.96
Pu-241	15.23
Pu-242	7.10

The work of Kang and von Hippel in the journal of Science and Global Security notes a number of advantages that cause the thorium fuel cycle to have improved proliferation resistance. One of the major disadvantages of using Thorium-232 to produce U-233 as a fissile material is the appearance and decay of U-232. U-232 produces strong gamma rays through its decay chain, specifically the nuclide Thallium-208, which produce 2.6 MeV gamma rays during its decay, with a half-life of 3 minutes. [11]

The fertility of thorium can be compensated for by using a driver fuel. In this case, Plutonium is selected. The use of Pu-Th improves the sustainability of the SCWR concept, by reducing the overall need for mined uranium. [16]

The central pin is a pure Zirconia (ZrO_2) pin with a 2.82 cm radius. The fuel pins contain a homogeneous mixture of PuO_2 and ThO_2 fuel. The outermost ring of fuel pins have a smaller radius than the inner and intermediate pins. The reduced fuel pin radius is used to reduce the centreline temperature of the fuel.[17]

The liner tube between the coolant and the porous insulator is perforated (70% coolant) in the original reference model, allowing the coolant to enter the Insulator region, as seen in Figure 1.1 [1], a significant point in the analysis in Chapter 4. The liner tube is no longer perforated for Chapters 3 and 5. The liner tube and fuel cladding are both made of Zr-modified Stainless Steel 310 (SS310) throughout this thesis.

Figure 1.3 shows how the coolant properties change inside the coolant region when travelling in the axial direction, from inlet to outlet, as defined by the Pre-Conceptual design for 2011.[9] The channel power corresponds to 2540 MW, though the flow rate is not directly specified in the source material.[2]

The radial direction goes from the centre of the lattice cell to the edges of the cell. The materials in this cell, in order, are the Centre Pin, Coolant/Fuel, Liner Tube,

[2]The work of McDonald notes an approximate coolant flow rate of 1300 kg/sec from a different source.[7] This may or may not be comparable

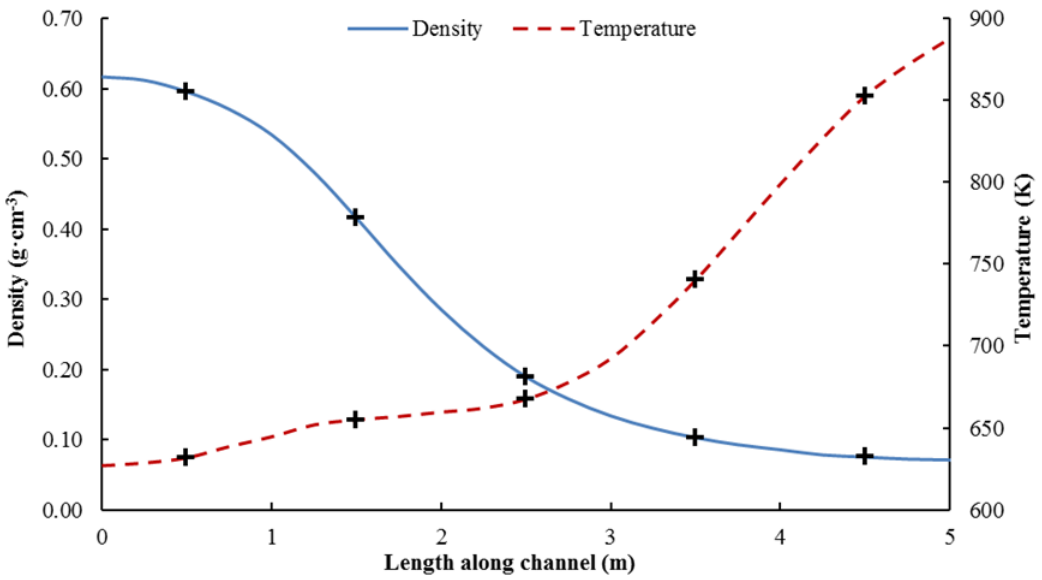

Figure 1.3: Coolant properties along length of PT-SCWR Channel

Insulator, Pressure Tube, moderator, cell boundary. The moderator is maintained at 342 K. A radial temperature gradient must exist between the inner coolant region, with temperature ranges from 600 K to 900 K, and the moderator. Chapter 4 of this thesis investigates the consequences of the resulting lateral temperature and density gradients in this insulator region. The temperature of the liner tube is assumed to match the temperature of the coolant region itself, which is described in Table 1.3. Figure 1.4 shows how the density and thermal conductivity of water changes as a function of temperature of the operating pressures of the SCWR.

Table 1.3: Position-Dependent PT-SCWR Material Temperatures

Position	Coolant/Liner Tube (K)	Pressure Tube (K)	Insulator
Position 0.5m	632.35	477.55	554.88
Position 1.5m	656.30	485.51	570.83
Position 2.5m	675.27	491.82	583.46
Position 3.5m	774.05	524.65	649.25
Position 4.5m	881.45	560.35	720.78

Table 1.4 describes the density of the coolant at each of the five axial locations considered in this thesis, as described in the 2011 pre-conceptual design. These coolant densities and temperatures are unchanged in the 2012 benchmark.

The temperature of the pressure tube and other materials is provided from the reference model [9] and described in Table 1.5. These temperatures also remain unchanged in the 2012 benchmark.

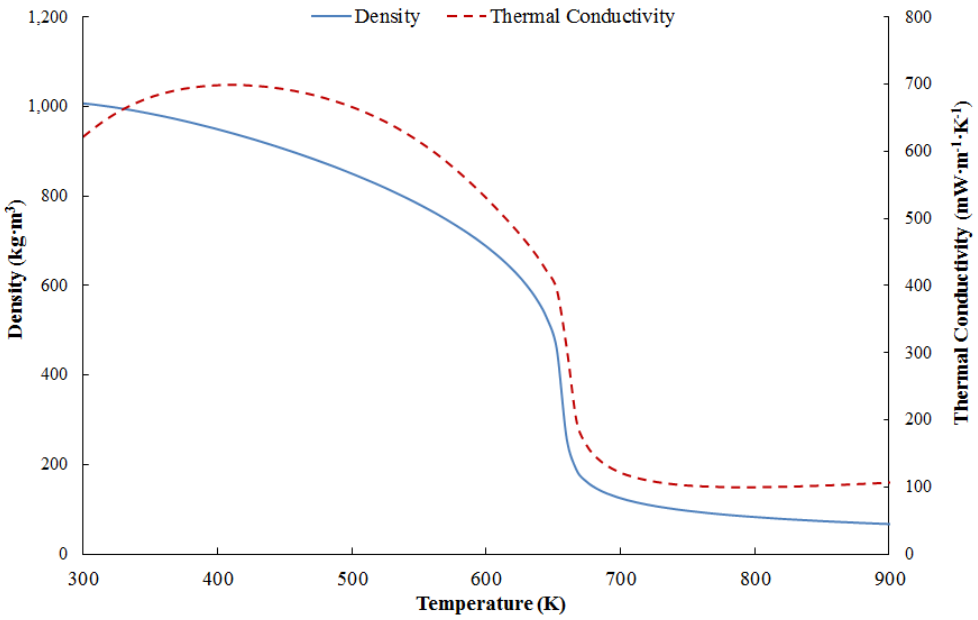

Figure 1.4: Light water density and Thermal Conductivity vs. Temperature at 25 MPa

Table 1.4: Coolant Density at 5 Axial Locations in PT-SCWR

Position	Coolant Density $\frac{kg}{m^3}$
Channel Position 0.5m	592.54
Channel Position 1.5m	382.46
Channel Position 2.5m	160.92
Channel Position 3.5m	89.49
Channel Position 4.5m	69.63

1.2 Nuclear Physics and Simulations

1.2.1 Neutron Interactions

A nuclear reactor consists of a large population of neutrons with varying energies as a function of position and time.[3] These neutrons are generated through fission events and radioactive decay. Each neutron lasts in the nuclear chain reactor for an extremely short period of time[4] and has energies that span many orders of magnitude. Over its lifetime the neutron may interact with the many nuclei in the reaction. Some of these reactions result in the capture of the neutron or elastic or

[3] Approximately 10^8 neutrons per cm^3
[4] Approximately 10^{-6}s to 10^{-4}s [18]

Table 1.5: Position-Independent PT-SCWR Material Temperatures

Material	Temperature (K)
Fuel	960.16
Moderator	342.16

inelastic scattering. These interactions can be subdivided into two major categories, scattering interactions and absorption interactions. Neutrons are removed from the system through absorption or through leakage to the exterior environment.[18],[19].

A scattering interaction occurs when a neutron interacts with a nucleus but is not permanently absorbed. Scattering collisions can be subdivided into elastic collisions and inelastic collisions which are described below. A scattering interaction does not directly influence the number of neutrons in the system.

A neutron may scatter elastically off of the nuclear potential field of an atom, being deflected with an exchange of momentum. Elastic collisions conserve the kinetic energy between the nucleus and neutron from before and after the interaction. A scattering collision which leaves the target nucleus in an excited state is called inelastic scattering. The nucleus absorbs the neutron and creates a temporary excited compound which rapidly emits a neutron.

An absorption interaction occurs when a neutron is absorbed, creating a compound nucleus. This type of reaction also has multiple types such as radiative capture, (n,2n), and fission. Absorption interactions directly influence the number of neutrons in the system.

A radiative capture involves a neutron absorption leading to an excited nucleus releases the excess energy through gamma rays or some other means, without the ejection of a neutron as a product. This results in a net loss of neutrons from the system.

A fission event is when a fissile nuclei absorbs a neutron and splits into two smaller nuclei, releasing a significant amount of energy[5] and one to four additional neutrons. This is the most significant source of additional neutrons back into the nuclear system. The neutrons produced by fission have a large energy and have a low probability of interaction with other materials. Moderator materials are used to lower the neutron energies through scattering collisions.

Some nuclei generated as fission products or the descendant of a fission product, can decay and release a neutron as part of its radioactive decay. These neutrons

[5]Approximately 200 MeV[18]

are emitted on a longer time scale than fission neutrons as they must rely on radioactive decay. Energetic photons may also generate photo-neutrons, they are generated through the absorption of a photon into a nucleus, which then emits a neutron.[18][19]

1.2.2 Cross-Sections and Materials

The previous section discussed the interactions of a free neutron with an atom. When determining these interactions it is necessary to predict the probability of each event. The ability of a neutron to interact with matter is determined by its *nuclear cross-section*,σ. The microscopic nuclear cross-section is in units of cm^2, allowing it to be approximated conceptually as an area. In fact, one might think of σ as approximately the cross-sectional area presented to a beam of incident neutrons. Another commonly used unit for microscopic cross section is barns, which equals $10^{-24}cm^2$. This cross-section can be further subdivided into cross-sections for each important reaction of absorption, fission[6] scattering, etc. [20]

A quantity closely related to the microscopic cross-section is the *macroscopic cross-section*, Σ. It is defined by Equation 1.1. It's simply defined as the microscopic cross-section multiplied by the atomic number density N.

$$\Sigma \equiv N\sigma \tag{1.1}$$

The units of the macroscopic cross-section are inverse length, cm^{-1}. It represents the probability of neutron interaction per unit path length travelled in a given material. The inverse of the total macroscopic cross-section is therefore the *neutron mean free path.*

The microscopic and macroscopic cross-sections have useful properties where they are additive algebraically. The total cross-section, microscopic or macroscopic, is the sum of its constituent cross sections:

$$\Sigma_t = \Sigma_a + \Sigma_s \qquad \sigma_t = \sigma_a + \sigma_s \tag{1.2}$$

The relation between the microscopic and macroscopic cross sections hold true for any defined cross-section of a particular reaction.

[6] σ_a and σ_f, respectively

$$\Sigma_f \equiv N\sigma_f \qquad \Sigma_s \equiv N\sigma_s \tag{1.3}$$

This can be further extended to include cross-section of different materials. For example, the total macroscopic cross-section of a material with three nuclides could be described as follows:

$$\Sigma_t = N_A\sigma_t^A + N_B\sigma_t^B + N_B\sigma_t^B \tag{1.4}$$

This cross-section can be dependant on a large number of variables, such as the energy of the incident neutron, thermal energy of the nucleus, incident direction of collision and are position and time dependent[7].

1.2.2.1 Nuclear Data Tables

The data for the cross-section of every material and interaction are stored in a Nuclear Data Library. Each cross-section is measured experimentally or through complex nuclear models.[18] Without this information, the vast number of various constant and variables in the various cross-section would be impossible to determine. There are a number of different nuclear libraries available but in this thesis the nuclear data library ENDF/B.VII is used in order to satisfy the benchmakr requirements.[8] ENDF/B.VII contains only complete and evaluated nuclear data. [18]

1.2.3 Neutron Transport Equation

The *neutron transport equation* is an exact equation for the angular neutron density throughout a system. It is the governing equation for reactor physics.

$$\frac{\partial n}{\partial t} + \nu\hat{\Omega}\cdot\nabla n + \nu\Sigma_t n(r,E,\hat{\Omega},t) = \int_{4\pi} d\hat{\Omega}\prime \int_0^\infty dE\prime\nu\prime\Sigma_s(E\prime \to E, \hat{\Omega}\prime \to \hat{\Omega})n(r,E\prime,\hat{\Omega}\prime,t) + s(r,E\prime,\hat{\Omega}\prime,t) \tag{1.5}$$

[7] An example of a positional dependence would be the number density varying with position

$\frac{\partial n}{\partial t}$ is the change in neutron density with time at a specific position, energy, direction and time

ν is the velocity of the neutron

$\hat{\Omega}$ is the direction of a neutron

∇n is the divergence of the neutron

Σ_t is the total cross-section of the neutron interactions

$n(r, E, \hat{\Omega}, t)$ is the neutron density at a given position, energy, direction and time

r is position

E is energy

t is time

Σ_s is the scattering cross section *into* the relevant energy, position and direction

$s(r, E\prime, \hat{\Omega}\prime, t)$ is neutron source covering all remaining sources of additional neutrons, such as fission, delayed neutrons and photo-neutrons.

A nuclear code, such as WIMS-AECL or Serpent must solve this equation, or an approximation of it.[19]. Such simulations are usually performed over a small region of a reactor core known as a lattice cell. Equation 1.5 can be reformulated depending on the assumptions applied to a specific case such as diffusion assumptions.

1.2.4 Multiplication Factor

The primary measure of a nuclear reaction system is its multiplication factor, or k. A multiplication factor of 1 indicates that the nuclear reactor is in perfect balance, maintaining its neutron population at a constant value as the sources balance the sinks. A multiplication factor of >1 indicates the neutron population is increasing. An operating nuclear core has a time-averaged multiplication factor of 1. This work involves the analysis of an idealized nuclear core without reactivity devices and fresh fuel, so the multiplication factor is expecting to be well above 1. There are multiple equivalent definitions for the multiplication factor, but the one used here

is as follows: [18]

$$k \equiv \frac{\text{Number of neutrons in a generation}}{\text{Number of neutrons in previous generation}} \tag{1.6}$$

Reactivity, ρ, is a quantity used to describe differences in k. When k is equal to 1, a stable state, reactivity is zero. When $k > 1$, $\rho > 0$. Both definitions are used in this thesis, and both are unit-less. A one-thousandth of each unit is defined as a milli-k (mk), but mk is used only in the context of reactivity. Reactivity is defined below in equation 1.7:

$$\rho \equiv \frac{k-1}{k} \tag{1.7}$$

1.3 Introduction to Lattice Codes

Nuclear codes used to calculated the solution to the neutron transport equation, Equation 1.5, come in many types. The two codes used in this thesis, WIMS-AECL and Serpent are deterministic and stochastic codes, respectively.

1.3.1 Deterministic Codes

A deterministic simulation produces a solution that ignores the stochastic nature of the processes and predicts a single resultant state. Running the code multiple times without any modification will result in the same result. A deterministic nuclear code must make a number of assumptions and simplifications of Equation 1.5 in order to make it deterministic and tractable.[18][19]

Energy discretization is the first simplification for a deterministic code. Instead of allowing a neutron to have continuous energies, a discrete set of energies is analyzed wherein all neutrons within the discrete energy range are treated as having the same energy. This greatly restricts the number of cross-sections and the possible energy values for each neutron. Each cross-section now only needs to be defined for each group rather than a value for every possible energy level.[19]

Spatial discretization is the second simplification. This works similarly to Energy discretization where the physical locations within a lattice cell are divided into

specific volumes and the interactions are considered on a volume average basis. The properties related to the neutron transport equation are calculated within each discrete volume.[19]

Angular discretization is the third major simplification, giving each outgoing neutron an angular momentum with a number of discrete values. [19]

1.3.2 Stochastic Codes

A stochastic code uses random sampling to solve the neutron transport equation by reducing the problem into a number of interrelated probability trees. One calculation will follow a neutron through a single branch of the probability tree. With an infinite number of simulations, the results of the probability tree can be determined with infinite precision and representative of the true distribution of neutron energy, position, angular momentum, etc. Since only a finite number of simulations are possible, the end predictions represent a sample of the true distribution, resulting in a sampling error related to the number of simulations analyzed.[19]

A stochastic code such as Serpent has the advantage of using less simplifications and yet being a much simpler individual calculation compared to a deterministic code. This had the trade-off of having a statistical uncertainty with the output of a stochastic code in addition to the typical uncertainties that result from imprecisely defined inputs. An additional trade-off is that a stochastic code typically requires a significantly increased calculation time to reduce the statistical uncertainty to a manageable level. [21][19]

1.4 Reactor Computational Analysis Codes

The two nuclear codes used in this thesis are WIMS-AECL and Serpent. These codes are validated against one another in Chapter 4 to ensure they provide comparable results for the PT-SCWR lattice cell.

1.4.1 WIMS-AECL

The SCWR lattice cell is modelled with WIMS-AECL version 3.1.2.1. WIMS-AECL is a deterministic two-dimensional neutron transport code typically used for reactor lattice cell calculations in both steady state and slowly time-variant (i.e. burnup)

systems. WIMS-AECL is capable of correcting for leakage and performing burnup steps, automatically calculating the change in fuel composition over time as a function of the lattice and power. [22][23]

The input data consists of the physical geometry along with material densities, temperatures and nuclide composition. The nuclear data used in this thesis for WIMS-AECL is taken from the E70ACR library included with this version of WIMS-AECL, based on data from the ENDF/B-VII nuclear data library [24].

WIMS-AECL was selected given the large amount of available experience with the code in Canada and at McMaster University, allowing for an easy baseline from which to compare. An example SCWR cell was provided by Jeremy Pencer in WIMS-AECL.[9]

1.4.2 Serpent

The SCWR Lattice cell is also modelled with Serpent 1.1.17 and Serpent 2.1.11 in this thesis. [21]

Serpent is a three-dimensional, continuous energy Monte-Carlo reactor physics code designed for lattice physics applications. It has a built-in burnup calculation capability to simulate fuel-depletion, which is not used in this thesis. Serpent uses the standard Monte Carlo approach to geometry definition with universes, cells and surfaces similar to MCNP and Keno-IV.[21, 25] A Monte-Carlo code was required for this thesis, as the calculation of a non-uniform lattice cell or core is performed more quickly and easily than with a deterministic code. [26]

1.4.2.1 Woodcock Delta-tracking method

The use of a continuous energy Monte Carlo methodology can result in long calculation time, especially for burnup calculations. Serpent uses the Woodcock delta-tracking method as a geometry routine to reduce the CPU time for the infinite lattice calculations [27, 28]. The method is described below using the previous citations.

Using a typical ray-tracing methodology, the geometry routine normally needs to calculate the distance between a given neutrons sampled path length and the nearest boundary surface. The path length is estimated by:

$$l_m = \frac{1}{\Sigma_{tot,m}(E)} \tag{1.8}$$

Where l_m is the estimated mean-free-path, and $\Sigma_{tot,m}(E)$ is the total macroscopic cross section of the material where the neutron is located. This equation only holds inside a given material, and must be recalculated at a material boundary. In practice, whether or not a boundary crossing has occurred it must be calculated the neutron moves within a given history.

Using the delta-tracking method, the material cross-sections are homogenized such that the sampled path lengths are valid across the geometry. This is done by introducing 'virtual collisions', a scattering reaction which does not change the neutron energy or direction, essentially a non-event. The materials cross section is not affected by the addition of virtual collisions.

A global majorant cross section, Σ_{maj} is defined to represent the total (physical+virtual) collision probability in all materials. This material is defined as the maximum material total in the system at each energy point. The path lengths sampled by the majorant are valid in all materials, eliminating the need to stop at boundary crossings. This means there is no need recompute surface distances.

$$\begin{aligned}\Sigma_{maj}(E) &= \Sigma_{tot,1}(E) = \Sigma_{tot,2}(E) = ... = \Sigma_{tot,m}(E) \\ &= \max[\Sigma_{tot,1}, \Sigma_{tot,2}, ..., \Sigma_{tot,m}]\end{aligned} \tag{1.9}$$

An additional step is required for the virtual collisions. Rejection sampling is carried out for each collision and point of collision in material m and is accepted with probability:

$$P_m(E) = \frac{\Sigma_{tot,m}(E)}{\Sigma_{maj}(E)} \tag{1.10}$$

If the point is not accepted, it is treated as a virtual collision and a new path length is sampled. This sampling allows for a rapid calculation in a complex environment, such as a material with changing cross-sections. Tracking is faster in complex geometries, which matches the description of the PT-SCWR. This is relevant for the treatments performed in Chapters 4 and 5. The downsides of this sampling method involve efficiency issues with low-density regions when the majorant cross-section is very high, such as in the presence of strong absorbers.

1.4.3 Serpent 2

Serpent 2 is an advanced beta version of Serpent, intended for a public release in late 2014 [29]. This beta version contains a multi-physics interface which permits the usage of the output of a thermal-hydraulics code as a spatial input. This multi-physics interface allows Serpent to perform sub-channel physics analysis and be coupled with a thermal-hydraulics code. An arbitrarily fine mesh of coolant densities can be imported into the geometric definition of the cell.

As noted in the previous section, an arbitrarily fine mesh can be used without having to stop at each individual surface. This permits Serpent 2 as an excellent code with which to perform this analysis which would be overly computationally expensive without the Woodcock tracking model.

1.5 Computational Fluid Dynamics Analysis

Subchannel analysis refers to the coolant density variations in between the individual fuel pins in the coolant region of a nuclear reactor. While it is often a useful assumption in reactor physics to assume that this region has a constant lateral density, the effect of considering the non-uniform density of this region may be worth considering. This may be of particular importance for SCWR as the density is very sensitive to temperature near the pseudo critical transition temperature. It is this consideration that forms the basis of Chapter 5.

The coolant density variations in this region are a function of the heating of the coolant from the fuel cladding, flow along the channel, and the mixing of the coolant between subchannels. Often dedicated subchannel codes such as COBRA-TF are used to calculate subchannel information. An excellent discussion in more detail about subchannel analysis can be found in the work of Lokuliyana. However subchannel codes predict average properties within each subchannel and actual density distributions may deviate significantly from this average near the pseudo critical point. Therefore for this work detailed density gradients are predicted using Computational Fluid Dynamics codes. [30]

The detailed thermal-hydraulics analysis performed as an input for this thesis was done using the CFD code FLUENT. These results are not validated entirely and are used largely as a proof-of-concept for the thesis.[31] Future work should likely involve more strongly coupling the CFD predictions with the neutronics. The CFD analysis performed is described in Chapter 1.5, though not all details are available

in this thesis[8].

Chapter 5 uses Computational Fluid Dynamics analysis results as an input into the lattice code Serpent 2. The CFD calculation determines the lateral density variations of the coolant in the coolant region of the SCWR. Chapter 5 uses this lateral density variation to determine the significance of including this analysis as part of the neutronics calculation for this design. The CFD code Fluent is used for this analysis. The subchannel coolant density was computed by Dr. Rashkovan, a visiting professor at McMaster University from the Nuclear Research Center NEGEV (NRCN). The details of the simulation are provided below as described by personal communication with Dr. Rashkovan.[31]

The simulation is performed at a steady-state 100% Power, assuming thermally expandable incompressible water. The water properties are determined using mini-REFPROP. Arguing from symmetry, only a 1/6th radial slice is modelled. An RNG k-epsilon turbulence model with standard wall functions and constant turbulent Prandtl number were used. The inlet temperature used is 623.15 K with a uniform mass flux at the inlet of 869.6 $\frac{kg}{m^2 s}$.

Figures 1.5 and 1.6 are preliminary results created by Dr. Rashkovan in Star-CCM+, showing the preliminary lateral density distribution structure in the subchannel of the SCWR bundle studied in this thesis.

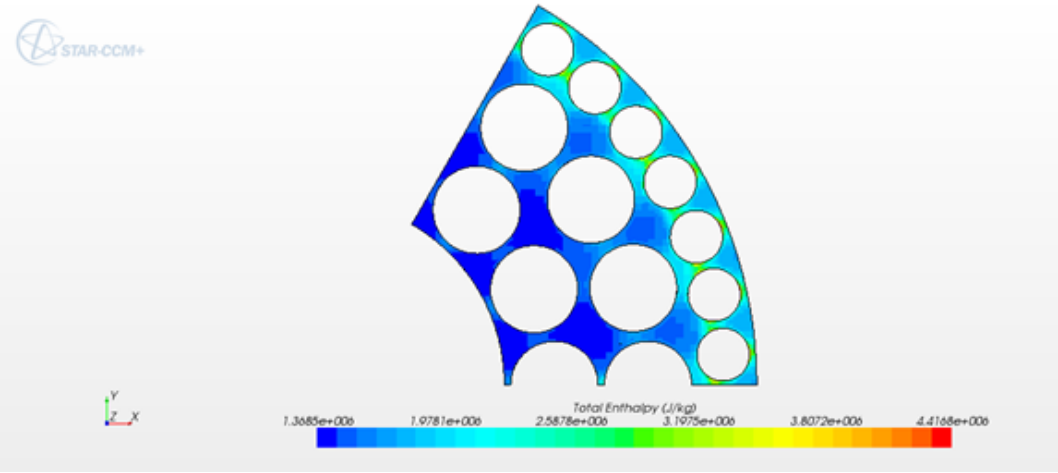

Figure 1.5: Example image of subchannel density variation at z=2m, 100% power in Star-CCM+

MATLab scripts were used to parse the FLUENT data into the required format for SERPENT input. The re-formating was done in 2 stages to allow for intermediate

[8]The work in the CFD model for FLUENT was not performed specifically for this thesis, and was necessarily recorded in sufficient detail for replication

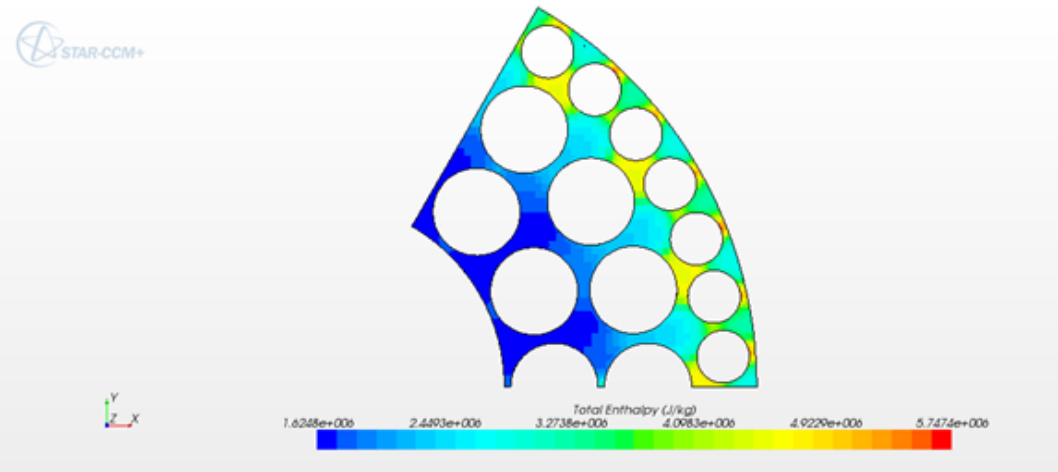

Figure 1.6: Example image of subchannel density variation at z=4m, 100% power in Star-CCM+

verification. One script trims the input data to just the geometric position and coolant density of the points that are used in Serpent 2. A second script is used to finalize the formatting.The scripts are included in Appendix A

1.6 Problem Statement

This thesis contains a number of sections related to different aspects of the coolant density of the PT-SCWR design. A benchmark was proposed by AECL [8] in July 2012 to resolve noted discrepancies in the $k_{infinity}$ of the reference model between several nuclear codes, including WIMS-AECL and Serpent. In Chapter 3, Serpent is used to model the benchmark input files. The results are compared against several codes including Dragon 3.06, MCNP5, WIMS-AECL, and KENO.[13] The Serpent results from l'École Polytechnique de Montréal [14] are compared and contrasted with the results obtained in Serpent in this thesis.

In Chapter 4 the lateral density distribution of the coolant water in the porous insulator region is estimated from simple thermal properties. This impact on lattice level neutronics of this modified lateral coolant density distribution is compared against the reference model, with a uniform coolant density in the insulator region. This analysis is performed with the lattice codes WIMS-AECL and Serpent.

In Chapter 5 the density gradient in the coolant region is taken from a Computational Fluid Dynamics (CFD) sub-channel analysis. Using the beta lattice code Serpent 2, the effect on the lattice level neutronics due to the subchannel density

fluctuations is calculated. The strength of Serpent is used here, as a Monte-Carlo code is more suited to the strongly non-uniform coolant region. This chapter uses the same geometry as found in Chapter 3.[26]

Chapter 2

Literature Review

This chapter reviews a selection of literature regarding the various topics considered in the problem statement.

2.1 Neutronics in the SCWR

There have been multiple papers produced on various aspects of simulating the neutronics of the Canadian SCWR. Due to the many different variations of the SCWR that have been proposed, much of the available literature on SCWR neutronics often involves a different variation of the SCWR cell. Multiple lattice physics papers use Serpent as one of the examined codes.

One of the previous versions of the PT-SCWR is the 54-element version of the PT-SCWR in 2010, where each fuel element is identically sized.[32]. The work of Shen is a core-level analysis of the PT-SCWR using Serpent and MINER, with comparison to work in WIMS-AECL and RFSP. This work finds that the key elements of SCWR core design include power distribution, peak channel and bundle powers, and core reactivity coefficients in both steady-state and accident conditions. This work is focused on core-level analysis, but notes weaknesses in the single-lattice cell analysis, as each cell interacts heavily with its neighbours, indicating a need for multi-cell neutron transport solutions. The batch refuelling of the SCWR using the same fuel bundle in three stages of loading, reducing the utility of a single-cell lattice in full-core considerations. Calculations of a single lattice cell is not sufficient to describe the lattice cell properties in a full-core model. It is also found that the lattice code Serpent is an appropriate tool for the assessment of reactor-physics methods for use in SCWR analysis.[33] The work of Shen, notably, assumes a wholly constant coolant density throughout the 2D axial slice. The possible coolant density variations are not considered.[33]

The importance of calculating pin power profiles in discussed in the work of Grcić. It shows that Serpent 1.1.16 and DRAGON 4.03 can vary significantly in a number of different considerations. It uses the maximum relative pin power, diffusion coefficient and a pin power distribution in order to characterize the pin power profile.

the pin power profiles can vary dramatically when the $k_{infinity}$ calculations are strong matches for each other, showing that reactivity alone is not a sufficient descriptor of a lattice cell analysis. It concludes that a minimum of 5000 neutrons per cycle is necessary in order to sufficiently characterize the pin power profile in Serpent, though this work only uses 500 cycles. This work is based off a 16×16 Fuel assembly, typical of the European SCWR design, which may have little relevance to an SCWR cell. [34]

The 2013 work of Pencer et al "Core Neutronics for the Canadian SCWR Conceptual Design" from AECL if based off of more recent[1] of a High Efficient Re-Entrant channel design of the PT-SCWR. The geometry is a significant departure from the pre-conceptual design discussed in this thesis, the most notable changes are solid insulator and an inner central coolant tube which separates the coolant as it first enters the lattice cell downwards, and then flows upwards in the fuel and coolant annulus region. This work assumes minimal heat transfer into the central coolant flow tube, combined with the lack of a porous insulator region results in no major lateral coolant density variations outside of the subchannels. In order to perform subchannel analysis on this concepts, grid spacers and wire wrap would need to be considered. The calculation is performed on a core-level in agreement with the work of Shen of the importance of core-level analysis for well-defined boundary properties. $k_{infinity}$ and CVR are the major neutronic properties calculated by AECL to establish the properties of the lattice cells outside of burnup calculations. The power profiles of each lattice cell in the core are also calculated, along with the Linear Element Ratings in each lattice cell. [16]

The aforementioned paper by Pencer at al[16] removed the porous insulator region from the PT-SCWR design. This was in part based on preliminary results from this thesis, presented at the 3rd China-Canada Joint Workshop based on work that is now Chapters 4.1-4.2.1 of this thesis.[35] These preliminary results filled an important niche within the literature that was not available elsewhere.

The 2012 presentation by Hummel et al[36] uses DRAGON 3.06 on the 78-element fuel bundle considered in this thesis in order to optimize the parameters of the lattice cell. This work emphasizes the importance of finding a slightly negative CVR for a given lattice cell. A negative CVR is a major goal of the PT-SCWR design as it causes the reactor to tend towards shut-down during a Loss of Coolant Accident (LOCA). However, an overly negative CVR can lead to instability and control issues.[32] The maximum Linear Element Rating is also an important concern, as the integrty of the cladding is a concern above $40\frac{kW}{m}$.[7] As an optimization process, 1569 unique DRAGON models were simulated over three optimization, further demonstrating the value of finding optimal methods to determine properties of a lattice cell, as optimization studies can consist of a large number of individual simulation runs.

[1] 2012 and onwards

The 2012 paper by Marleau and Harrison of l'École Polytechnique de Montréal for PHYSOR 2012 uses the older 54-element PT-SCWR design.[32][37] This paper uses the lattice codes DRAGON 3.06 and Serpent, in particular using the `endfb70` library for Serpent. This paper uses 10000 neutrons per cycle, and again only 500 cycles. The material temperatures were adapted to the nearest 300 K in order to simplify the model as much as possible. Serpent, unlike DRAGON, does not need to subdivide the fuel rods in order to account for self-shielding. The differences between DRAGON and Serpent are suggested to be mostly due to the zirconium present in the insulator region.

It is notable that no papers of the neutronics of the PT-SCWR design with the porous insulator region discuss or consider the effects of the temperature gradient the potentially supercritical coolant would be subject to. In this respect, this thesis is investigating a unique consideration of this older PT-SCWR design.

2.2 Coolant Density Variations

This section discusses literature which considers the effects of subchannel density gradients on lattice physics analysis.

The work of Shan et al [38] uses a coupled neutronics/thermal-hydraulics analysis in the 43-element PT-SCWR using the lattice code MCNP and the subchannel code ATHAS. This work uses a total of 70 subchannels bounded by the cylindrical fuels rods and open gaps. This work doesn't consider the coolant density variations within a subchannel, simply the coolant density variations between subchannels.

The work of Ahmad et al [39] uses the 62 element re-entrant type of PT-SCWR. The coolant flows downward through a central flow tube, and upwards through the space between the fuel pins. This work considers the change in coolant density in an axial direction within the downward central coolant channel. This central coolant channel variation is only 15°C, but it has a strong effect on the properties of the reactor. Consideration of this 15°C change decreasing the outlet temperature of the reactor by up to 7°C due to the heat flux to the coolant in the central fuel region.

The work of Jareteg et al investigates the creation of a fine-mesh solver for a coupled neutronics/thermal-hydraulics simulation for a steady-state PWR design based on Serpent, OpenFOAM and SALOME. The simulation uses 800 cells per fuel pin at each axial position, allowing a calculation of the heterogeneity of the coolant in the PWR fuel assembly. The same mesh for both the neutronics and thermal-hydraulics modelling. The difference between the coarse-mesh and fine-mesh modelling can result in discrepancies of up to 0.5% in pin power and tens of

pcm. This paper finds that homogenizing of the moderator results in zero change in the neutronics of the reactor, with the $k_{infinity}$ both with and without a bulk moderator to be unchanged. The fuel assembly used has no distinction between the coolant and moderator.[40]

This suggests that the considerations of the coolant density variations in the coolant region may not be significant. However, the PT-SCWR has a huge number of design differences from the fuel assembly used, such as super-critical fluid and a separated moderator.[40]

The work of Feng et al uses a neutronic/thermal-hydraulic coupling scheme with the lattice code WIMS-AECL and subchannel code ATHAS to optimize a 54-element PT-SCWR design. The pitch-circle radius of fuel rings are optimized. The lattice cell considered uses a porous liner tube and insulator region. However, this work only considers the ability of the insulator to draw heat out of the coolant and into the moderator through the pressure tube as a factor for the subchannel analysis. The effect of subchannel coolant density gradient on the neutronics of the SCWR is not isolated or compared with a reference case without coupling. This paper additionally notes that consideration of the subchannels can elevate the peak cladding temperatures.[41]

The paper presented by Liu et al, "Coupled neutronics/thermalhydraulics analysis of PT-SCWR fuel channel"[42] performs a coupling analysis of the PT-SCWR 78 element fuel channel concept used in this thesis using MCNP and ATHAS. This work assumes that the coolant in the porous liner tubes and insulator regions are not recalculated by the subchannel code, they remain as originally defined. The subchannel code performs calculations on the 132 subchannels in the coolant region. MCNP is a stochastic lattice code like Serpent. The coupling was effective. This paper attempts to optimizae some factors in the 78 element fuel bundle such as lattice pitch and fuel enrichment. Having different fuel enrichments in different fuel rings is explored, finding neutronic value in this process.

Another paper by Liu et al, "Core and sub-channel analysis of SCWR with mixed spectrum core" uses a mixed spectrum version of the SCWR, termed the SCWR-M, to perform core and sub-channel analysis with a coupled neutronic and thermal-hydraulic analysis. This work focuses on the properties of the SCWR-M, but it compares the results with the coupled subchannel analysis against a reference homogenized model. The analysis with the subchannel has a nearly identical moderator temperature, but a maximum cladding temperature that is 350°C higher than the reference maximum cladding temperature. This is likely a result of the super-critical water reducing its density against the fuel pins more rapidly when portions of the coolant are permitted to cross the pseudo-critical point. The maximum fuel temperature in the fast neutron zone also increases by over 700°C.[43]

The work of Liu et al does not compare the neutronics results of the reference model versus the subchannel model, but it is clear that the changes may be significant, but it is not explored.[43]

The work of Jareteg et al performs an analysis similar to what is desired, a reference model with a bulk fluid consideration compared against a calculated subchannel analysis (with the same average bulk fluid density), but only performs this consideration for the downward central coolant flow. The results are minimal, but indicate the lack of directly comparable research. The work of Liu performs this consideration for an entire core, but does not discuss the neutronics of the situation. Again, this work is very similar, performing the desired goals similarly, but not as a direct analogue.

The work of Churkin and Deev demonstrates the complexities in using subchannel codes to calculate the density of the supercritical water. It shows that the nonlinear heat transfer correlations such as for the Reynolds number and Pradntl number can result in ambiguous solutions. In these ambiguous solutions, the calculated wall temperature may be possible with the same values of heat flux and averaged parameters of flow and liquid. The solutions to these cases are solved with additional equations and approximations including additional variables, which must be iterated upon. The significance is a fine-mesh subchannel simulation may be increasingly computationally expensive. Coupled neutronic/thermal-hydraulic codes requires multiple iterations of the same mesh so the computational time is an important constraint.

2.3 Summary

There are a couple of major conclusions of this review of literature. There is a body of work involving the lattice physics considerations of all variations of the PT-SCWR. However, none of the reviewed papers discuss the coolant density variations in a porous insulator region in the PT-SCWR.

Firstly, there are a large number of SCWR papers that discuss a coupled neutronic and thermal-hydraulic analysis. However, the discovered papers do not discuss the ramifications of the subchannel coolant density gradients themselves. Instead the focus of these papers is on the successful coupling of the neutronics and subchannel codes, where the actual coolant density variations and magnitudes are not discussed, the positional variation of the coolant within the subchannels is not a factor. In this regard, this thesis is unique. This is indicated by the citations of the preliminary results by Atomic Energy of Canada Limited. Secondly, Serpent is used in a number of different lattice physics papers, including in SCWR analysis. It is

uniformly accepted as a useful lattice physics code for SCWR analysis.

There is a body of work in coupled neutronic and thermal-hydraulics analysis that is very similar to the space in which this thesis is investigating. The lack of literature comparing the SCWR with a bulk fluid temperature and a fine-mesh subchannel analysis indicates value in the work performed in this thesis. No research was discovered discussing the coolant density variations in a porous insulator region which divides the area between the coolant and the separated moderator. Where subchannel analysis is performed, the importance of the density of the mesh is not heavily discussed. The investigations in this thesis are relatively unique, and directly related previous work is difficult to identify.

Chapter 3

Benchmark

A benchmark was proposed by AECL and McMaster University [8] in July 2012 to resolve noted differences in the reactor physics predictions for the reference model between WIMS, Serpent and other codes. It examined the sensitivity of $k_{infinity}$, as well as differences in predictions of the maximum linear element ratings (LER). The scope of this chapter is to use Serpent and Serpent 2 to benchmark against the others used in the benchmark.

In this thesis results are generated using Serpent 1.1.17 and Serpent 2.1.11 and compared against several codes including DRAGON 3.06, MCNP5, KENO and WIMS-AECL. The results from McMaster University [13] and l'École Polytechnique de Montréal [14] are compared and contrasted with the results obtained in this thesis.

3.1 Benchmark Specifications

The benchmark specifications are available in the description provided by AECL [8]. A number of details are provided below for context.[13]

The geometric and material definitions in the benchmark are updated from the definitions used in the pre-conceptual SCWR design. Yttrium is not present in many of the libraries used in the benchmark so it is removed from the material definitions. The liner tube has no perforations. The insulator material is without any coolant flow while remaining porous. No material replaces the coolant in this region.

The coolant and other material densities remain identical compared to the pre-conceptual reference model; the coolant is defined for a temperature at 600 K or 900 K. This uniformity of temperature is selected in order to minimize the amount of Doppler broadening and interpolation calculations performed, limiting the number of parameters of each code being compared in the benchmark.

An exit burnup fuel composition is provided in the benchmark for usage in

calculations, so each participant is using identical burnup fuel. The burnup fuel composition varies within each of the three fuel rings, but each axial location has identical fuel burnup.

The lattice is simulated with two major perturbations, calculating the Coolant Void Reactivity (CVR) and the Fuel Temperature Reactivity Coefficient (FTC). The CVR is measured by reducing the coolant density to 1 $\frac{kg}{m^3}$. The FTC is measured by increasing the fuel temperature by 300 K, though it is calculated per 100 K.

The calculations are performed at three different power levels: Hot Full Power (HFP), Hot Zero Power (HZP) and Cold Zero Power (CZP). HFP is measured at a power density of 29 $\frac{W}{g}$ of initial heavy elements. At HZP, all non-moderator materials are set to 600 K and the coolant density is uniformly defined as the inlet density of 592.54 $\frac{kg}{m^3}$. At CZP, all materials are set to 300 K and the coolant density is uniformly defined as 996.567 $\frac{kg}{m^3}$. The CZP and HZP models have no variation in properties in the axial direction, so only one axial position is simulated.

The Linear Element Rating (LER) is calculated in Serpent by tallying fissions in each fuel element. The value is normalized assuming a total power of 1512.56$\frac{kW}{m}$ per bundle.[13] The benchmark in Serpent is calculated using 5000 generations and 5000 neutrons per generation, along with 300 additional unrecorded generations that are used to allow the Monte-Carlo simulation to approach the steady-state.

3.2 Benchmark Results

The first section of the Benchmark compares Serpent 1.1.17 against the other codes used by McMaster researchers, DRAGON 3.06K, KENO V.a and VI, WIMS-AECL 3.1 and MCNP5 [13].

In Figures 3.1 and 3.2 Serpent 1.1.17 largely trends with the other codes in the Benchmark. In Figure 3.1 reactivity difference between the first and second axial positions is much greater than for the other studied codes. This positive reactivity bias is also apparent using the exit burnup fuel in Figure 3.2.

While Serpent can be used to determine trends, an error was generated that could not be traced to a solution, leading to a change in code version partway through this work. The error is quoted below:

> Conflicting reaction type in 1 fission channels. Serpent treats the reaction as fission (mt 18-21 or 37), but the type number in the TYR block

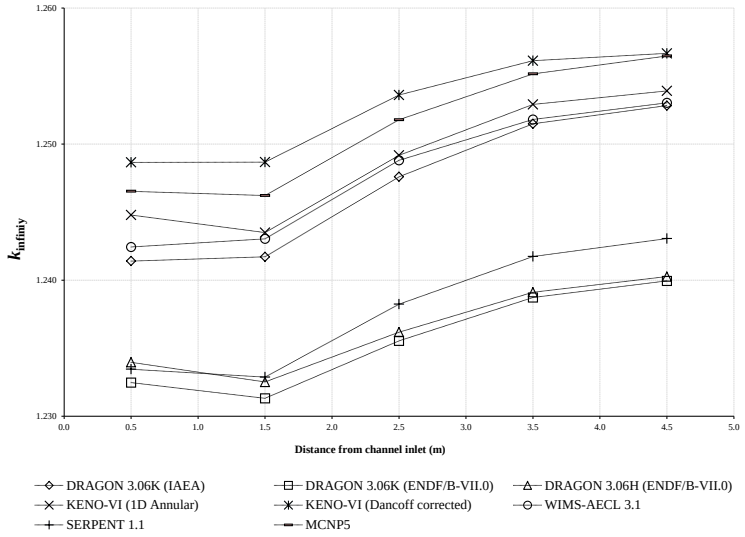

Figure 3.1: Benchmark k_{inf} results for fresh fuel

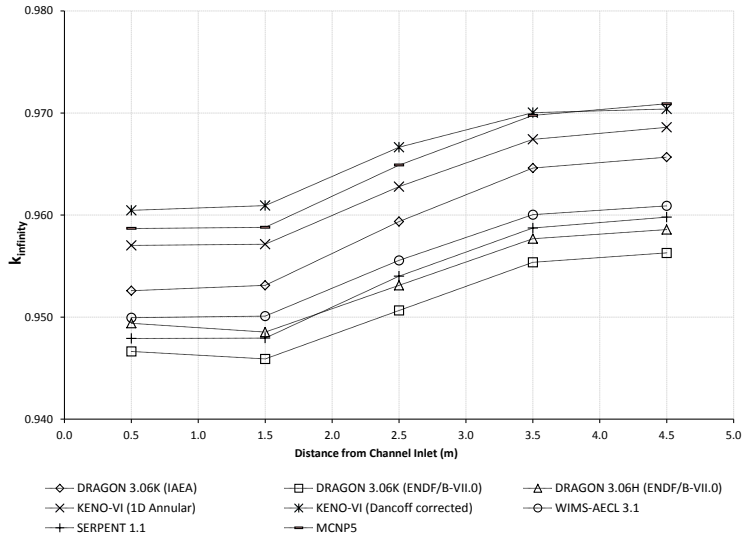

Figure 3.2: Benchmark k_{inf} results for exit burnup fuel

suggests that the channel should be handled as absorption. This may cause significant discrepancies in code-to-code comparisons.

This error code could is specific to Serpent version 1.18 and earlier. It does not appear in Serpent 2. Since this problem is corrected in Serpent 2, and comparisons show close agreement between the two version of Serpent, it is expected that this error did not significantly impact the simulations.

Of note in Figures 3.1 and 3.2 is that many codes identify different trends in whether reactivity increases or decreases with the initial coolant density changes from position 0.5m to 1.5m. Some of the studied codes indicate a slightly negative reactivity trend, but all the codes show a small trend initially. Serpent 1.1.17 behaves most similarly with DRAGON 3.06K and H with the ENDF/B-VII.0 library.

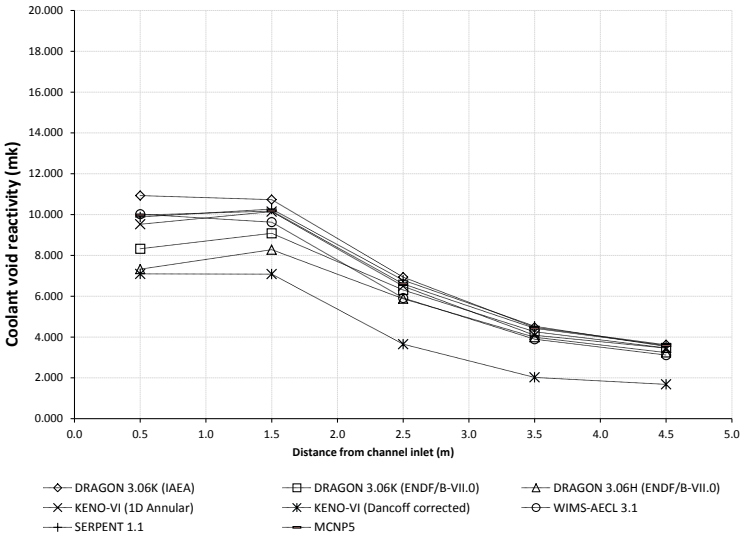

Figure 3.3: Benchmark CVR results for fresh fuel

Figures 3.3 and 3.4 contain the results for voiding the coolant within of the lattice cell. Serpent 1.1.17 tracks very closely to the general trend of all the codes listed. It tracks on the higher end of calculated CVR. Like many of the other codes, it shows a small positive trend in the CVR between the first and second axial positions.

In Figures 3.5 and 3.6 Serpent has reasonably comparable results to that of the other codes in terms of the estimated FTC at both zero and exit burnups. In Figure 3.5 Serpent has one the highest FTC of the codes and increases with the axial position. All the codes, in aggregate, show a general increase in FTC with axial position, but Serpent 1.1.17 has a stronger trend. In Figure 3.6 Serpent shows a more uniform trend than KENO and WIMS-AECL, but it has an even stronger increase in FTC with axial position. The smoothness of the trendlines in these

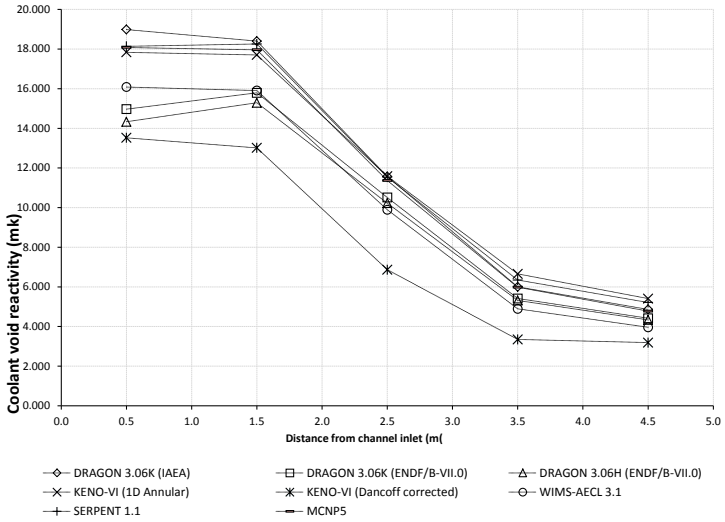

Figure 3.4: Benchmark CVR results for exit burnup fuel

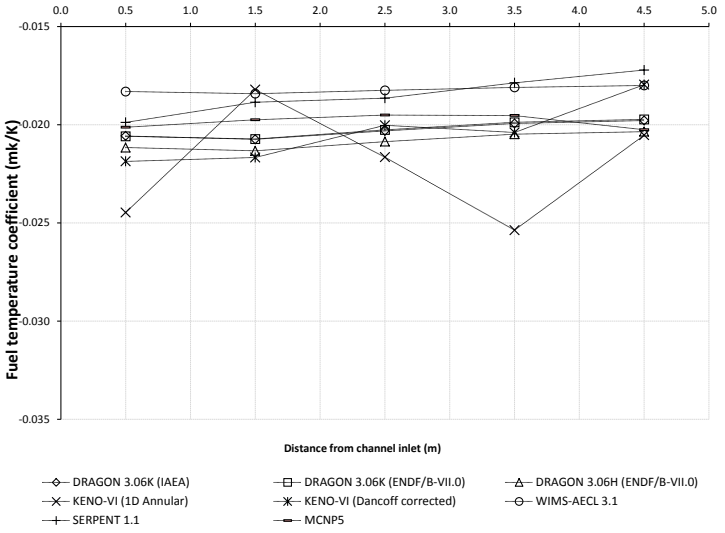

Figure 3.5: Benchmark FTC results for fresh fuel

figures suggests a real trend. Serpents treating of the temperature-dependence of the nuclide cross-section has an appreciable effect on the results, as a mild outlier

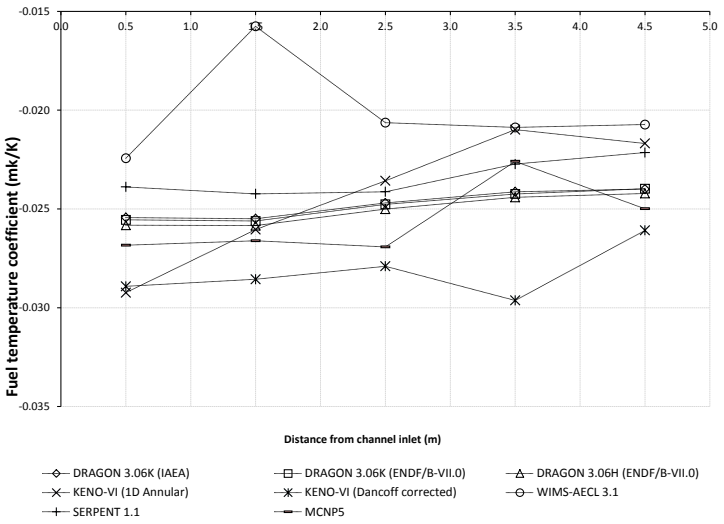

Figure 3.6: Benchmark FTC results for exit burnup fuel

from the aggregate.

Figures 3.7-3.12 show the Linear Element Ratings in $\frac{kW}{m}$ for each of the three rings of fuel. The Linear Element Ratings is calculated at a power level of $1.513\frac{\mathrm{MW}}{\mathrm{m}}$. The three rings of the fresh fuel are presented first, followed by the three rings of the burned fuel. Note that the outer ring has a smaller fuel radius than the inner and middle rings (0.35 cm vs 0.62 cm) though the cladding thickness remains constant at 0.06 cm.

The three rings for the fresh fuel are represented in figures 3.7-3.9. Figure 3.7 reveals that Serpent 1.1.17 tracks very closely to the LER results of WIMS-AECL and Dragon. Serpent has a similar dependence on axial position for the Linear Element Rating. Serpent with fresh fuel provides no real contrast between WIMS-AECL and Dragon.

Figures 3.10-3.12 are the Linear Element Rating simulation results for the exit burnup fuel for each of the codes. The trend seen in the fresh fuel continues for the burnup fuel, where Serpent tracks closely with both Dragon and WIMS-AECL. Serpent 1.1.17 appears to be well-within reasonable consideration as a nuclear lattice code for the purposes of the SCWR project.

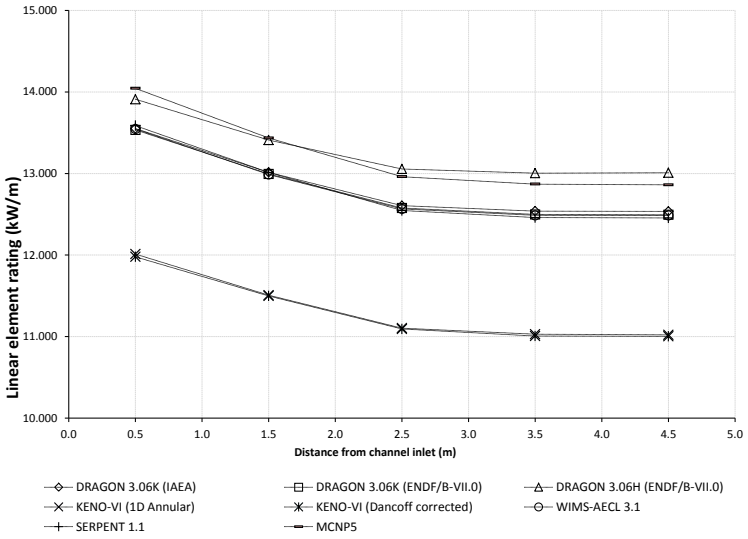

Figure 3.7: Benchmark LER results for the inner ring of elements of fresh fuel

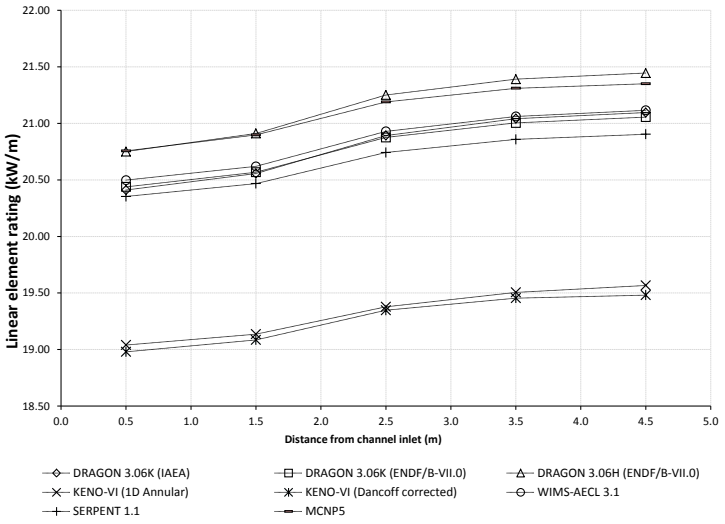

Figure 3.8: Benchmark LER results for the middle ring of elements of fresh fuel

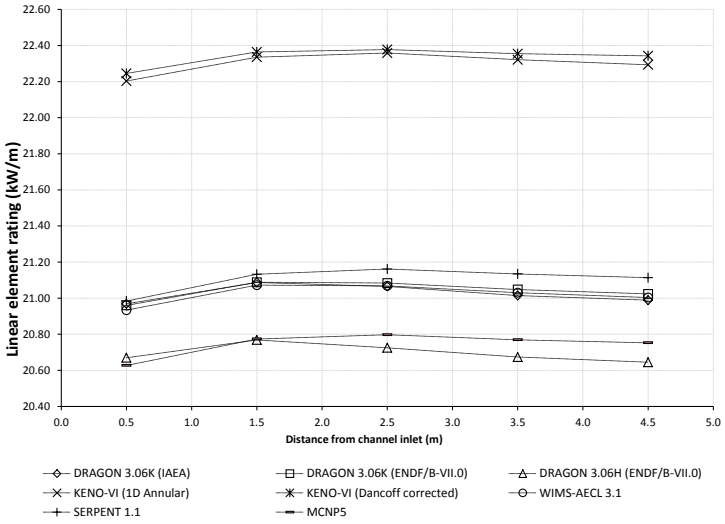

Figure 3.9: Benchmark LER results for the outer ring of elements of fresh fuel

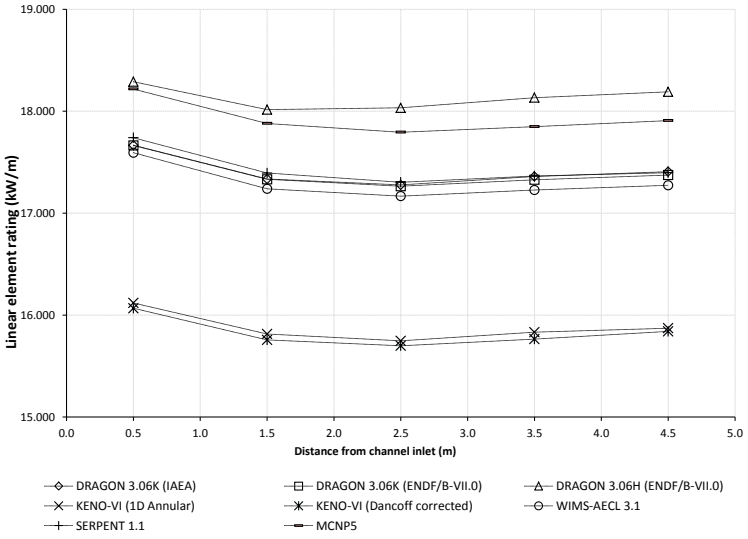

Figure 3.10: Benchmark LER results for the inner ring of elements of exit burnup fuel

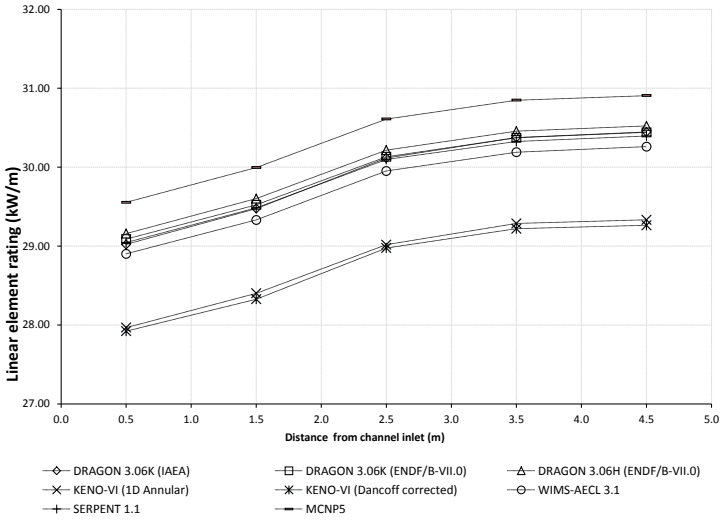

Figure 3.11: Benchmark LER results for the middle ring of elements of exit burnup fuel

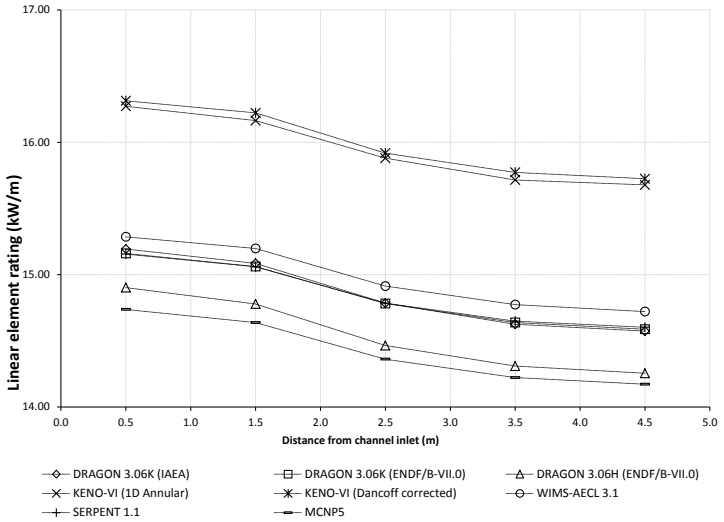

Figure 3.12: Benchmark LER results for the outer ring of elements of exit burnup fuel

3.3 Benchmark Comparison of Various Serpent Results

It is not enough to compare the work of Serpent 1.1.17 against the other codes of the benchmark. Given the availability of the beta version of Serpent 2, the benchmark results are re-simulated with Serpent 21.11, to determine if this beta version generates any significant differences from Serpent 1.1.17. The work done here is not the only work done with this benchmark in Serpent 1.1.17. Dr.Guy Marleau at l'École Polytechnique de Montréal also simulated this benchmark.[14] Therefore, the results here must also be compared against Dr. Marleau's work, to ensure that any discrepancy is not solely due to user or other error.[1]

The previous figures 3.1-3.12 are recreated below, with only the three data series of Serpent 1.1.17 from this thesis, Serpent 2.1.11[2] and the Serpent 1.1.17 calculations from l'École Polytechnique de Montréal[3]. The y-axis of each chart is maintained from the version to provide a sense of scale against the previous benchmark data charts.

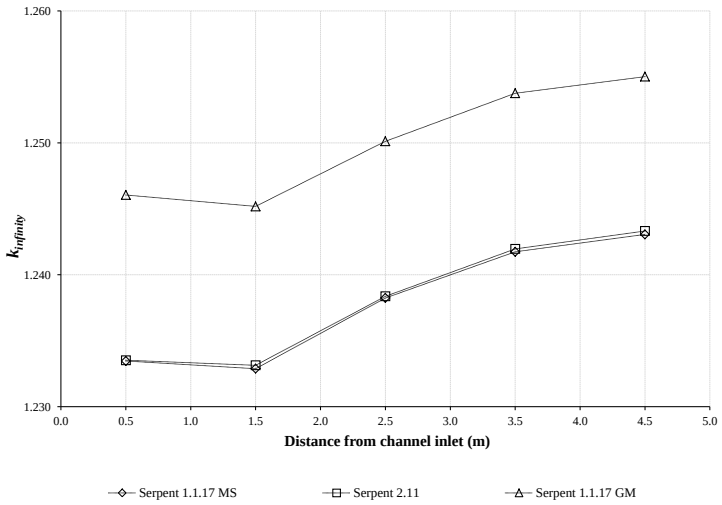

Figure 3.13: Serpent Benchmark k_{inf} results for fresh fuel

[1]Dr. Marleau was kind enough to provide the input files used in his group, which featured heavily in the proper usage of Serpent in this thesis, so this is not an independent comparison of codes

[2]Produced as part of this thesis

[3]Compared from [14]

Figure 3.13 shows the $k_{infinity}$ for the three Serpent variants tested. Here the Serpent 1.1.17 and Serpent 2 code versions used in this thesis provide nearly identical results to one another. This suggests that the Serpent version has a small role to play in the final results.

Notably, the Serpent results from Dr. Marleau follow largely the same trend, but with a higher mk. There are a couple of reason for this differential. Firstly, in the Benchmark used by McMaster it was largely selected to have a fuel cladding around the central Zirconia pin, while Dr. Marleau's group removed this cladding around the pin. The benchmark was ambiguous about this point. This may have been a source of the noted differences, however a test of the benchmark results with and without the cladding around the central pin reveals that this has a fairly small role, and is not a significant cause of the discrepancy. As mentioned previously, Dr. Marleau's lattice cell was acquired for analysis in this thesis. When analyzing this file some discrepancies in the library were discovered.

The library code used in Dr. Marleau's cell is `"endfb7/sss_endfb7.data"`, while the library used in this thesis is `"endfb7/sss_endfb7u.xsdata"`. This suggests that the library version is the source of this issue, as long as the cell used here is the final cell used in Dr. Marleau's report. Sensitivity to the library is a useful topic of further research.

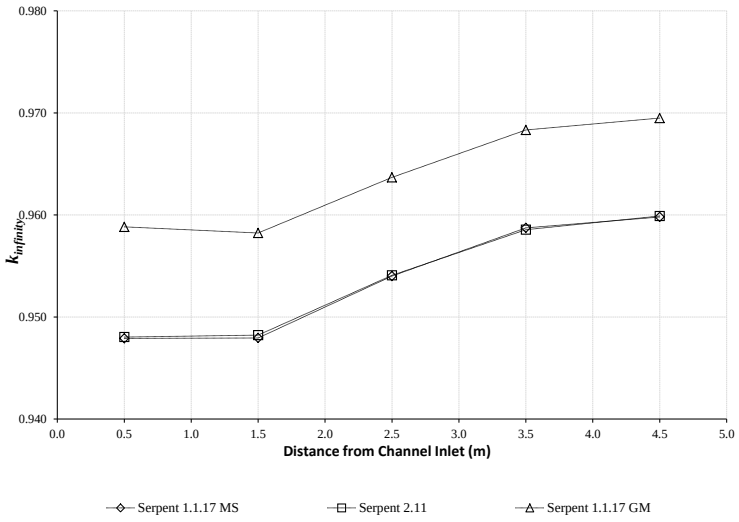

Figure 3.14: Serpent Benchmark k_{inf} results for exit burnup fuel

Figure 3.14 continues the trend where the Serpent difference appear to be due a difference in usage.

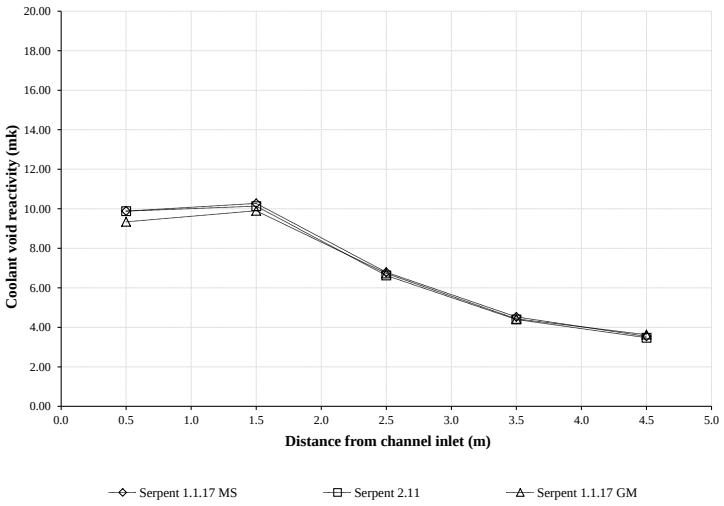

Figure 3.15: Serpent Benchmark CVR results for fresh fuel

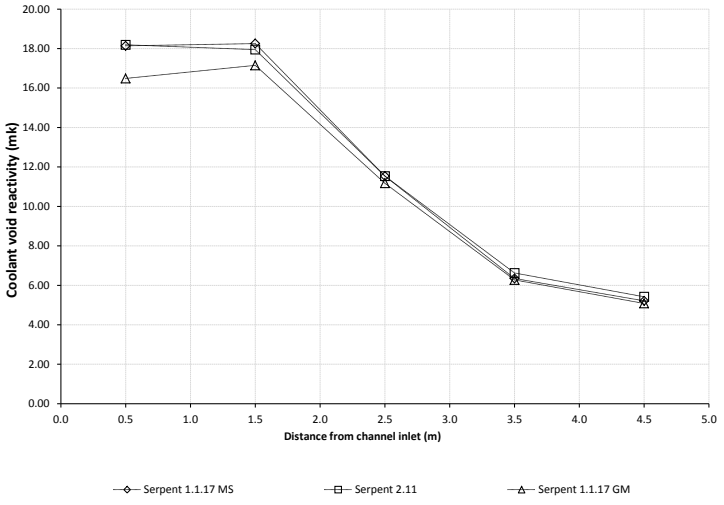

Figure 3.16: Serpent Benchmark CVR results for exit burnup fuel

Figures 3.15 and 3.16 provide nearly the same information as figures 3.13 and 3.14, showing how the trend between the different inputs is not dependent on the specific version of Serpent.

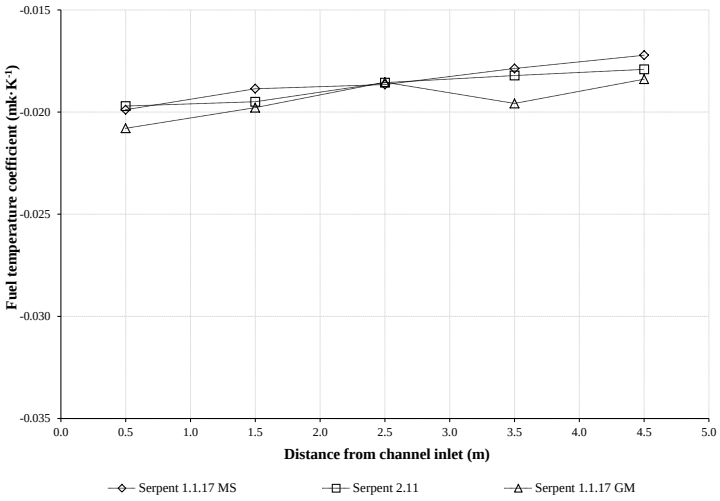

Figure 3.17: Serpent Benchmark FTC results for fresh fuel

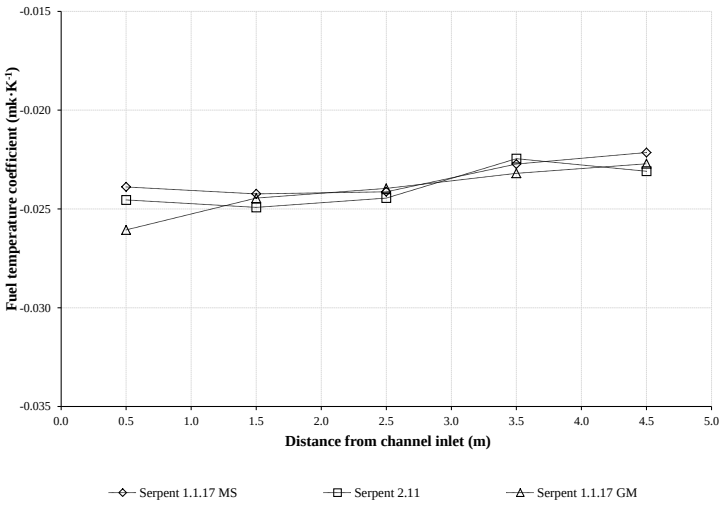

Figure 3.18: Serpent Benchmark FTC results for exit burnup fuel

Figures 3.17 and 3.18 again show that the differences between Serpent 1.1.17 and Serpent 2 are insignificant. The Linear Element Rating plots (figures 3.19-3.24) emphasize this point where the similarities between l'École Polytechnique and this work are observable, as well as the similarity to other physics code predictions earlier in this chapter.

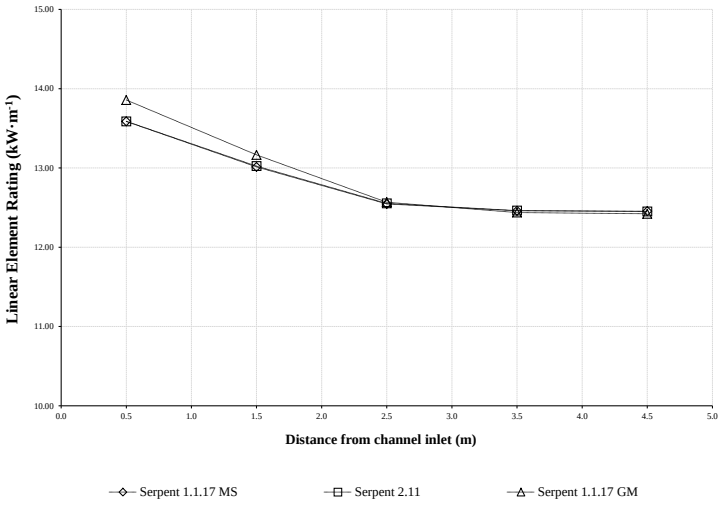

Figure 3.19: Serpent Benchmark LER results for the inner ring of elements of fresh fuel

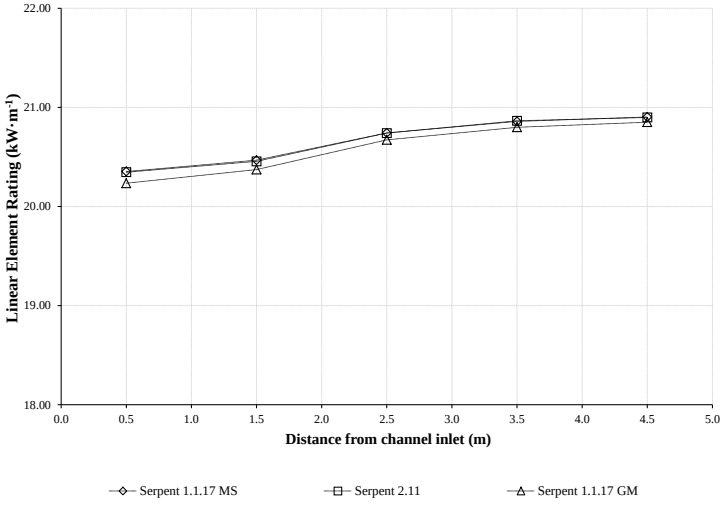

Figure 3.20: Serpent Benchmark LER results for the middle ring of elements of fresh fuel

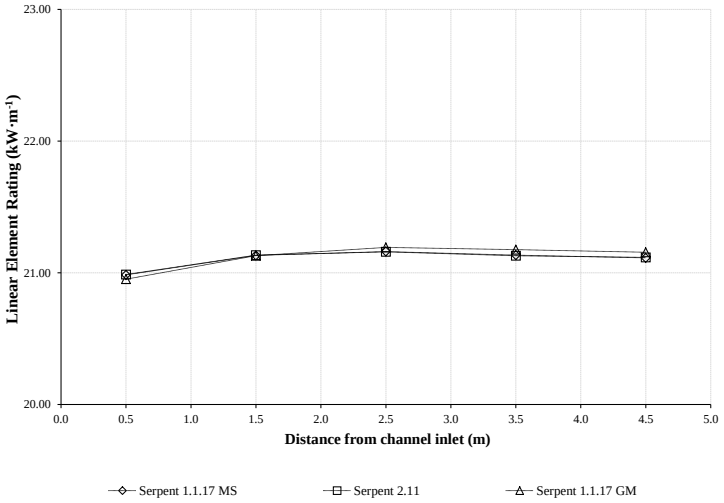

Figure 3.21: Serpent Benchmark LER results for the outer ring of elements of fresh fuel

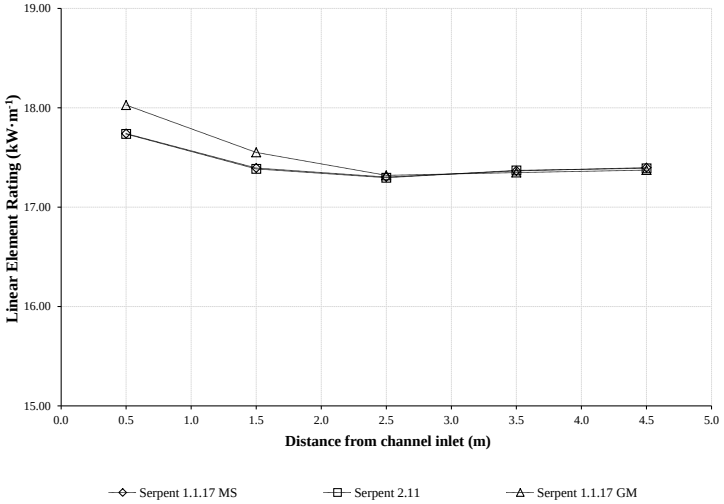

Figure 3.22: Serpent Benchmark LER results for the inner ring of elements of exit burnup fuel

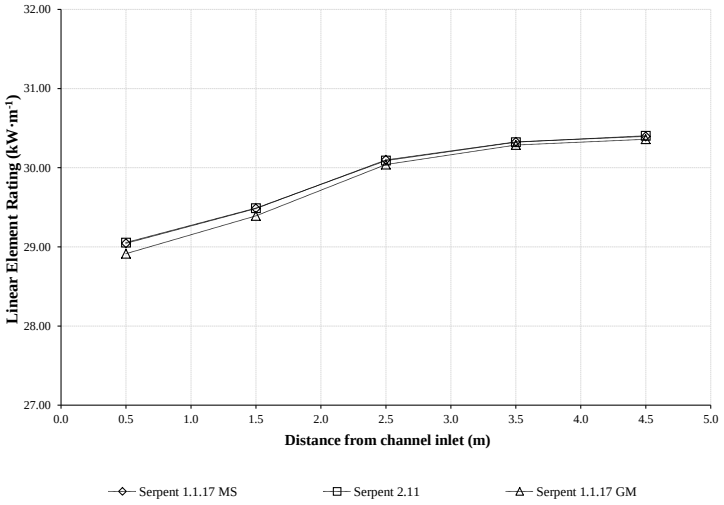

Figure 3.23: Serpent Benchmark LER results for the middle ring of elements of exit burnup fuel

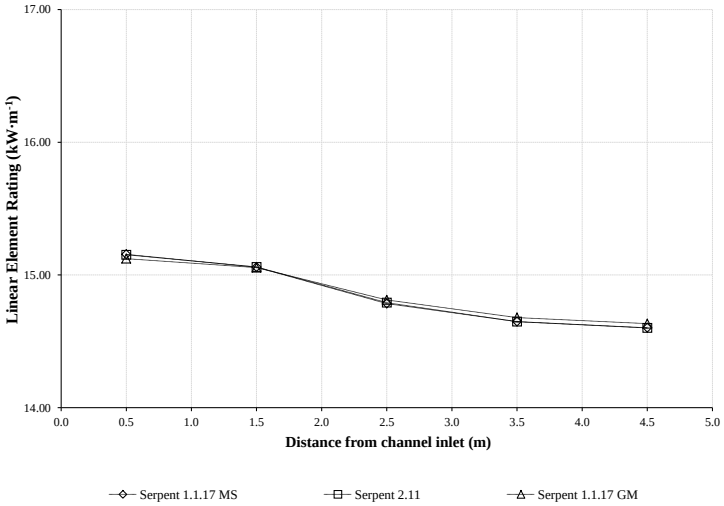

Figure 3.24: Serpent Benchmark LER results for the outer ring of elements of exit burnup fuel

Chapter 4

Insulator Region Analysis

The scope of this chapter is to derive the lateral coolant density function in the insulator region of the pre-conceptual SCWR and then measure its effect on the neutronics of the lattice cell. Given the acceptable benchmark results from the previous chapter, SERPENT was then used to study the effects of lateral coolant density variations on key reactor physics parameters. This chapter estimates the lateral density gradient at five axial locations with a number of varying assumptions. The method of calculating the thermal properties in the insulator region is addressed.

4.1 Methodology

4.1.1 Modelling the SCWR Cell in WIMS-AECL

The PT-SWR Cell is modelled using WIMS-AECL version 3.1.2.1. Nuclear data is taken from the E70ACR library included with the release of WIMS-AECL, based on data from the ENDF/B-VII nuclear data library [24]. The design of the lattice cell is based upon the pre-conceptual SCWR design in he AECL document 217-123700-REPT-001 [9]

For this model, the density of the water in the porous insulator region is normally assumed to be the same density as the average bulk coolant density at each axial location. The reference model addresses the change in temperature in the insulator region, but does not modify the density of the water within the insulator which would occur due to the temperature change. Essentially, the model assumes that the coolant water that flows into the insulator region remains at the same temperature and density as the central coolant. Since there is a temperature gradient in the insulator there must be strong property variations laterally. Depending on the axial position this has a very strong effect on the density of the light water in this region. For example, the density of water is 69.7 $\frac{kg}{m^3}$ at 478 K to 876.0 $\frac{kg}{m^3}$ at 881 K [9][44]. To account for axial effects, this model must be evaluated at several sections along the length of the channel. In particular the changes in coolant properties in the pseudocritical transition must be considered.

Table 4.1: Temperature Boundary Conditions

Boundary Condition	Coolant/Liner Tube	Pressure Tube Inner Surface
Channel Position 0.5m	632.35 (K)	477.55 (K)
Channel Position 1.5m	656.30 (K)	485.51 (K)
Channel Position 2.5m	675.27 (K)	491.82 (K)
Channel Position 3.5m	774.05 (K)	524.65 (K)
Channel Position 4.5m	881.45 (K)	560.35 (K)

Due to the large changes in the coolant properties and material temperatures throughout the channel, the two-dimensional lattice cell is evaluated at five equally spaced axial locations. This is done in order to study the effects of neutron transport and the changes in physics behaviour for the entire core. These five positions are considered to be sufficiently descriptive of the average neutronics of the HEC [7]. Table 4.1 and figures 4.1 and 1.4 summarize the coolant conditions used at each of the five axial locations [9]. These are used as the inner boundary conditions for the inner wall of the insulator region.

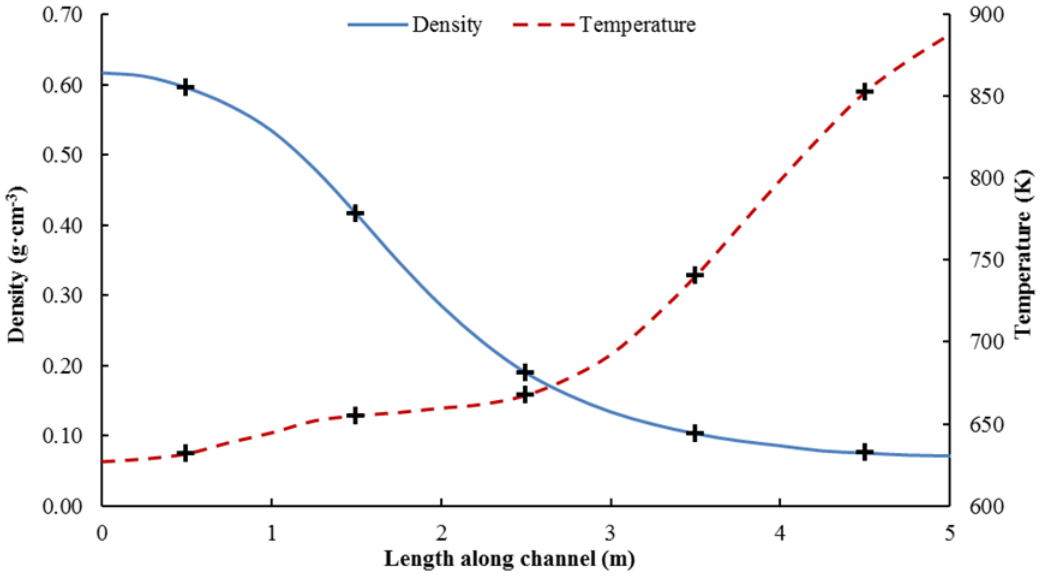

Figure 4.1: Coolant properties along length of PT-SCWR Channel

4.1.2 Methods for Modelling the Insulator Region

In order to calculate thermal profile within the insulator region at each of the five axial locations, a number of assumptions of the properties of the insulator are needed. First, the temperature gradient within the insulator must be determined accurately so that the proper density distribution can be assigned. A key element in predicting

the insulator temperature gradients is the assumptions applied for the effective thermal conductivity within the insulator. This work assumes that the coolant inside the porous insulator region does not transfer heat significantly through convection, only through conduction due to the expected insignificant flow rate inside the porous insulator.

4.1.2.1 Governing Heat Equation

The lateral coolant density is calculated by modelling the conductive heat transfer though the insulator by applying Fourier's Law. The insulator region is treated as a two-dimensional cylinder with boundary conditions matching the inner coolant temperature and outer moderator temperature of the reference model. While the insulator region is a three-dimensional cylindrical object, the heat conduction along the axial direction is assumed to be negligible compared to the radial temperature gradient. It is assumed that there is no temporal or angular dependence. In this way, the problem is reduced to a single dimension, r. In a steady state the heat transferred from the liner tube to the insulator region must equal the heat transferred from the insulator region to the pressure tube.

$$Q(r) = Q(r + dr) \tag{4.1}$$

Therefore:

$$\frac{\partial Q}{\partial r} = 0 \tag{4.2}$$

The heat flow through a radial region is given by Fourier's Law as:

$$Q = -k2\pi r \frac{\partial T}{\partial r} \tag{4.3}$$

Substituting equation 4.3 into equation 4.2 results in:

$$\frac{\partial}{\partial r}[-k2\pi r \frac{\partial T}{\partial r}] = 0 \tag{4.4}$$

Dividing the constants out, and noting the thermal conductivity is a function of temperature creates the governing equation for the problem at a given axial location.

$$\frac{\partial}{\partial r}(rK(T)\frac{\partial T}{\partial r}) = 0 \tag{4.5}$$

Equation 4.5 is a second-order non-linear ordinary differential equation. It has no exact solution; the numeric solution is obtained from the finite element solver FlexPDE 5.0.

The variables in this equation are the radial position, r, (running from the liner tube to the pressure tube), temperature, T, (the output variable, with defined boundary conditions) and the thermal conductivity, $K(T)$ of the insulating material. Thermal conductivity in water has a strong dependence on temperature, which is the source of the non-linearity of the equation.

If the thermal conductivity of the insulator and water is assumed to be constant, independent of the temperature of the light water and ceramic insulator, the equation simplifies to:

$$\frac{\partial}{\partial r}(r\frac{\partial T}{\partial r}) = 0 \tag{4.6}$$

Equation 4.6 is a second-order linear ordinary differential equation. This is a significantly less realistic equation, though it is simpler to compute.

Solving for temperature as a function of position results in Equation 4.7.

$$T(r) = A \times \ln(r) + B \tag{4.7}$$

Temperature as a function of radial position. The temperature distribution in this simplified two-dimensional cylindrical insulator region is a logarithmic curve, with A and B selected to match the boundary conditions. The boundary condition for each model, defined in equations 4.5 and 4.7 are the reference model defined temperatures for the coolant as the inner temperature and the pressure tube as the outer temperature.

The boundary conditions described in Table 4.2 are used for all the different treatment models. Table 4.3 on page 50 indicates the density of the water at the

Table 4.2: Temperature Boundary Conditions

Boundary Condition	Channel Position 0.5m	Channel Position 1.5m	Channel Position 2.5m	Channel Position 3.5m	Channel Position 4.5m
Coolant Liner Tube (K)	632.35	656.30	675.27	774.05	881.45
Pressure Tube (K)	477.55	485.51	491.82	524.65	560.25

given boundary conditions.

As seen in Figure 1.4 on page 8 the density of water has a strong nonlinear dependence on the temperature of the water for the pressure and temperature range explored. The simplified logarithmic temperature distribution is produced by ignoring the strong dependence of the thermal conductivity on temperature near the pseudo critical temperature. Using a constant thermal conductivity creates a model where the temperature of the insulator region follows a natural logarithmic trend. This simplified model is used in the analysis as the Log T model.

Solving Equation 4.5 in FlexPDE using the thermal conductivity of water generates a temperature distribution curve named the k(water) Model. The k(water) model does not account for the effects of the thermal conductivity of the insulator region itself. To account for the YSZ thermal conductivity within the insulator regions, knowledge of the thermal conductivity of the YSZ composite material is required, which is also a function of temperature.

The non-linear behaviour of the thermal-conductivity is included by determining the temperature distribution within the insulator region. Furthermore, the effective thermal conductivity, accounting for both water and Yttria-Stabilized Zirconia (YSZ), of the insulator should be used in solving Equation 4.5. The thermal conductivity of water is obtained from mini-REFPROP based on the NIST database Version 9.1 at 25 MPa [44]. The exact solution to equation 4.5 is determined using FlexPDE 5.0 [45]. These programs are lightly described in Appendix F on page 107. This analysis assumes that the water within the porous ceramic insulator is largely stationary and not mixing. The accuracy of this assumption depends on the properties of the porous YSZ in the insulator region, along with the SS310 Liner Tube. The accuracy of this assumption is not tested in this thesis, requiring significantly more advanced work in the field of thermal-hydraulics.

There is limited reference information for the particular porous mixture of YSZ and water used in the pre-conceptual design, so it is necessary to find an approximation of the thermal conductivity. The model of Woodside allows calculation of the effective thermal conductivity of a porous mixture of a solid and gas as a function of the effective porosity and the thermal conductivities and densities of the constituents

[46]. The work of Schlichting, Padture and Klemens presents the measured thermal conductivity of solid Yttria-stabilized Zirconia at 8 mol per cent and 3 mol per cent Y2O3 in ZrO2 [47]. The 10 weight per cent Y2O3 in ZrO2 used in the PT-SCWR design is equivalent to 5.72 mol per cent, and thus an interpolation is done between the values presented by Schlichting et al. This information, combined with the varying thermal conductivity of water are used as input for the model of Woodside and evaluated at 76% porosity. This results in an evaluation of the effective thermal conductivity of the porous mixture of YSZ and water as a function of temperature that can be used for calculation of the temperature distribution in the insulator region.

The resulting thermal conductivity curve, accounting for the presence of water and YSZ at varying temperatures, is shown in Figure 4.2. Notably, this curve is superficially very similar to the thermal conductivity of water alone, though at a significantly different scale. The addition of the YSZ thermal conductivity is nearly a constant multiplied against the thermal conductivity of water. An exact constant would be filtered out in Equation 4.5.

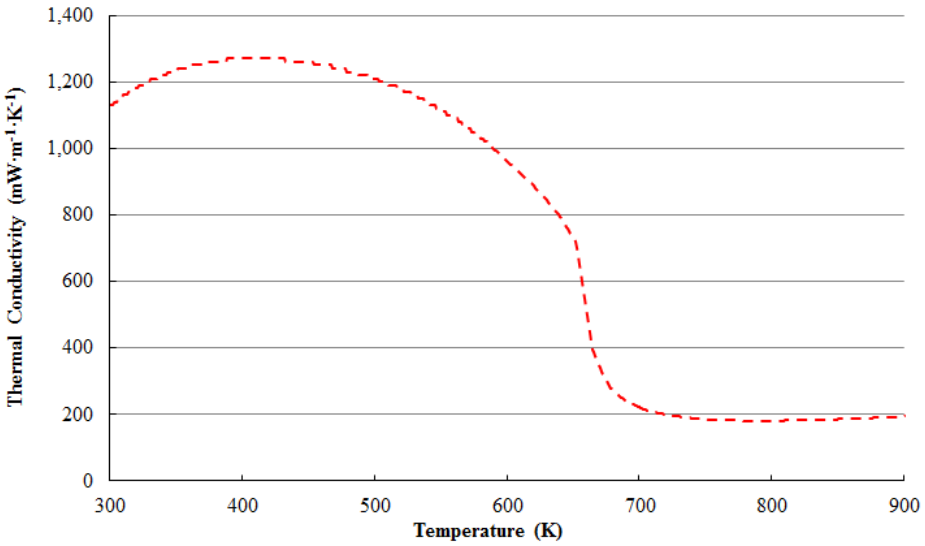

Figure 4.2: Calculated Thermal Conductivity of Porous Insulator Region

This thermal conductivity curve is used as an input to Equation 4.5, created a model that accounts for the thermal conductivity of Water, Yttria and Zirconia. This model is referred to as the k(WaZr)[1]or k(Water-YSZ) Model.

While the solution of temperature and density within the insulator is continuous, spatial discretization is necessary for input into the WIMS-AECL model. When subdividing the insulator region, the total mass of water in each subdivision must be

[1]WaZr: Water - Zirconia

conserved. Conservation of the total mass of water within the region is accomplished by integrating the density function across the cylindrical subregion of interest, divided by the subregion. This is shown briefly in Equation 4.8.

$$d_{\text{ave}} = \frac{M}{V} = \frac{\int_{z_1}^{z_2} \int_0^{2\pi} \int_{r_1}^{r_2} d(r) \partial\theta \partial z}{\pi \partial z (\Delta r)^2} \tag{4.8}$$

The density is determined previously to be only a function of radius r, as $d(r)$. The length dimension, z, is factored out and plays no role in this equation, as we are only looking at a constant z position. Θ is not a variable of the density, and is factored out as 2π. The density in a given subsection is therefore:

$$d_{\text{ave}} = \frac{\int_{r_1}^{r_2} d(r) r \partial r}{{r_2}^2 - {r_1}^2} \tag{4.9}$$

Equation 4.9 is solved in Excel, and was checked in MATLAB.

Table 4.3: H_2O Density Boundary Conditions

Boundary Condition	Channel Position 0.5m	Channel Position 1.5m	Channel Position 2.5m	Channel Position 3.5m	Channel Position 4.5m
Coolant/Liner Tube ($\frac{kg}{m^3}$)	592.5	382.4	160.9	89.5	69.6
Pressure Tube ($\frac{kg}{m^3}$)	876.5	867.6	860.3	818.9	765.5

In order to estimate the sensitivity of the methodology to the discretization scheme, three models of insulator are used: i) 3-subregions with constant density ii) 3 subregions and iii) a model with 10 subregions. This allows a determination of how many subdivisions are required for a good estimate of the distribution in the insulator region while also allowing a test of the results against constant water density assumptions.

Ultimately the different models used are referred to as Logarithmic T, k(Water) and k(Water-YSZ). Each model also has a variation in the number of subregions; with 1, 3, and 10 subregions used.

Figures 4.3-4.7 show the density distribution for the model accounting for the thermal conductivity of both the coolant and the insulator material, k(Water-YSZ), in each of the five axial positions.

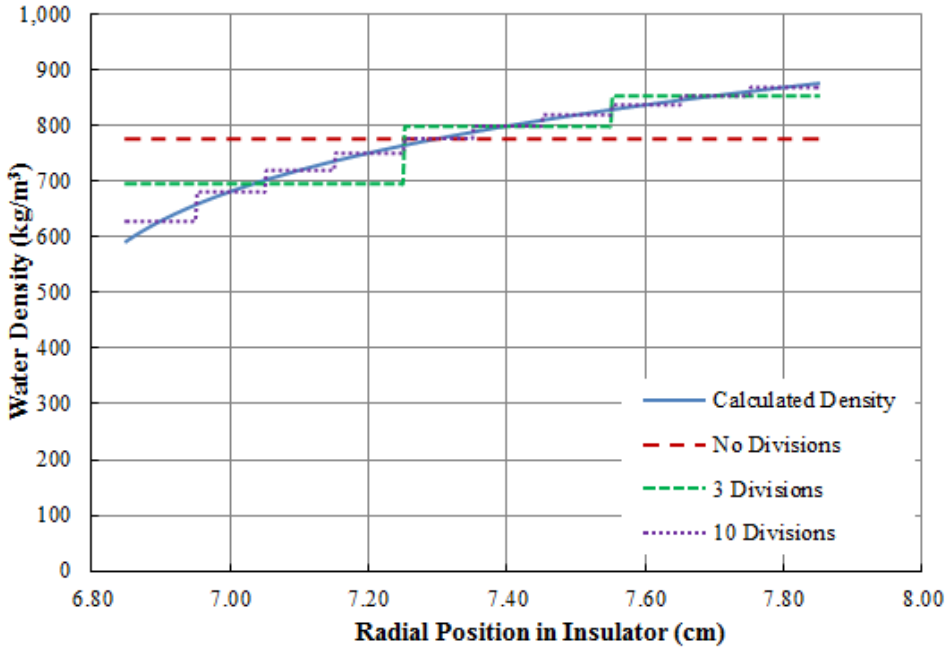

Figure 4.3: Calculated density curve with model k(Water-YSZ) at 0.5m from inlet

Figure 4.3 shows the density distribution. The solid blue line shows the calculated density gradient based on the calculations in FlexPDE. The dashed red line is the average density of the water[2]. The dashed green line is the calculated density curve divided into three subregions, with the dashed purple line the ten subregion densities.

[2]The density is weighted to account for the cylindrical co-ordinates of the system, which conserves the total mass of water in the system

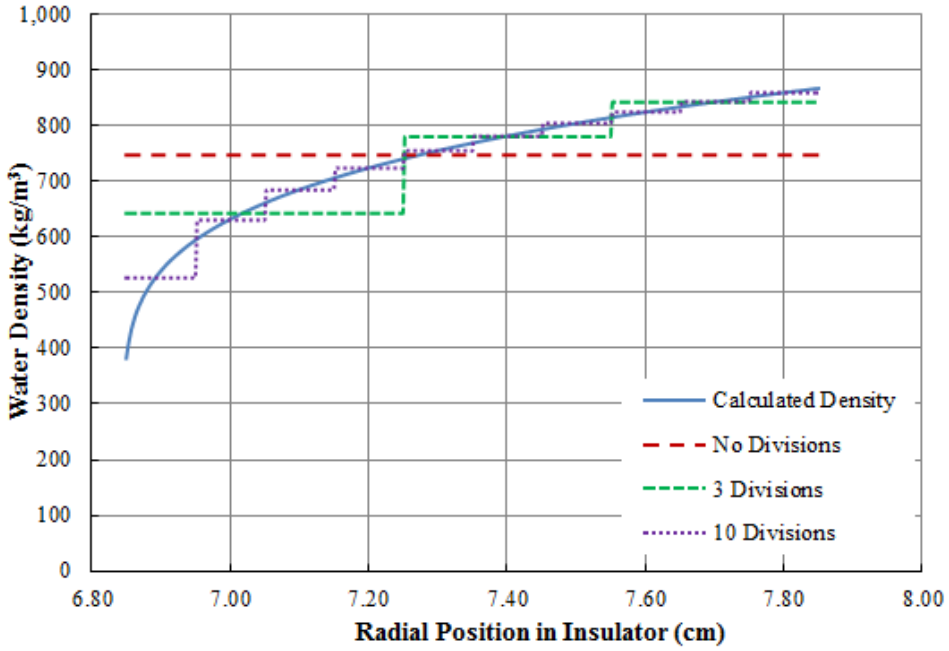

Figure 4.4: Calculated density curve with model k(Water-YSZ) at 1.5m from inlet

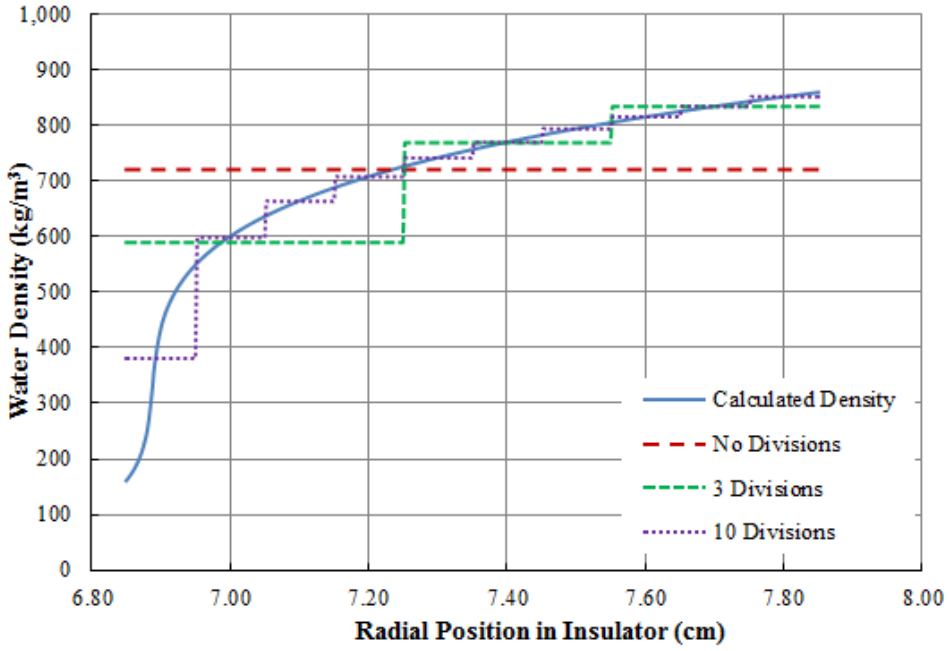

Figure 4.5: Calculated density curve with model k(Water-YSZ) at 2.5m from inlet

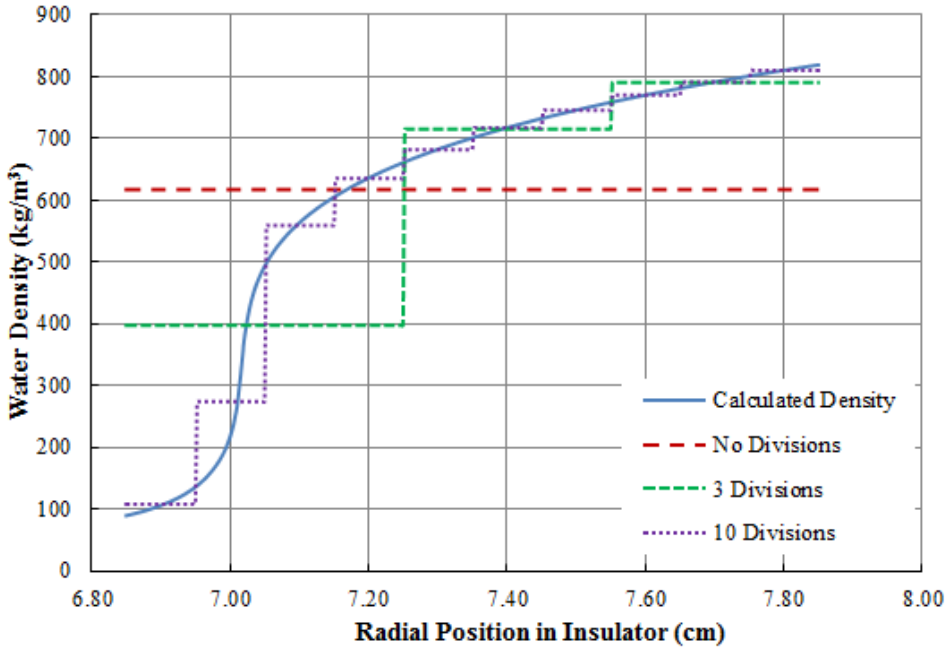

Figure 4.6: Calculated density curve with model k(Water-YSZ) at 3.5m from inlet

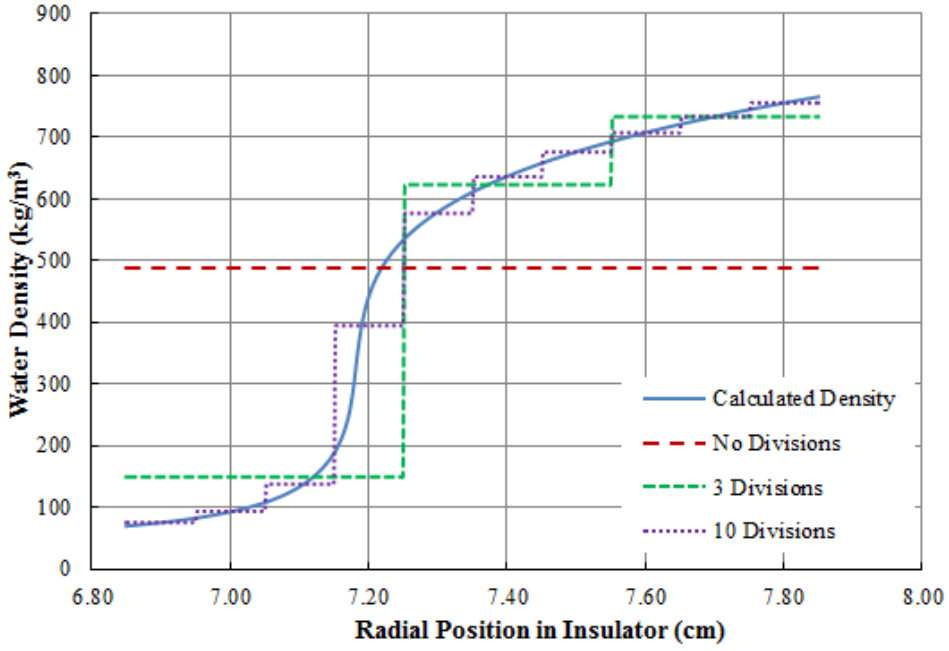

Figure 4.7: Calculated density curve with model k(Water-YSZ) at 4.5m from inlet

Figures 4.3-4.7 show the progression of the water density calculated in different

axial positions for a single model. The supercritical transition is visible as a significant density change. This is apparent both as the coolant transition between 1.5m and 2.5m, and in each subsequent insulator region.

Figures 4.7-4.9 are each located at axial position 4.5m with the three different treatments to the thermal conductivity. This reveals the effects of the different models. As the boundary conditions are defined, the water density at the inner insulator wall and outer insulator wall are unchanged between the models, only the curve between the endpoints is modified.

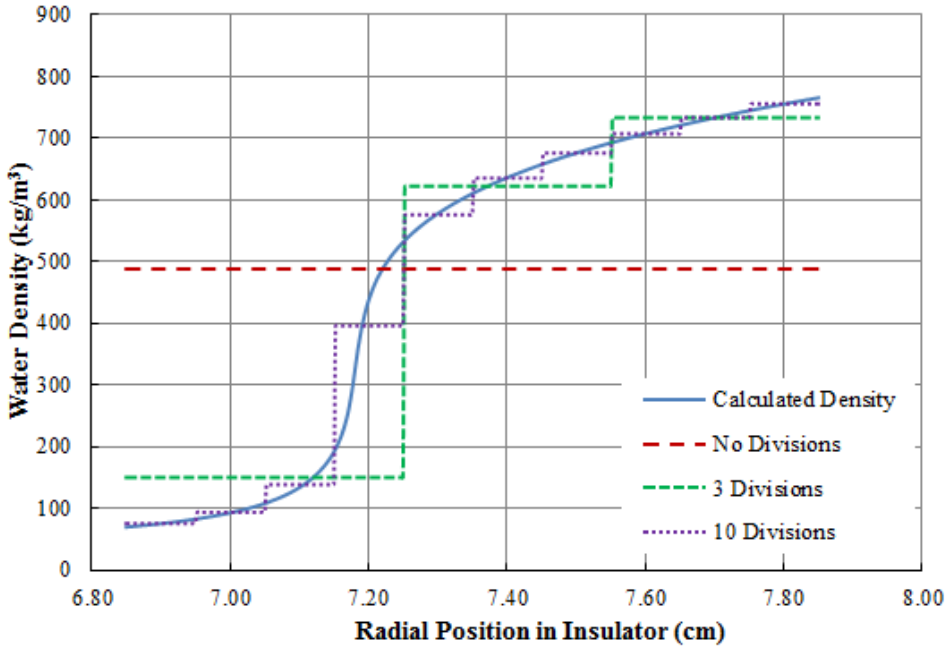

Figure 4.8: Calculated density curve with model k(Water) at 4.5m from inlet

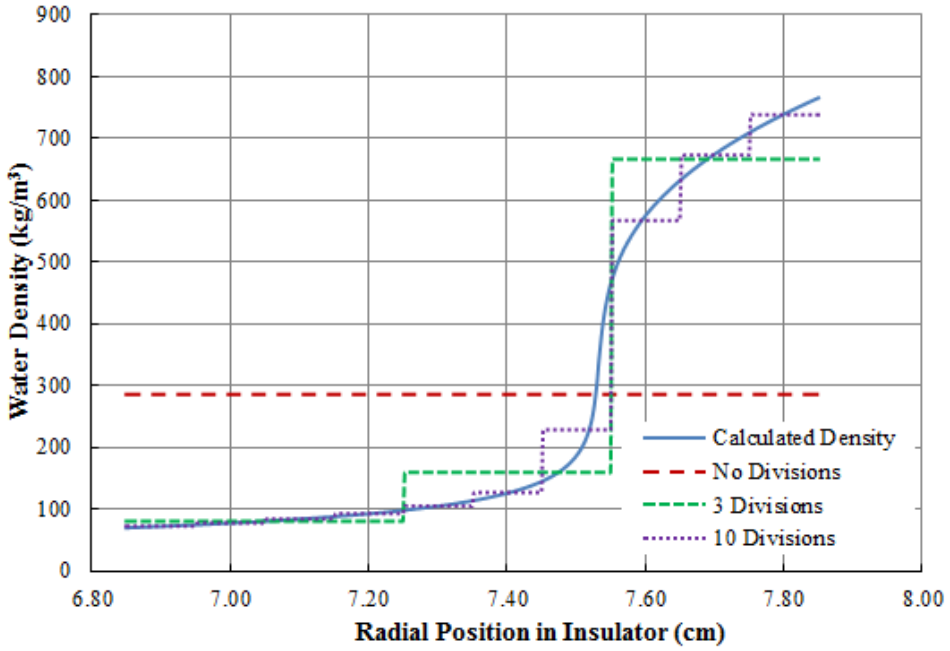

Figure 4.9: Calculated density curve with model k(constant) at 4.5m from inlet

The k(water) and k(Water-YSZ) models are nearly identical. Including the thermal conductivity information of the YSZ insulating material adds little value to the model while introducing additional sources of error. The Log T model consistently has a lower average density than the other two models for all axial positions. This density difference is strongest in the 3.5m and 4.5m models, where the supercritical transition is well-represented in the data. The Log T model estimates a significant different location for the supercritical transition than the more robust models. The remaining figures are located in Appendix C.

4.1.3 Modelling the SCWR Cell in SERPENT

Serpent is a stochastic Monte-Carlo code, unlike WIMS-AECL which is a deterministic code. A number of modifications between the two codes are made, but the library used is the ENDF-BVII library. A number of defined natural compositions in the WIMS-AECL library are not available in the Serpent libraries, so the natural compositions are recreated by using natural abundance values. The Serpent input files are calculated using 5000 generations and 5000 neutrons per generation, along with 300 additional unrecorded generations that are used to normalize at the beginning. An example Serpent input file is provided in Appendix E.

4.2 Results

4.2.1 SCWR-Cell in WIMS Results

At zero burnup the modified insulator treatment differs heavily from the reference model in all of the various models. Table 4.4 contains the average $k_{infinity}$ for the basic three subregion version of each model.

The voided case for the Coolant Void Reactivity (CVR) is calculated by fully voiding the coolant in the channel, liner tube and porous YSZ. Notably, this voided case is identical to the voided case for the reference model, as the only modification to the model is in the coolant density. The three different treatments all use the same voided results for the CVR calculation.

The density of the coolant is reduced to 0.001 $\frac{g}{cm^3}$, as used in the reference model [9]. Reducing the density to simply 0.000 $\frac{g}{cm^3}$ provides inconsistent results in both Serpent and WIMS-AECL. A pure vacuum cannot be used for void simulations.

Table 4.4: WIMS Average $k_{infinity}$ (ii- 3 subregions)

Model	$k_{infinity}$	CVR (mk)
Reference Model	1.26521	2.17
Logarithmic T (constant k)	1.27284	-1.84
k(Water)	1.27412	-2.55
k(Water-YSZ)	1.27412	-2.54
Void	1.26870	

All of the models explored increase the average $k_{infinity}$ of the reactor relative to the reference model. The data is an unweighted average from the five equally spaced slices of the channel. The consideration of the lateral coolant density variation, using the k(Water) model, indicates an average reactivity increase of 4.7 mk.

The most significant finding is that the role of insulator density modelling is related to the strong influence on CVR as seen in Figure 4.11. Notably, the increase in the overall average reactivity changes the estimated CVR from a positive to a negative value. A negative CVR is a major safety goal, reducing or entirely preventing a power spike during a Loss of Coolant Accident.[32] (LOCA)

Table 4.4 indicates a considerable value in considering the lateral density gradient of coolant in the insulator region. Even a token consideration of the effect in the Log T model bears more similarity to the more advanced models than the

reference case. The effect of including the thermal conductivity of the YSZ to the thermal conductivity of the insulator region calculation has a very small effect on the $k_{infinity}$ value as seen in Figure 4.10 compared to the value from adding the thermal conductivity of water.

The $k_{infinity}$ of each model has a strong dependence on the axial position. This is an expected result, as the coolant water is heated by the fuel, the temperature inside the insulator region increases, reducing the density of the water within the region. The lateral coolant density in the insulator region, even without consideration of the gradient is strongly dependent on axial position. As is visible in Figure 4.10, the change in coolant density in the explored models is strongly dependent on the axial position.

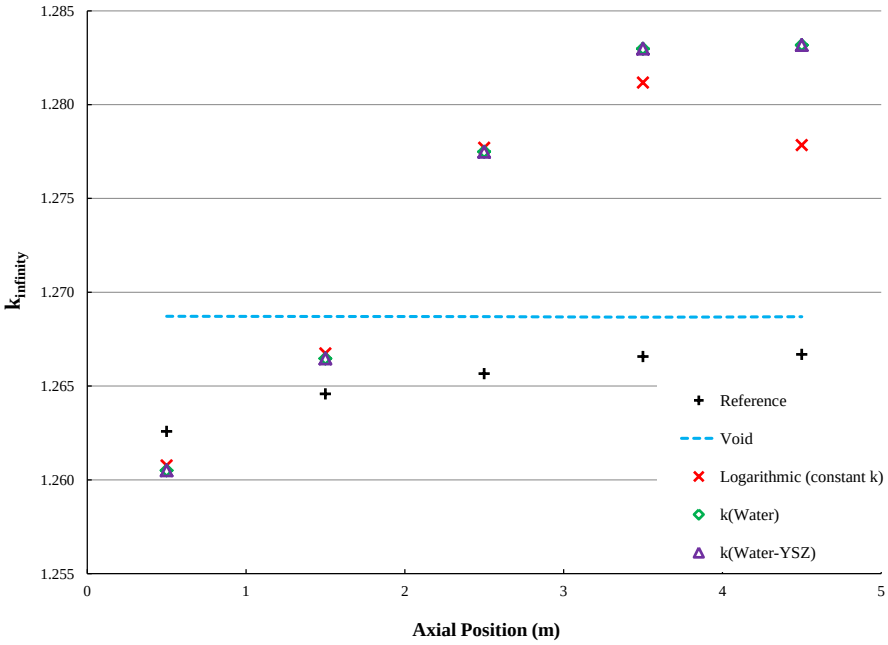

Figure 4.10: $k_{infinity}$ in WIMS, along the channel (3 subregions) (0.5-4.5 m)

The $k_{infinity}$ of the lattice cell generally increases with the distance from the coolant inlet. In the k(water) model, the $k_{infinity}$ is 14 mk higher at the outlet of the channel than at the inlet. This 14 mk change can have large effects on the characteristics and axial power profile of the reactor.

The Log T model differs significantly from the more robust models at the axial

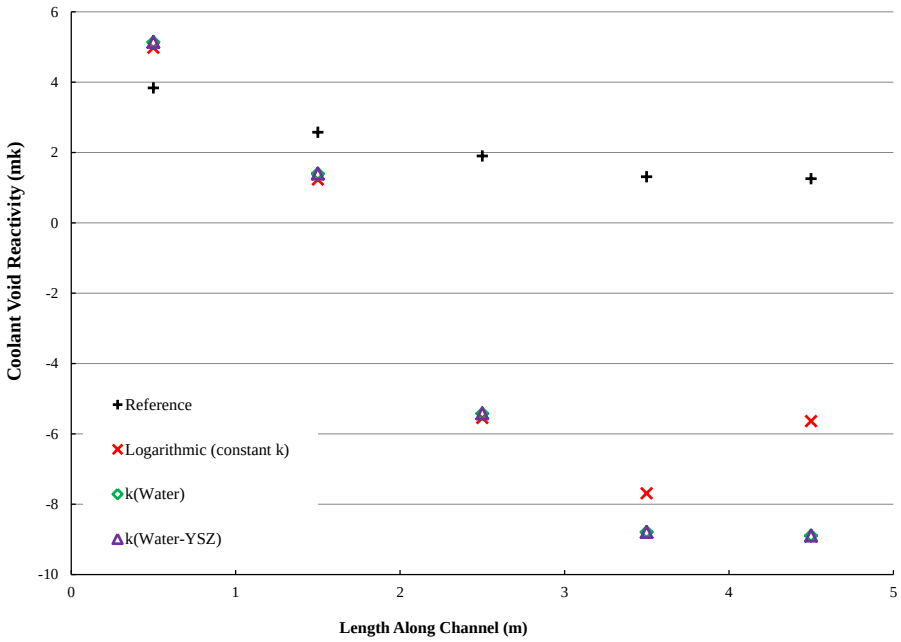

Figure 4.11: WIMS Coolant Void Reactivity (CVR) at zero burnup (3 subregions)

position nearest the outlet. The coolant distribution in figures 4.7-4.9 on page 53 reveal the lateral coolant difference between Log T and the other models is most significant towards the outlet, so the difference between the models here is an unsurprising result. The reduced reactivity of the system may be caused by the reduced water for moderation in the insulator region, which is a larger reduction for the Log T model as seen in figure 4.9.

The effect of changing the number of subregions within the insulator region was also studied. The effect of moving from one to three to ten regions has a differing magnitude depending on the axial position being studied, ranging from roughly 1.9 mk (in all 3 types of thermal conductivity assumed) to 0.26 mk. This effect is relatively small compared to other factors involved in the simulations. The channel average reactivity is affected by up to 1.28 mk. This is demonstrated in Table 4.5 for the Log T and the k(Water-YSZ) models.

The number of subregions used in the analysis provides a significant effect on the calculated $k_{infinity}$. Depending on the position in the channel, the $k_{infinity}$ can change up to 1.9 mk. Figure 4.12 demonstrates the dependence on axial position.

Table 4.5: WIMS Absolute difference in mk from reference model vs. number of subregions

	Logarithmic T Model			K(Water-YSZ) Model		
Channel Position	1 Region	3 Reg.	10 Reg.	1 Region	3 Reg.	10 Reg.
CP#1 0.5m	-0.40	-1.14	-2.31	-0.57	-1.31	-2.51
CP#2 1.5m	2.13	1.35	0.31	1.95	1.18	0.07
CP#3 2.5m	8.17	7.45	6.66	8.06	7.32	6.34
CP#4 3.5m	8.58	9.02	8.61	10.44	10.10	9.57
CP#5 4.5m	6.17	6.89	6.61	9.90	10.15	9.89
Average	4.93	4.71	3.98	5.96	5.49	4.67

It is notable that the number of subregions has a stronger effect closer to the inlet of the reactor than at the outlet of the SCWR. The methodology ensures that the total mass of water in the insulator region is conserved regardless of the number of subregions, only its position is more precisely defined. However, it's visually apparent that the 1 subregion and 10 subregion models have the greatest deviation in the position of the water near the outlet. Why these models agree nearest the outlet is unclear. There is a reduced total mass of water nearer the outlet of the reactor, but how this affects the discrepancy is unclear.

The k(water) and k(water-YSZ) models provide similar results to one another. This is predictable, given the near-identical shape of the thermal conductivity curves. The thermal-conductivity of water is dominating the overall thermal-conductivity of the highly porous YSZ insulator, resulting in only minor differences in the temperature distribution between the two models.

Table 4.6: WIMS Absolute difference in mk between K(water) and K(water-YSZ) vs. number of subregions

	K(Water) - K(YSZ)			
Channel Position	1 Region	3 Regions	10 Regions	Mag Average
CP#1 0.5m	-0.000628	0.000629	0	0.000419
CP#2 1.5m	0.004356	0.002494	0.021882	0.009577
CP#3 2.5m	0.003058	0.004289	0.005529	0.004292
CP#4 3.5m	-0.000607	-0.000608	-0.000608	0.000608
CP#5 4.5m	0	0.000607	0	0.000202
Average	0.001236	0.001482	0.005360	

In Table 4.6 the difference in mk between the highly similar models is explored. In most cases, the difference between the two models is less than 1 μk. The difference between the two models is most significant when the insulator is divided into 10 subregions. This is reasonable, as the differences between the two models will be clearer with more subdivisions. The difference is largest at Channel Position #2

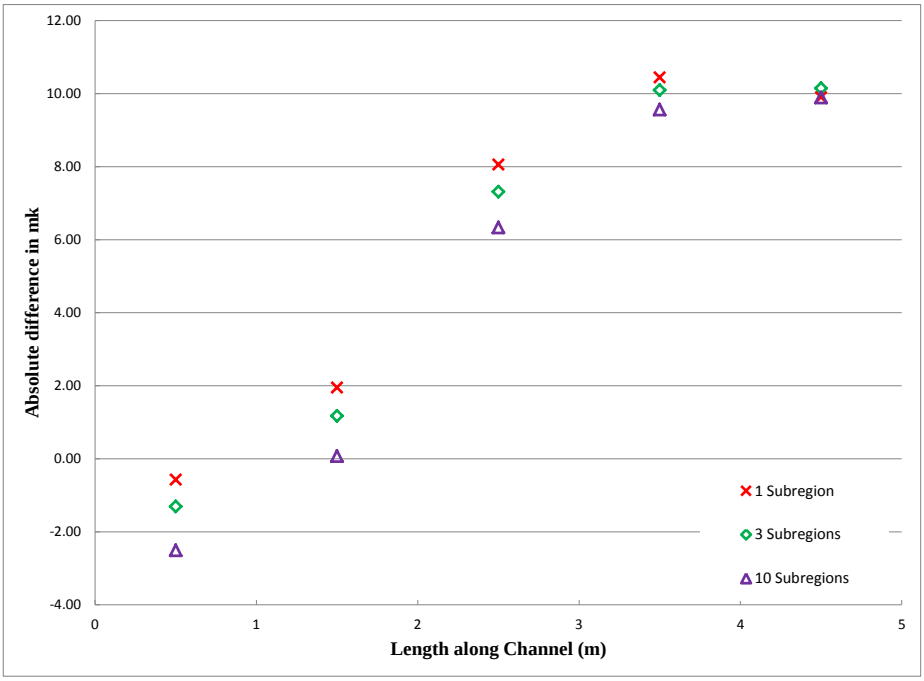

Figure 4.12: WIMS Absolute difference in mk from Reference Model and k(Water-YSZ)

(1.5m). Intuitively, one would expect the different in the models to be at its greatest with the largest temperature gradient, Channel Position #5 (4.5m), but this is not the case. A significant difference also occurs at Channel Position #3 (2.5m).

In order to explore this, Figure 4.13 shows the difference in the expected density of water between the two models. The peak difference in the coolant density in each model occurs at the period of supercritical transition. This is the expected period where each model would differ the most. The two models calculate a slightly different location for the supercritical transition, and this would be the most significant possible difference. Notably, at the Channel Positions at 2.5-4.5m, the curve has both a negative and positive component, reducing the overall difference in the density of water in the insulator region. At Channel Positions 0.5m and 1.5 m, the difference is wholly positive. This results in the density of water in the insulator region to have its greatest magnitude of difference in the middle regions of the reactor between the two models.

The two-sided density differential occurs when the pseudo-critical transition is

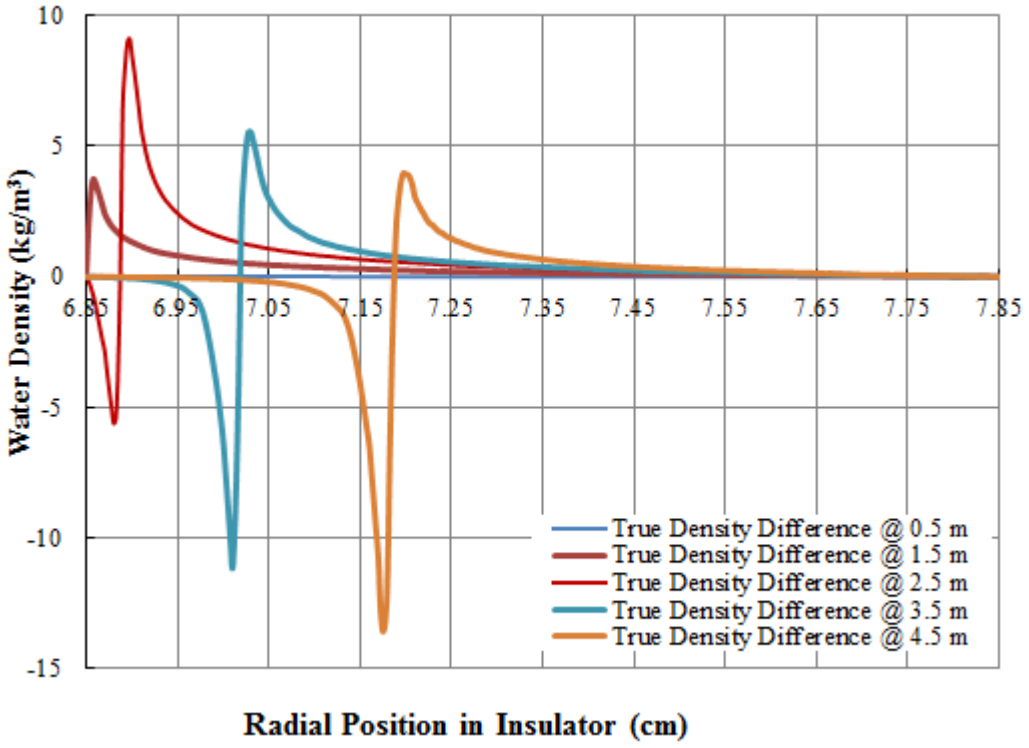

Figure 4.13: WIMS Difference in Calculated Water density in k(water-YSZ) - k(water) at 5 axial positions

located within the insulator region. The two models place the pseudo-critical transition in slightly different locations, resulting in a large difference in the density distribution at a given radial location. The one-sided density differential occurs when the pseudo-critical transition is outside the insulator region, so a slightly different curve of the two K(T) functions will estimate a different curve. There's no requirement for this curve to be both negative and positive.

In Figure 4.13, the curve for 0.5m, closest to the inlet, is nearly invisible as it tracks closely to 0 at all times. The total mass of water is at its largest difference at 2.5m.

Figure 4.14 is similar to Figure 4.13, but only looking at two axial positions and including the 10 subregion approximation. While the greatest difference in the $k_{infinity}$ is at CP 1.5 m, the mass difference between the two models is greatest at 2.5 m. The cause of this difference may be related to the wholly positive difference at 1.5 m.

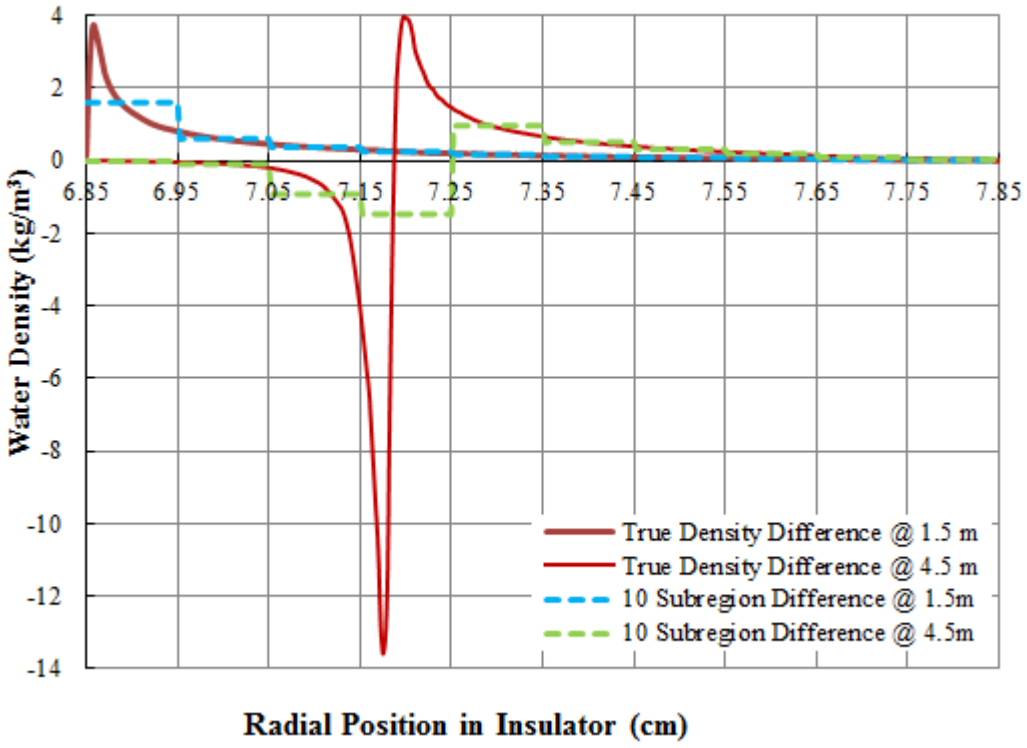

Figure 4.14: WIMS Difference in Calculated and Approximated Water density in k(water-YSZ) - k(water) at 2 axial positions

4.2.2 SCWR-Cell in Serpent Results

Serpent, as a Monte Carlo simulation, has a statistical uncertainty associated with its output values. The relative uncertainty in these results is approximately 0.009% for a given result. This statistical uncertainty increases to 0.013% when comparing between two different results[3]. With an average $k_{infinity}$ of around 1.25 or a reactivity of 200 mk, this statistical uncertainty is approximately ±0.072 mk. The uncertainty between two results is ±0.102 mk. This uncertainty can be reduced with longer simulations by increasing the number of individual runs and number of neutrons in each run. Serpent is calculated with 5000 neutrons per generation and 5000 generations.

Serpent 2.11 is already shown to be an excellent match for Serpent 1.1.17 in Chapter 3.2. Table 4.7 shows that this holds for the models explored here, so Serpent 2.11 is continued to be used for all the Serpent results in this section except in the demonstrative table 4.7.

[3]This assumes the uncertainty is a two tailed normal distribution, which is summed quadratically with itself

Table 4.7: Serpent 1 and Serpent 2 Average Positive Reactivity (ii- 3 subregions)

Model	Serpent 1 k_{inf}	CVR (mk)	Serpent 2 k_{inf}	CVR (mk)
Reference Model	1.25492	2.10	1.25492	2.21
Constant k(Log T)	1.25958	-0.85	1.25978	-0.86
k(Water)	1.26023	-1.26	1.26035	-1.22
k(Water-YSZ)	1.26027	-1.28	1.26020	-1.12
Voided Cell	1.25824		1.25842	

Table 4.7 shows the $k_{infinity}$ and the difference in ρ between the voided case and the models. With the ± 0.102 mk uncertainty, the sign of the CVR is well-defined. The difference between the k(water) and k(water-YSZ) models along with the Serpent 1 and 2 models. Serpent 1 and 2 generate similar results to one another, but have differences that are slightly larger than the uncertainty. The variance on the Serpent 2 results is slightly larger, but within the range of uncertainty. The k(water) model in Serpent 1 indicates that the consideration of the lateral coolant density over the reference model increases the reactivity of the PT-SCWR by 3.42 mk. This value is 3.48 mk for Serpent 2, a minor deviation given the statistical uncertainty.

There are clear differences in the results between Serpent 2 and WIMS-AECL. The voided case has an average positive reactivity of 205.4 mk in Serpent 2 and 211.8 mk in WIMS-AECL. This 6.4 mk separation is significant. Serpent and WIMS-AECL do not generate similar results. This is comparable to the difference in the cases in the Benchmark in Chapter 3 where the WIMS-AECL measurement has an average positive reactivity of approximately 13 mk and the Serpent 1.1.17 measurement from this thesis. The AECL reference model decreases in reactivity by 6.5 mk when simulated in Serpent. The models with the treated insulator region have an decrease of 7.4-7.8 mk when simulated in Serpent.

The calculated CVR of the models is somewhat less negative than in chapter 4.2.1, due to the trend where the reactivity of the treated models is lower in Serpent than in WIMS. Notably, the reference model continues to show a positive CVR, while the treated models show a slightly negative CVR in both WIMS and Serpent. The trends identified in the WIMS simulation continue to exist for the Serpent simulation, where the initial reactivity of the system is increased by appropriately creating a more realistic density gradient in the insulator region.

The reference model follows the same axial trend between Serpent and WIMS, where the reactivity of the system increases with increased axial position near the inlet of the reactor. The trend-line is the same, but he specific values of the reactivity between WIMS and Serpent differs by a significant degree. This may partially be the impetus for the AECL benchmark [8], given the differences between various models

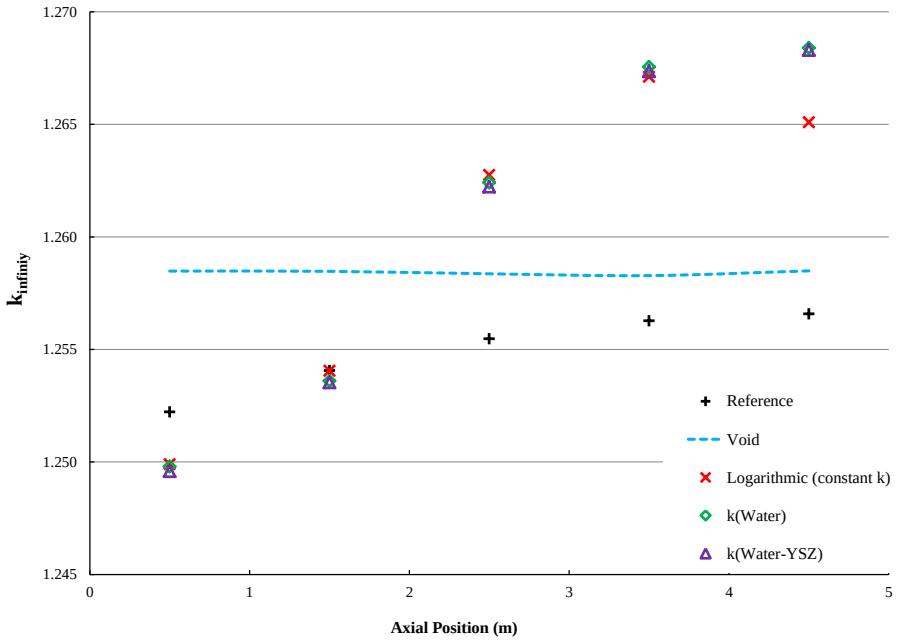

Figure 4.15: $k_{infinity}$ in Serpent 2, along the channel (3 subregions) (0.5-4.5 m)

for the same reference model.

Table 4.8 shows the difference between the Logarithmic T model and the k(water-YSZ) models against the AECL reference model results. It is the Serpent counterpart to Table 4.5 on page 59. This table shows that the number of subregions the insular region is divided into has a significant effect on the reactivity of he call, of up to 0.8 mk in an axial position. The variance is at is largest effect near the outlet of the reactor, when the density in the insulator region has the greatest differential. This is a reasonably expected result. It is also shown that the Log T model generates results more than 2 mk different from the more complex model, suggesting that the constant K model is a gross oversimplification.

Table 4.8 also reveals the value of the estimation of the location of the light water coolant. The 1 subregion model has no variation in the density of the coolant throughout the insulator region, just a more accurate total mass of the coolant. It has conserved the mass of coolant from the 10 subregion model, but estimates the physical location of that mass differently. In this case, the 10 subregion model locates the mass of water further from the fuel region and towards the moderator

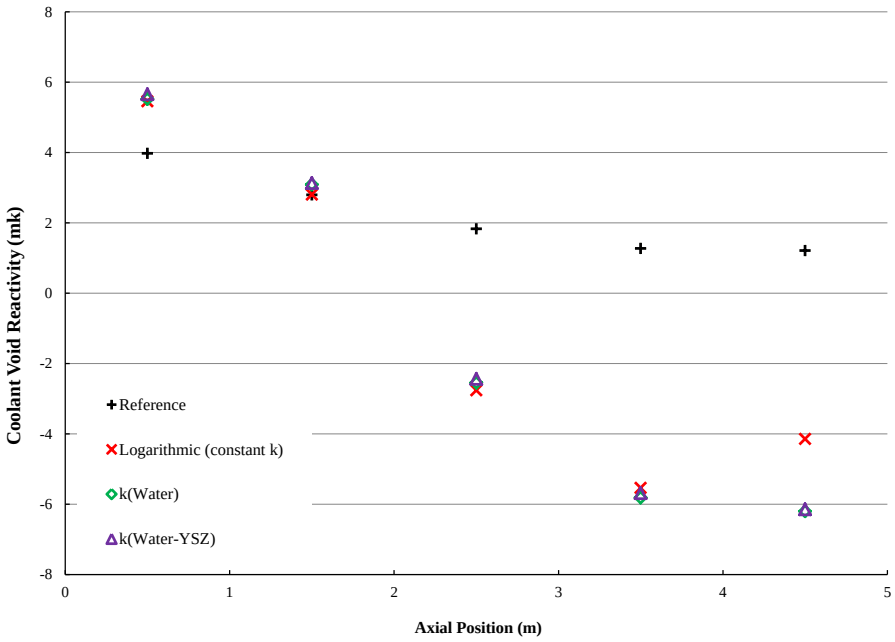

Figure 4.16: Serpent 2 Coolant Density Reactivity (CVR) at zero burnup (3 subregions)

region. Notably, table 4.8 indicates an increase in reactivity as more subregions are used, while table 4.5 for WIMS-AECL indicates a decrease. This is an interesting result, but no explanation has been uncovered.

Table 4.9 is the difference in reactivity between the k(water) and k(water-YSZ) models in Serpent 2. Noting that the uncertainty when comparing between two results is approximately ± 0.102 mk, we can see that 9 of the 15 results[4], or 60%, are outside of these bounds. In a normally distributed system, 34% of the results are outside of the first standard deviation. Therefore, it appears that there is a statistically significant difference between the k(water) and k(water-YSZ) models. The additional error is weak compared to the statistical uncertainty of 0.102 mk. The trend of the average difference between the two more complex models in Table 4.9 is different from the trend identified in Table 4.6 on page 59.

In order to ensure these results can be safely compared against one another, some other way to compare codes was required. The benchmark introduced in Chapter

[4] 8 out of 15 results for Serpent 1

Table 4.8: Serpent 2 Absolute difference in ρ (mk) from reference model vs. number of subregions

	Logarithmic T Model			K(Water-YSZ) Model		
Channel Position	1 Region	3 Reg.	10 Reg.	1 Region	3 Reg.	10 Reg.
CP#1 0.5m	-1.65	-1.48	-1.60	-1.83	-1.68	-1.53
CP#2 1.5m	-0.33	-0.01	-0.08	-0.30	-0.34	-0.34
CP#3 2.5m	4.20	4.59	4.72	3.92	4.27	4.44
CP#4 3.5m	5.85	6.81	6.78	6.54	6.96	7.21
CP#5 4.5m	4.51	5.35	5.45	6.82	7.35	7.63
Average	2.52	3.05	3.05	3.03	3.31	3.48

Table 4.9: Serpent 2 Absolute difference in ρ (mk) between K(water) and K(water-YSZ) vs. number of subregions

	K(Water) - K(YSZ)			
Channel Position	1 Region	3 Regions	10 Regions	Average
CP#1 0.5m	-0.192	-0.134	0.070	-0.085
CP#2 1.5m	0.127	-0.045	-0.204	-0.040
CP#3 2.5m	-0.151	-0.113	0.056	-0.069
CP#4 3.5m	0.143	-0.124	0.124	0.048
CP#5 4.5m	0.081	-0.056	0.087	0.037
Average	0.002	-0.094	0.027	-0.022

3, compared Serpent against other codes in a defined benchmark scenario, and then compared against another Serpent simulation generated by l'École Polytechnique de Montréal. The results presented suggest that Serpent is a valid code for this analysis, though Serpent and WIMS-AECL disagree significantly.

Chapter 5

Subchannel Coolant Variations with Serpent 2

In Chapter 4 of this thesis, the variation in coolant density in the insulator region of a PT-SCWR is explored. This chapter explores the coolant density variations in the subchannels of the coolant region in the PT-SCWR. The coolant density is simulated using the CFD code FLUENT.

Serpent 1.1.17 lacks the capability to import an arbitrarily fine density variation.[1] The beta version of Serpent 2 includes a multi-physics interface which permits an arbitrarily defined density matrix to be used as an input. In this case, this input is used to define a square matrix of points which define the coolant density in the coolant region.

5.1 Methodology

The Computational Fluid Dynamics (CFD) analysis was performed by Dr. Rashkovan of the Negev Nuclear Research Centre Negev (NRCN). Details of the CFD analysis that was performed with Fluent are given in Chapter 1.5. MATLAB scripts were used to convert the FLUENT results to input files for the multi-physics interface in Serpent 2. The scripts are included and described in Appendix A.

The model used for this analysis in FLUENT and Serpent 2 is the PT-SCWR model used for the benchmark in Chapter 3, with a solid liner tube and no coolant in the porous insulator. Using the same model is important for validity, though minor differences are unlikely to cause significant issues.

The Serpent calculations are performed with 20000 generations with 20000 neu-

[1] An input file for Serpent 1.1.17 complete this task. A material would be defined for each position in the coolant. A series of flat surfaces would need to be defined to define the boundaries of each coolant cell. The surfaces and materials would need to be checked for collisions with the fuel and cladding.

Table 5.1: Comparison of Bulk Coolant Density between Benchmark and FLUENT calculation

Channel Position	Reference Density $\frac{kg}{m^3}$	Fluent Density $\frac{kg}{m^3}$
CP#1 0.5m	592.54	549.10
CP#2 1.5m	382.46	291.64
CP#3 2.5m	160.92	168.15
CP#4 3.5m	89.49	120.52
CP#5 4.5m	69.63	99.48

trons per generation each, in order to minimize the Monte Carlo-associated uncertainty, to discern the existence of the potentially small signal. 300 unrecorded generations are run at the start, in order to allow the results to being to tend to a stable value before being recorded.

The CFD analysis provided results throughout the length of the lattice cell, but neutronics results were only obtained at the same five axial locations used previously in this thesis (0.5-4.5 m). The total number of square cells generated are as follows:

1×1 grid (a 15cm × 15cm cell size)
2×2 grid; cell size 7.5cm × 7.5cm
5×5 grid; cell size 3cm × 3cm
10×10 grid; cell size 15mm × 15mm
100×100 grid; cell size 1.5mm × 1.5mm
1000×1000 grid; cell size 0.15mm × 0.15mm

The 1×1 grid is equivalent to no subchannel analysis at all being performed in the reactor physics calculation, with a single bulk fluid density and temperature. This calculation does take into consideration the subchannel calculations performed in the Fluent analysis, so it does not generate the same coolant density as the Benchmark model or the AECL Reference model.

Table 5.1 compares the bulk coolant density used in the AECL benchmark and that calculated through the fine subchannel analysis in FLUENT. The subchannel analysis finds a softer trend or the desnity, where the inlet density is lower and the outlet density is higher. As such, the results at a given axial position in Chapter 5 cannot be directly compared to the same axial position in Chapter 3.

Serpent 2 is capable of measuring the pin power profile of each of the pins, permitting a calculation of the Linear Element Rating (LER). The calculation of LER is performed identically to the calculation in Chapter 3, where a total power of the bundle is assumed to be 1512.56 $\frac{kW}{m}$.[13]

5.2 Serpent 2 Subchannel Results

The SCWR lattice cell in Serpent 2 is measured at five different axial locations with six different coolant density profiles, as described above. The coolant density profiles are only a function of cell size. The $k_{infinity}$ of each of the 30 lattice cell combinations are calculated, along with the power density distribution among the three fuel rings. This information for all 30 permutations is provided in Table 5.2.

Table 5.2 and Figure 5.1 shows the positive reactivity in mk of all 30 permutations calculated. The uncertainty in this range is approximately ±0.0002 mk, with 20000 neutrons per iteration and 20000 iterations used plus 300 initial iterations. The reactivity of the system increases by 3.3 mk with the maximum resolution over the minimum resolution.

Table 5.2: Reactivity in mk of Serpent 2 Subchannel Analysis

Channel Position	1×1	2×2	5×5	10×10	100×100	1000×1000
CP#1 0.5m	189.02	189.06	189.02	189.10	189.66	191.58
CP#2 1.5m	189.80	189.82	189.99	190.23	192.23	194.43
CP#3 2.5m	192.23	192.16	192.34	192.43	193.90	195.88
CP#4 3.5m	193.54	193.52	193.65	193.63	195.02	196.61
CP#5 4.5m	194.33	194.28	194.48	194.37	195.48	197.05
Average	191.78	191.77	191.89	191.95	193.26	195.11

Figure 5.1 shows that the infinite multiplication factor is only significantly affected by the size of the subchannel cells when a 100×100 grid is reached. Notably, no diminishing returns are reached with the cell sizes selected. There is a minimum of 0.9 mm of distance between each fuel cell between two rings, and about 1.2-1.7 mm between two fuels cells in the same ring. The 100×100 grid is a cell size of 1.5 mm, and the 1000×1000 grid is a cell size of 0.15 mm. The subchannel calculation only has a significant impact when the cell size reaches the size of the subchannels. There was not enough resolution or variety of resolutions to determine a real trendline beyond this region.

The 1000×1000 subdivision calculation has a reactivity increase of 2.56 mk at the 0.5m (inlet) location in the reactor over the 1×1 no subdivision calculation. At the outlet side of the reactor at 4.5m, the increase in reactivity is approximately 2.72 mk. The axial position does not significantly affect the importance of the subchannel analysis sizes, though it appears as though it may be more significant for the major transition regions in axial positions 1.5 m and 2.5 m.

The Linear Element Rating of each of the 30 permutations[2] are shown in figures

[2]Five axial positions; Six different cell densities

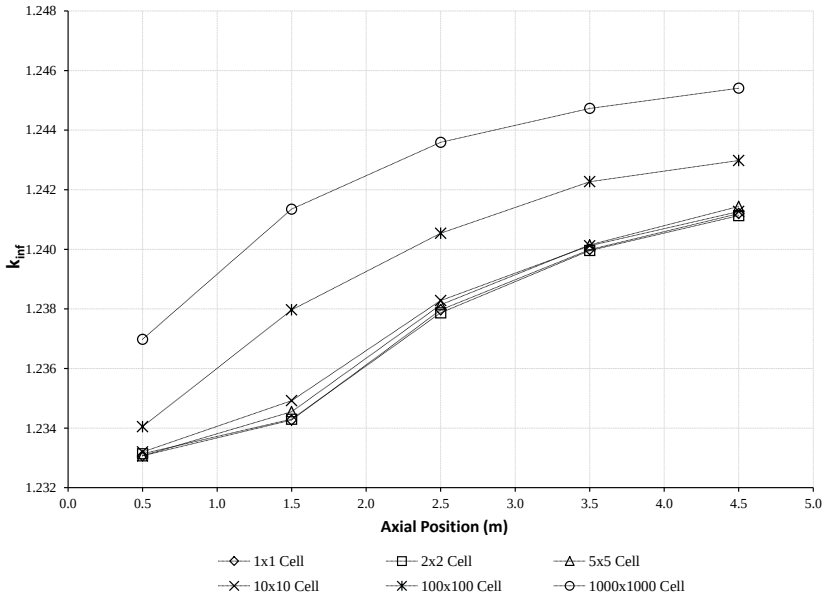

Figure 5.1: Serpent 2 Subchannel k_{inf} results

5.2 to 5.4.

Figure 5.2 shows a trend where all of the different subchannel sizes have an affect on the Linear Element Rating of the Inner Ring, unlike the effect on the reactivity of the system. Only the 1×1 and 2×2 cells overlap. Ignoring the Axial Position 0.5 m, there is a clear trend that the inner ring power level decreases towards the outlet of the reactor, and a non-monotonic trend regarding the cell size. Axial Position 0.5 m has little relation to the rest of the axial positions. This axial position has the lowest enthalpy, suggesting that this region, where the density of the water is the highest and least-affected by the reactor, the subdivision analysis has the least affect, but the fact the smallest cell size is a greatest outlier leaves room for interpretation. The smallest cell size is in the midpoint of LER of all 6 cell sizes.

Figure 5.3 for the middle ring shows a different trend compared to Figure 5.2. At Axial Position 0.5 m, the smallest cell division is a clear outlier even this close to the inlet of the reactor. This suggests that a subchannel analysis can calculate the proper balance of the power level between the inner and middle fuel rings near the inlet of the reactor. Outside of the first axial position, there is a clear monotonic trend where the smaller cell divisions increase the power level in the middle ring of the reactor. This is likely a result of the fact the middle ring is in the middle of the

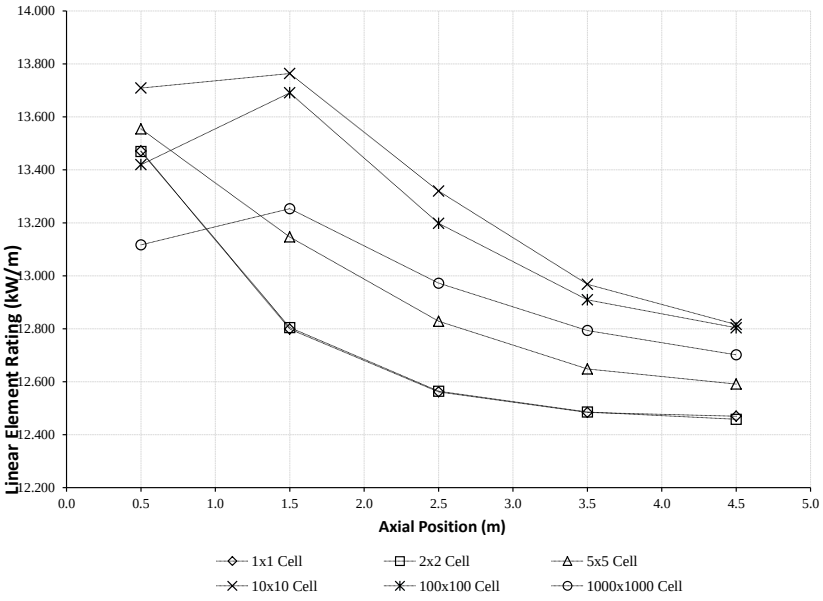

Figure 5.2: Serpent 2 Subchannel Inner Ring Pin Power

region that is affected by this analysis, drawing coolant density away to the liner tube and the central pin.

Figure 5.4 lacks a monotonic trend, a trait shared by Figure 5.2. Here, the smallest cell division is not a clear outlier at the first axial position. The smaller three cell subdivision all share a lower power level in he outer ring, but the smallest cell has the highest of the power levels. More and smaller cell sizes would need to be simulated to determine the true trendline.

At this point a number of patterns have emerged. At low cell sizes, the cells are nearly indistinguishable from each other. Only when the cell sizes approach the size of the actual subchannels does the analysis generate interesting results. The largest result discrepancies between cell sizes occurs at axial positions 1.5 m and 2.5m, when the coolant itself is near the psuedocritical transition zone.

The finest cell structure suggests a strong rebalancing of the power level towards the middle ring from the inner and middle rings as the subchannels are taken into consideration. This is a useful result, as the too-high LER rating was a significant factor in the design of the outer ring of fuel cells. These cells have a lower diameter in order to reduce the LER [9]. More very fine subchannels must be calculated,

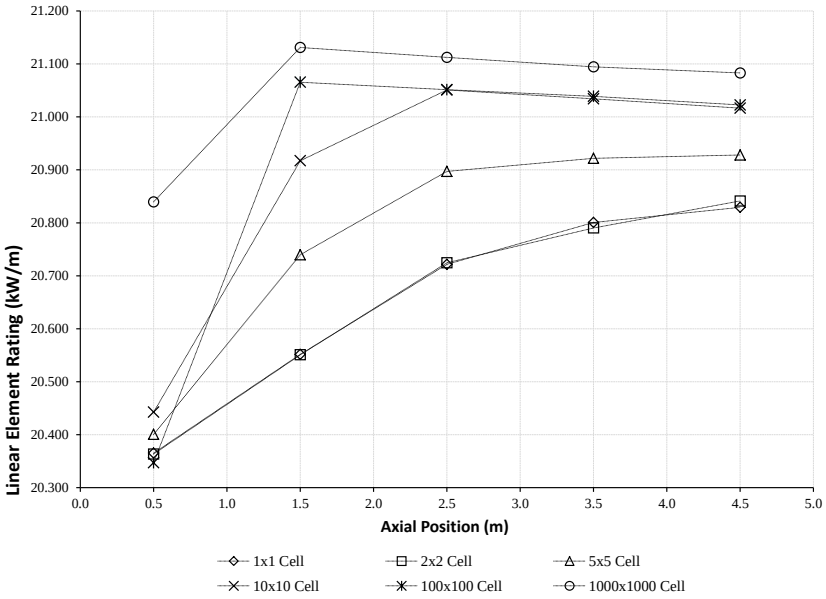

Figure 5.3: Serpent 2 Subchannel Middle Ring Pin Power

using more up-to-date thermalhydraulic analysis and finer cell sizes to determine the magnitude of this effect.

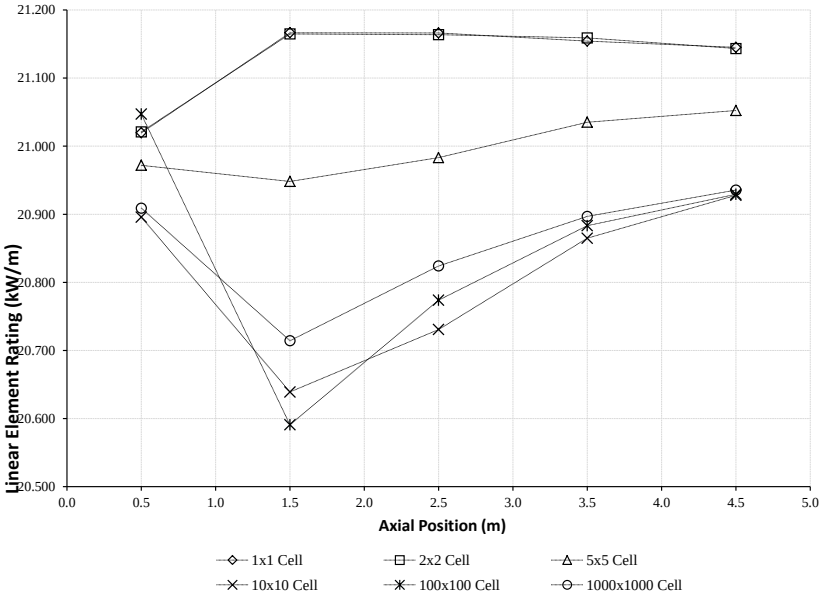

Figure 5.4: Serpent 2 Subchannel Outer Ring Pin Power

Chapter 6

Conclusions

The objectives of this work were two-fold. The first objective was to determine the effects of considering the lateral coolant density variations in the PT-SCWR cell. The second objective was to determine the strengths and weaknesses of the Serpent lattice physics code and determine if it is appropriate to use for the analysis of Canadian PT-SCWR designs.

This thesis used a simplistic methodology to determine the lateral coolant density in Chapter 4, where the density curve of the coolant in the porous insulator region is estimated simply through the thermal conductivity of water and the defined coolant and moderator temperatures. A CFD analysis of this region was not performed, due to a lack of specifications for the porosity, and the significant redesign of the PT-SCWR cell. Without a CFD analysis, quantitative conclusions that can be derived from this analysis are limited. However, it is clear that the coolant density variations in the insulator region of this particular geometry has the potential to generate powerful reactivity effects in the reactor.

The simulations of the coolant density variation in the insulator region are mostly about recalculating the total mass of light water engaged in moderation and absorption of the neutrons. This is apparent in figure 4.12 on page 60, where the flat density profile of the coolant in the insulator region is an acceptable match for the subdivided density profile. Simply recalculating the total mass of water in the region has a strong effect. The magnitude of the temperature differential on the nuclear characteristics was not explored. The additional subregions conserve the mass of the water in the insulator region, so figure 4.12 reveals the magnitude of the effect of the location of the light water as about 0.5 mk. The sign of this change is flipped between Serpent and WIMS-AECL. Additional subregions more accurately model the light water as located nearer the moderator than the fuel region of the core. Neutrons moderated by this concentration of the mass of water away from the fuel are less likely to travel to the fuel and participate in another fission reaction.

In chapter 5 the coolant density profile in the subchannels of the coolant region is further explored. The results of this section do not match the results from chapter 4. The reactivity of the system is increased by 3.3 mk by considering the light water massed further from the more energetic fuel cladding in the subchannel. At

this distances, the absorptive properties of the light water dominate the moderation properties, unlike in the region closer to the moderator, though it is unclear why.

The conditions that generate the most significant neutronic effects in the coolant density variations are:

- Large lateral temperature gradient
- Large coolant density variation along this temperature range
- Strong axial dependence for the size of the lateral temperature gradient

Without the large coolant density variation, the coolant density will not vary significantly over the observed range. The coolant under consideration here is light water, which has strong moderation and absorption properties. The reactor is highly sensitive to the density of water in any location in the reactor core. The third point means that the coolant density variations themselves vary along the axial length of the reactor. If there were no significant variations, this would still be a powerful and interesting result, showing another factor in considering the initial reactivity of the reactor, which may have significant effects of various reactivity coefficients. However, if there are powerful axial variations, this further complicates the picture. The effects on the fresh fuel reactivity of the reactor mean that the reactivity of the reactor is not normally constant along the axial length of the reactor, which needs to be approached.[1] In this case, the CVR of the reactor varies by up to 12 mk along the axial length of the reactor, creating additional issues in the event of a large LOCA, where different regions of the reactor see different reactivity changes. None of this analysis considers the effects of any burnup in the reactor.

The Canadian PT-SCWR design has changed designs significantly since this thesis was started, which makes a number of the conclusions no longer directly applicable. In particular, even the version of the PT-SCWR used in the benchmark removes the coolant flow though the insulator region. Further evolutions of the reactor design are even more radical, removing the porous insulator region entirely. The results of this thesis can be used as a preliminary considerations when another reactor design has a similar coolant density variation as the design under consideration in this thesis. The large neutronic considerations when dealing with the large coolant density changes in any super-critical water reactor must be investigated thoroughly for any design type. The quantitative results of the subchannel analysis are also problematic, as the CFD model used was not thoroughly vetted by Dr Rashkovan. The finest mesh of 0.15 mm$\times$0.15 mm was on average 3.3 mk higher than the constant coolant density model.

[1] The 'simple' answer to this problem would seem to be poison or enrichment variations to even out the reactivity

1,000,000 cells involves a very large computational time, 21:34 hours. As such, the only other comparable cell size is performed with 100×100 cells. It is unclear if 1,000,000 cells is sufficient to encompass the subchannel considerations, or if further subdivisions are required, with the corresponding increase in calculation time. The linear element rating in Figures 5.2 - 5.4 on 71 indicates the pin power profile for the fine cell structure continues to have a weaker axial dependence than for the coarser cell structures. This is likely because the consideration of the subchannels reduces the 'shielding' of denser light water around the inner ring of fuel elements, allowing them to interact at all stages of the reactor. The LER is highest in the finest grid in the middle element for reasons unknown.

This thesis also attempted to answer the validity of using Serpent or Serpent 2 as a code for work with the PT-SCWR. The results against the benchmarking study in chapter 3 indicate that both Serpent and Serpent 2 are equally valid and useful codes, though the continued discrepancies against the other Serpent code by l'École Polytechnique de Montréal indicate that more research is needed. This is almost certainly an issue with the differences in the libraries used, which is another avenue of future sensitivity research. All versions of the code used the ENDF/B-VII.0, but a difference in the encoding, as seen on page 37 suggests another factor at play. Of note, the file used in l'École Polytechnique de Montréal's work was not found in the Serpent available for this work. The source of this is unknown, but likely minor.

6.1 Future Work

This thesis suggests a great deal of useful future work to extend and validate its conclusions. A CFD model should be generated and validated to create a more accurate picture of the lateral coolant density profile in the insulator region, to determine if the effect described in the model continues to exist in a more sophisticated model. Additionally, the added technology of the multi-physics interface in Serpent 2 allows the actual density of the coolant to be used in the lattice code in a more rigorous manner than simply subdividing into merely ten different subdivisions. Determining the fuel burnup profile of the reactor with these considerations would be a difficult task, as the reactor is now heavily unbalanced in reactivity from the top to the bottom of the reactor. Whether a poison or negative reactivity devices are used to counteract this unbalanced reactivity, the burnup rates and burnup profiles could be heavily affected.

The subchannel analysis, using a more advanced CFD model with a finer mesh, could be used to generate a finer coolant density gradient in the multi-physics interface of Serpent 2, to determine if the finer mesh continues to generate powerful subchannel effects on the reactivity of the reactor, as the current work did not reach

the law of diminishing returns on the effect of smaller cell sizes. Testing with additional cell sizes may find counter-intuitive results if the cell sizes are too small for the assumptions used in the codes. This thesis did not explore the problem space sufficiently to know if this may or may not be an issue.

Thermal-hydraulic and neutronic coupling is when a CFD code and a lattice physics code are arranged such that each use the outputs of the other code as an input. "The traditional approach for code coupling in nuclear engineering is based on loose coupling where individual validated codes perform their respective calculation and exchange information at specified points." [26] This is not the method used in this thesis, where the output of the CFD is used as a one-way input into the lattice physics code SERPENT. The information gleaned from SERPENT is not passed back to FLUENT. This is mentioned as a potential method of improvement.

In all of these codes, it was only investigated at five equally spaced axial positions. These axial positions are not necessarily the most interesting positions to investigate. Instead, there should be a tight spacing of measurements around the pseudo-critical transition region, as it occurs in the coolant region and anywhere with the coolant. The transitionary period around the pseudo-critical region needs to be investigated further. Reactivity effects around this region may further change the assumptions regarding the enthalpy transfer to the coolant, requiring a truly coupled CFD and neutron physics lattice codes.

Bibliography

[1] C. Chow and H. Khartabil, "Conceptual Fuel Channel Designs for CANDU-SCWR," *Nuclear Engineering and Technology*, vol. 40, no. 2, pp. 139–146, 2007.

[2] Y. Nakahara, K. Suyama, J. Inagawa, R. Nagaishi, S. K. an Nobuaki Kohno, M. Onuki, and H. Mochizuki, "Nuclide Composition Benchmark Data for Verifying Burn-up Codes on Light Water Reactor Fuels," vol. 137, no. 2, pp. 111–126, 2002.

[3] (2013, Oct) The Generation IV International Forum. [Online]. Available: www.gen-4.org

[4] "GIF R&D Outlook for Generation IV Nuclear Energy Systems," Generation IV International Forum, Tech. Rep., 2009.

[5] L. H. K. Leung, "A Next Generation Heavy Water Nuclear Reactor with Supercritical Water as Coolant," in *International Conference on Future of Heavy Water Reactors*. Ottawa, 2011.

[6] D. R. Novog, "Introduction to Super Critical Water Reactor GEN IV Concepts," in *The 9th Seminar and Training on Scaling, Uncertainty, and 3D Coupled Code Calculations in Nuclear Technology*. Amsterdam, 2008.

[7] M. H. McDonald, B. Hyland, H. Hamilton, L. H. K. Leung, N. Onder, J. Pencer, and R. Xu, "Pre-Conceptual Fuel Design Concepts for the Canadian Super Critical Water-Cooled Reactor," in *The 5th International Symposium on Supercritical Water-Cooled Reactors (ISSCWR-5)*. Vancouver, 2011.

[8] J. Pencer and L. Blomley, "A Preliminary SCWR 2D Lattice-Level Benchmark Comparison of WIMS-AECL and MCNP," AECL Internal Report 217-123700-REPT-005.

[9] Jeremy Pencer, *SCWR 78-Element Bundle Reference Model, Revision 0*, Atomic Energy of Canada Limited, 2011, AECL Internal Report 217-123700-REPT-001.

[10] H. Reutler and G. Lohnert, "Advantages of going modular in htrs," *Nuclear Engineering and Design*, vol. 78, no. 2, pp. 129–136, April 1984.

[11] J. Kang and F. von Hippel, "U-232 and the Proliferation-Resistance of U-233 in Spent Fuel," vol. 9, pp. 1–32, 2001.

[12] J. Pencer, D. Watts, A. Colton, X. Wang, L. Blomely, V. Anghel, and S. Yue, "Core Neutronics for the Canadian SCWR Conceptual Design," Atomic Energy of Canada Limited, Shenzen, Guangdong, China, 6th International Symposium on Supercritical Water-Cooled Reactors ISSCWR-6, March 2013.

[13] D. Hummel, S. Langton, M. Ball, D. Novog, and A. Buijs, "Description and Preliminary Results of a Two-Dimensional Lattice Physics Code benchmark for the Canadian Pressure Tube Supercritical Water-cooled Reactor (PT-SCWR)," in *The 6th International Symposium on Supercritical Water-Cooled Reactors*. ISSCWR-6, March 2013.

[14] G. Marleau, G. Harrison, H. Raouafi, A. Rouchon, and T. Benguedouar, "Evaluation of the 2-D SCWR Benchmark using SERPENT, TRIPOLI and DRAGON," École Polytechnique de Montréal, Benchmark, November 2012.

[15] J. Pencer and B. Hyland, "PHYSICS ASPECTS OF THE PRESSURE TUBE TYPE SCWR PRECONCEPTUAL DESIGN," Atomic Energy of Canada Limited, Proceedings of the International Conference of the Future of HWRs, October 2011.

[16] J. Pencer, D. Watts, A. Colton, X. Wang, L. Blomeley, V. Anghel, and S. Yue, "Core Neutronics for the Canadian SCWR Conceptual Design," Atomic Energy of Canada Limited, ISSCWR6-13021, March 2013.

[17] M. H. McDonald, "Fuel and Core Physics Considerations for a Pressure Tube Supercritical Water Cooled Reactor," Master of Applied Science, McMaster University, October 2011, Open Access Dissertations and Theses, Paper 6207.

[18] J. Duderstadt and L. Hamilton, *Nuclear Reactor Analysis*. John Wiley and Sons, Inc, 1976.

[19] L. Russel, "Simulation of time-dependent neutron populations for reactor physics applications using the geant4 monte carlo toolkit," Master's Thesis, McMaster University, 2012.

[20] J. Lamarsh and A. Baratta, *Introduction to Nuclear Engineering*, 3rd ed., 2001.

[21] J. Leppänen, *Serpent - a Continuous-energy Monte Carlo Reactor Physics Burnup Calculation Code User's Manual*, VTT Technical Institute.

[22] D. Altiparmakov, "New Capabilities of the Lattice Code WIMS-AECL," in *International Conference on the Physics of Reactors, Nuclear Power: A Sustainable Resource*. PHYSOR, 2008.

[23] G. Jonkmans, *WIMS-AECL Version 3.1 User's Manual*, istp-05-5115 ed., CANDU Owner's Group Inc., August 2006.

[24] D. Altiparmakov, "ENDF/B-VII.0 Versus ENDF/B-VI.8 in CANDU Calculations," in *PHYSOR 2008 - Advances in Reactor Physics to Power the Nuclear Renaissance*. PHYSOR, 2010.

[25] J. Leppänen, *PSG2 / Serpent a Continuous-energy Monte Carlo Reactor Physics Burnup Calculation Code*, RSICC Computer Code Collection, September 2009.

[26] M. Vazqueza, H. Tsige-Tamiratb, L. Ammirabileb, and F. Martin-Fuertesa, "Coupled neutronics thermal-hydraulics analysis using Monte Carlo and subchannel codes," no. 250, pp. 403–411, June 2012.

[27] E. Woodcock, T. Murphy, P. Hemmings, and C. Longworth, "Techniques used in the GEM code for Monte Carlo neutronics calculations in reactors and other systems of complex geometry," 1965.

[28] J. Leppänen, "Performance of Woodcock delta-tracking in lattice physics applications using the Serpent Monte Carlo reactor physics burnup calculation code," January 2010.

[29] ——. (2014, February) On-going Work and Future Plans: Serpent 2. VTT Technical Research Centre of Finland. [Online]. Available: {http://montecarlo.vtt.fi/development.htm},

[30] D. Lokuliyana, "SIMULATING SCWR THERMAL-HYDRAULICS WITH THE MODIFIED COBRA-TF SUBCHANNEL CODE," MASc Thesis, McMaster University, 2014.

[31] A. Rashkovan, "Email Communications with Alex Rashkovan," 2012-2013.

[32] P. G. Boczar, W. Shen, J. Pencer, B. Hyland, P. Chan, and R. Dworshak, "Reactor Physics Studies for a Pressure Tube Supercritical Water Reactor (PT-SCWR)," in *The 2nd Canada-China Joint Workshop on Supercritical Water-Cooled Reactors*. Toronto: CCSC-2010, 2010.

[33] W. Shen, "Assessment of the traditional neutron-diffusion core-analysis method for the analysis of the Super Critical Water Reactor," *Annals of Nuclear Energy*, 2012.

[34] D. Grcić, R. Ječmenica, and D. Pevec, "Lattice codes pin power prediction comparison," *Nuclear Engineering and Design*, pp. 27–40, 2012.

[35] M. Scriven, D. Hummel, D. Novog, and J. Luxat, "Analysis of the Impact of Coolant Density Variations in the High Efficiency Channel of a Pressure Tube Super Critical Water Reactor," in *3rd China-Canada Joint Workshop on Supercritical-Water-Cooled Reactors*, no. 12010, April 2012.

[36] D. Hummel and D. Novog, "FUEL COMPOSITION OPTIMIZATION IN A 78-ELEMENT FUEL BUNDLE FOR USE IN A PRESSURE TUBE TYPE SUPERCRITICAL WATER-COOLED REACTOR," in *CCSC-2012*, no. 12015, April 2012.

[37] G. Harrison and G. Marleau, "Computation Of A Canadian SCWR Unit Cell With Deterministic And Monte Carlo Codes," l'École Polytechnique de Montréal, PHYSOR 2012 Advances in Reactor Physics, April 2012.

[38] J. Shan, W. Chen, B. W. Rhee, and L. K. Leung, "Coupled neutronics/thermalhydraulics analysis of CANDUSCWR fuel channel," 2010.

[39] A. Ahmad, L. Cao, and H. Wu, "Coupled analysis and improvements for Canadian-SCWR core design," 2014.

[40] K. Jareteg, P. Vinai, and C. Demazire, "Fine-mesh deterministic modeling of PWR fuel assemblies: Proof-of-principle of coupled neutronic/thermalhydraulic calculations," 2014.

[41] J. Feng, B. Zhang, J. Shan, and L. Wang, "Optimization of 54-element pressure tube SCWR bundle through neutronics/thermalhydraulics coupling analysis," 2014.

[42] W. Liu, Y. Zhu, N. Bai, J. Shan, and B. Zhang, "Coupled neutronics/thermalhydraulics analysis of PTSCWR fuel channel," in *ISSCWR-6*, March 2013.

[43] X. Liu, T. Yang, and X. Cheng, "Core and sub-channel analysis of SCWR with mixed spectrum core," 2010.

[44] National Institute of Standards and Technology. (2012, January) Refprop. [Online]. Available: http://www.boulder.nist.gov/div838/theory/refprop/MINIREF/MINIREF.HTM

[45] *FlexPDE User Guide*, PDE Solutions Inc, 2005.

[46] W. Woodside, "Calculation of the Thermal Conductivity of Porous Media," *Canadian Journal of Physics*, vol. 36, no. 7, pp. 815–823, July 1958.

[47] K. W. Schlichting, N. P. Padture, and P. G. Klemens, "Thermal Conductivity of dense and porous Yttria-stablized Zirconia," *Journal of Materials Science*, vol. 36, pp. 3003–3010, 2001.

[48] B. Lin and B. Wuebben. (1995, March) dos2unix. [Online]. Available: http://linuxcommand.org/man_pages/dos2unix1.html

Appendices

Appendix A

Using the thermal-hydraulic results in Serpent 2

The output generated from Fluent is in the following space delimited form:

```
num xcoord ycoord zcoord xvel yvel zvel temp xcoord ycoord zcoord
1 4.585915804E-002 4.906649515E-002 5.816975608E-003
4.185581740E-003 -2.810817346E-003 1.269116030E+000 6.248154769E+002
4.593977954E-002 4.897792227E-002 5.820114150E-003
```

The 2nd set of geometric co-ordinates is the central co-ordinate of a given cell, and is the positional co-ordinates used. Notably, only the temperature value is an output from Fluent, it must be converted to the density. To reduce computational time a lookup table was used to transform the FLUENT temperatures to density.

MATLAB scripts were used to parse the FLUENT data into the required format for SERPENT input. The re-formating was done in 2-stages to allow for intermediate verification. First the Matlab 2007b script GenGeo trims the input data to a just the geometric position and density of the points that will used in Serpent 2. A second script, GenGeoS2 is used to perform the final steps to set the final formatting. This script is split into two to allow an intermediate check.

GenGeo performs a number of necessary functions. This script takes the output from Fluent and imports it into Matlab. It then trims the data to only the output results within 5 cm[1] of the axial location selected. As Fluent outputs the data in terms of temperature, a Microsoft Excel file converts the Temperature input of each datapoint to a density. This .xls file can be coded as fine as necessary using miniREFPROP. The Fluent CFD analysis was performed with a 1/6 symmetry. The data points are extended to cover the entire slice. The is accomplish first by flipping the data over one axis, then copy+rotating the points twice by $\frac{2\pi}{3}$. The script then outputs a single text file containing the X and Y co-ordinates with a matching density for a given axial location. Different axial locations are stored in different text files.

[1] 5 cm is selected as each slice of data output from Fluent is within 10 cm of each other

The first paragraph, lines 2-8, of GenGeo opens and reads the dataset provided by Dr Rashkovan. Of note, this code has the axial location hard-coded on line 7, and must be modified each time a different axial location is desired.

Lines 10-13 access a reference excel file named 'interpolate', which allows the MATLAB script to convert from Temperature (K) to density ($\frac{kg}{m^3}$) for H_2O at 25 MPa. This excel file is included in the thesis in Appendix D.

Lines 15-22 identify each cell with an index number, then it selects each cell that is located near the selected axial location. The distance of 0.05 m was chosen through trial and error, by noting what distance would always allow a large number of data points.

Lines 24-30 takes all the selected data points, and reads their X and Y co-ordinates and temperature, converting to the density through the interpolation file.

Lines 32-46 converts the 1/6th symmetry provided in the Fluent files to a full region, through a combination of rotation and mirroring over an axis.

Lines 48-50 return the data into a form of solely the X and Y co-ordinates along with the density information, which is all that the Serpent 2 multi-physics interface requires.

Lines 54-57 outputs the results into a text file, which leads into GenGeoS2.

The Matlab script GenGeoS2, shown in Appendix A.2, converts this data list of coordinates and density information into the format readable by Serpent 2's multi-physics interface. GenGeoS2 uses the output file generated by the previous script. The number of cells in the coolant region are defined by the total number along a given axis. The distance between the centres two diagonally adjacent cells are calculated, this is required for a Serpent 2 option below. The X and Y coordinates of the centre of each cell are defined, along with the boundaries. Each datapoint from the previous script is imported, and placed into a cell. The densities of each datapoint in a cell are averaged. The script now has an X and Y coordinate as well as a density for each cell. An example output from this script is given below:

```
1 cool 0
2 1.065000e+001 1
4
-3.750000e-000 -3.750000e-000 -5.484391e-001 -1
3.750000e-000 -3.750000e-000 -5.497376e-001 -1
-3.750000e-000 3.750000e-000 -5.484391e-001 -1
```

```
3.750000e-000 3.750000e-000 -5.497376e-001 -1
```

This output is formatted as the *.in input file used by Serpent 2, and can be used directly as part of the multi-physics interface[2].

Lines 4-10 of the GenGeoS2 script defines the size of the grid being used for this section. The number of cells in the X and Y co-ordinate are hard-coded, and must be changed manually each time the code is run.

Line 14 is a hard-coded constant, showing the maximum radius a cell could possibly have.

Lines 16-17 determine the maximum amount of distance[3] between a point and its nearest neighbour.

Line 18 opens the text file generated by the MATLAB script GenGeo.

Lines 19-24 print off the header information for the Serpent 2 multi-physics interface file. This informations includes the material type ('cool'), the number of cells to follow and the distance Serpent will search for density data in the coolant region.

Lines 26-51 is a loop which runs across the entire grid of X and Y co-ordinates once, averaging the data to determine the density mean and geometric centroid in the given cell. This value is then outputed the format for Serpent 2.

Note the co-ordinate and density units being converted in lines 43-45, as Serpent 2 uses cm and $\frac{g}{cm^3}$, instead of m and $\frac{kg}{m^3}$

As this code is being run in a DOS machine, and Serpent 2 runs in Unix, a program called dos2unix is used to correct for the difference in endline formatting.[48]

A.1 MATLAB Script GenGeo

```
1
2  fileName = 'prelim.txt';
3  fid = fopen(fileName);
4  fgetl(fid); %ignores reading the header
```

[2]In this thesis, the MATLAB script was run in a DOS environment. Serpent 2 was run in a UNIX environment. A DOS-UNIX converter was required, as newline's in DOS are in the form \r\n, while Unix uses \n

[3]The value is intentionally over-reported, in anticipation of any unexpected entries

```
A = fscanf(fid, '%g %g %g %g %g %g %g', [11 inf]);
fclose(fid);
location = 4.5; %The axial location, in metres
%This creates 11 rows in the matrix 'A' containing all data

INTX = xlsread('interpolate','A1:A44');
INTY = xlsread('interpolate','B1:B44');
%interpolate is an excel file with the
%density of water for a given temperature

CellNum = A(1,:);
ZXC = A(11,:);
%A list of the axial position of every
%measurement in the input file

index = ZXC <= location+0.05 & ZXC >= location-0.05;
%This grabs only the data points within a certain range
%of the targeted axial location

XC = A(9,index);
YC = A(10,index);
ZC = A(11,index);
TC = A(8,index);
DC = interp1(INTX,INTY,TC);
%The positional and temperature data for all datapoints
%Converts the Temp to Density

XC = cat(2,XC,XC);
YC = cat(2,YC,-YC);
DC = cat(2,DC,DC);
%Doubles the number of points along the x-axis symettry

Slice1 = cat(1,XC,YC,DC);
%Points from -pi/3 to pi/3
Slice2 = cat(1,(XC.*cos(2*pi/3)-YC.*sin(2*pi/3)),
            (XC.*sin(2*pi/3)+YC.*cos(2*pi/3)),DC);
%Rotatation of previous slice
Slice3 = cat(1,(XC.*cos(4*pi/3)-YC.*sin(4*pi/3)),
            (XC.*sin(4*pi/3)+YC.*cos(4*pi/3)),DC);
%Final rotation of slice
Geometry = cat(2,Slice1,Slice2,Slice3);
%Combines the pieces to correct for 1/6 cell modelled

XC=Geometry(1,:);
YC=Geometry(2,:);
DC=Geometry(3,:);

scatter(XC,YC);

fileID = fopen('exp.txt','w');
fprintf(fileID,'%6.2f %12.10f\n',ZXC);
fclose(fileID);
%output file of the geometry
```

A.2 MATLAB Script GenGeoS2

```

% Take data from the X,Y,D Data Set

NumXCells = 1000; %Total number of cells in X direction
NumYCells = NumXCells;
%Total number of cell in Y direction
%Must be square
TotalCells = NumXCells * NumYCells;
%pitch is defined by total size divided by total
%number of cells in a given direction

%Max distance from origin (radius)

Radius=0.075;

pitch = 200 * Radius / NumXCells; %ouputs in cm
pitchcalc=1.42*pitch;
fileID=fopen('outfile.txt','wt');

fprintf(fileID,'%s\n','1 cool 0');
fprintf(fileID,'%s %d %s\n','2',pitchcalc,'1');
%Generate Lattice

fprintf(fileID,'%d\n',TotalCells);

```

```
26  for j=1:NumYCells
27    for i=1:NumXCells
28      k=i+(j-1)*NumXCells;
29
30      %Here is the calculation for density of a specific cell
31      index = XC >= -Radius + (i-1)*pitch
32       & XC <= -Radius + i*pitch
33       & YC >= -Radius + (j-1)*pitch
34       & YC <= -Radius + j*pitch;
35      %Need to look for lines in Geometry
36      %where X and Y satisfy some value
37      %Average the DC in those lines
38      %If no lines exist, set to 0?
39
40      if max(index) == 1
41        xcentre = -Radius+(i-0.5)*pitch;
42        ycentre = -Radius+(j-0.5)*pitch;
43        %xcentre = 10*mean(XC(index));
44        %ycentre = 10*mean(YC(index));
45        density = mean(DC(index))/1000;
46        %End of calculation
47      fprintf(fileID,'%d %d %d %s\n',xcentre,
48                ycentre, -density,'-1');
49      end
50
51    end
52  end
```

Appendix B

Operation of Serpent

This section discusses some of the advantages and disadvantages of Serpent, and some of the lessons learned in its application. The material identifier cards defined in ENDF format permit materials with temperatures of 300 K, 600 K, 900 K, etc. If a material is at a temperature outside of these values, the nuclide identifier selected must be of an ENDF-defined value *below* the true material temperature, with the true value defined as part of the material. The doppler broadening calculation in Serpent will interpolate if invoked using a `tmp` entry in the material card. [21]

Serpent comes with a number of different libraries available: endfb7, endfb68, jef22, jeff31 and jeff311. When specifying the library, one must be careful to also specify the thermal scattering data used for light and heavy water. This is identified by the `therm` input card. An example of this card is reproduced below.

```
therm lwtrC lwe7.12t
therm lwtrM lwe7.00t
therm hwtrM hwe7.00t
```

The `lwtrC` and `lwtrM` distinction is created in order to use a different temperature card for the given material, so the H_2O in one regino does not scatter identically to the H_2O in another region with a different temperature.

The `e7` section of the card identifies which library the thermal scattering data is retrieved from. It must be updated manually if the library for the rest of the lattice cell is updated, as the library definition permits the use of scattering cross-sections from another library.

The `.00t` is the temperature identifier. In order to determine which temperature a given thermal scattering code refers to, it is necessary to refer to the `.xsdata` file for the library. For example, the `lwe7.12t` code refers to a temperature of 600 K, and `lwe7.00t` refers to 294 K. This convention does *not* match the convention for other material cards, and the convention varies depending on which library is selected.

As Serpent is a Monte-Carlo code, the number of cycles and neutrons per cycle simulated must also be defined. For example, in Chapter 3 5000 live cycles with 5000 neutrons each are simulated. An additional 200 'dead' cycles are performed at the start of a simulation, to allow the simulation to approach the true value before recording the results in the final tally.

Appendix C

Additional Figures

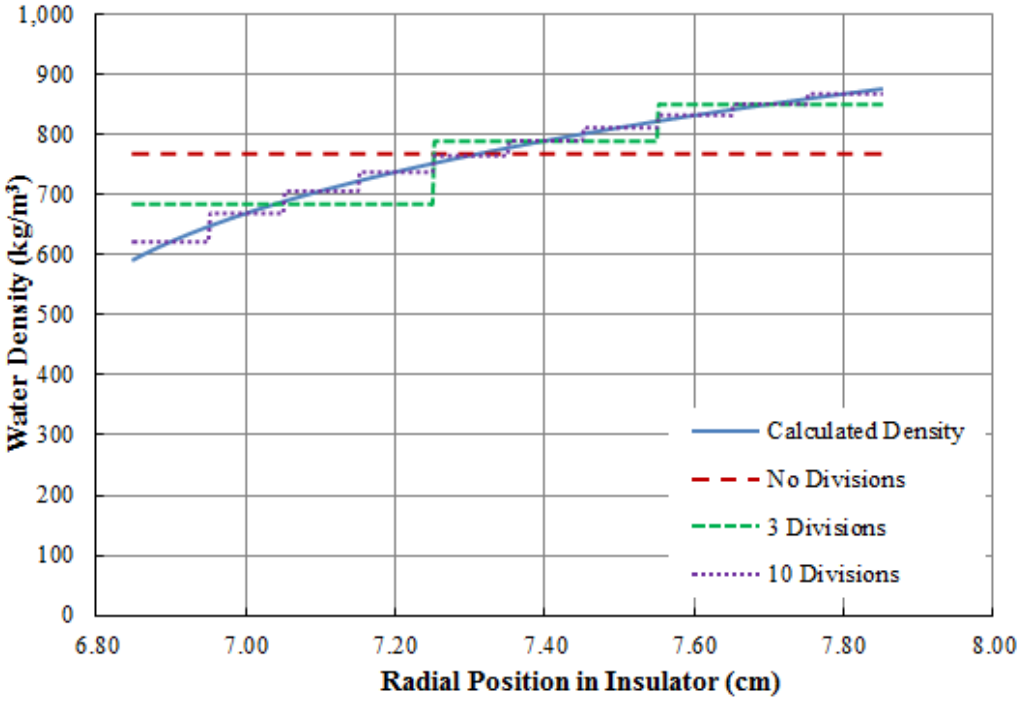

Figure C.1: Calculated density curve with model k(constant) at 0.5m

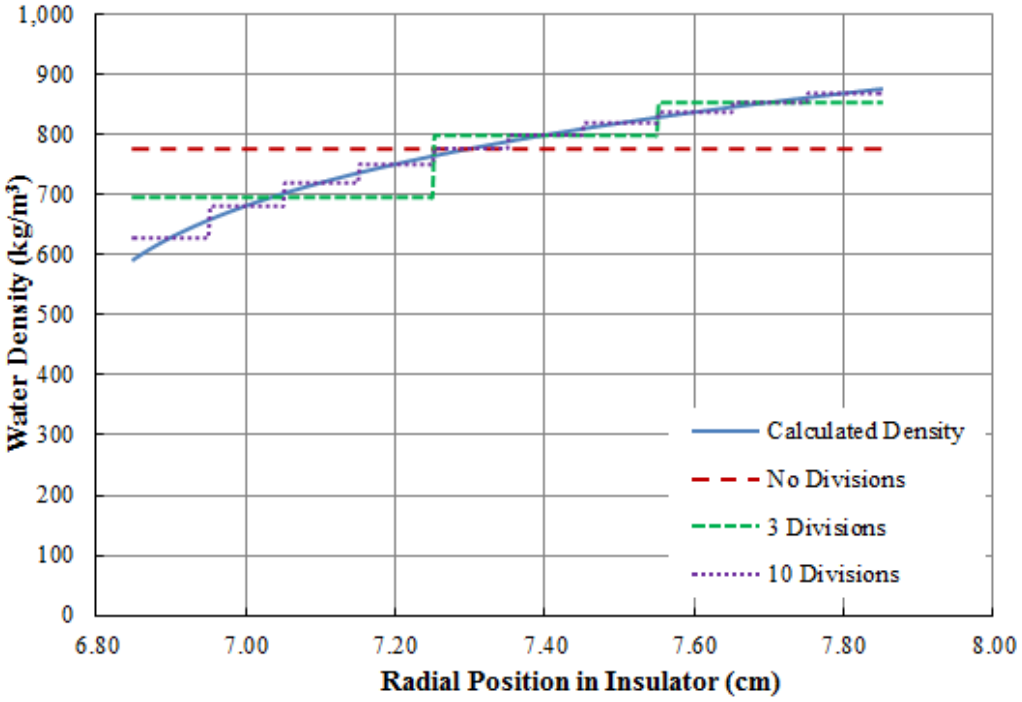

Figure C.2: Calculated density curve with model k(Water) at 0.5m

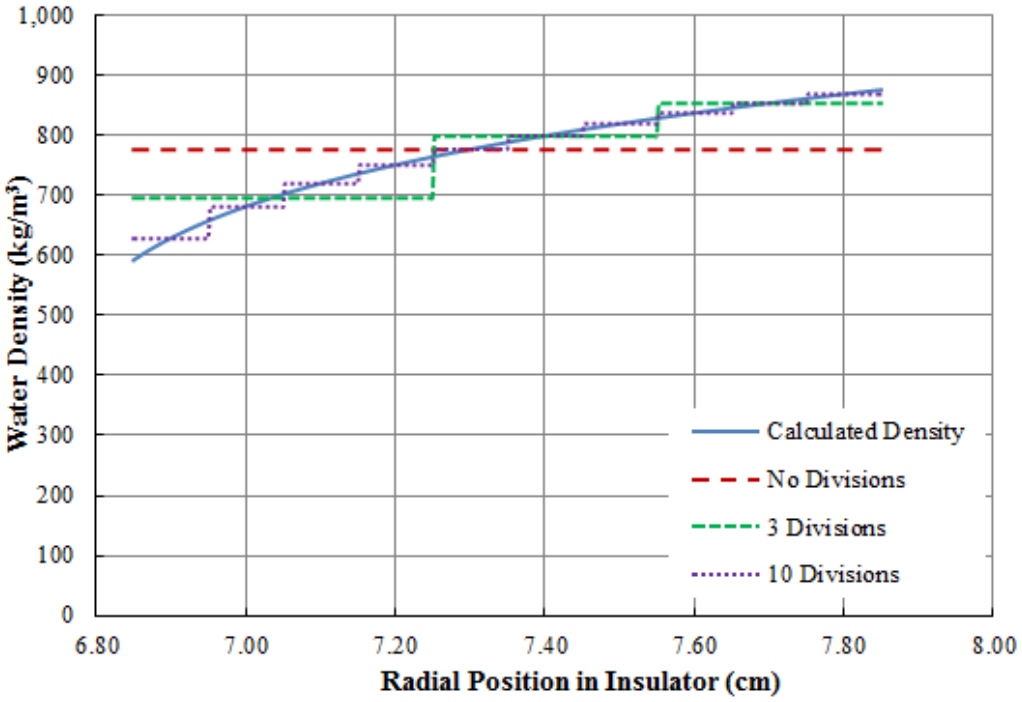

Figure C.3: Calculated density curve with model k(Water-YSZ) at 0.5m

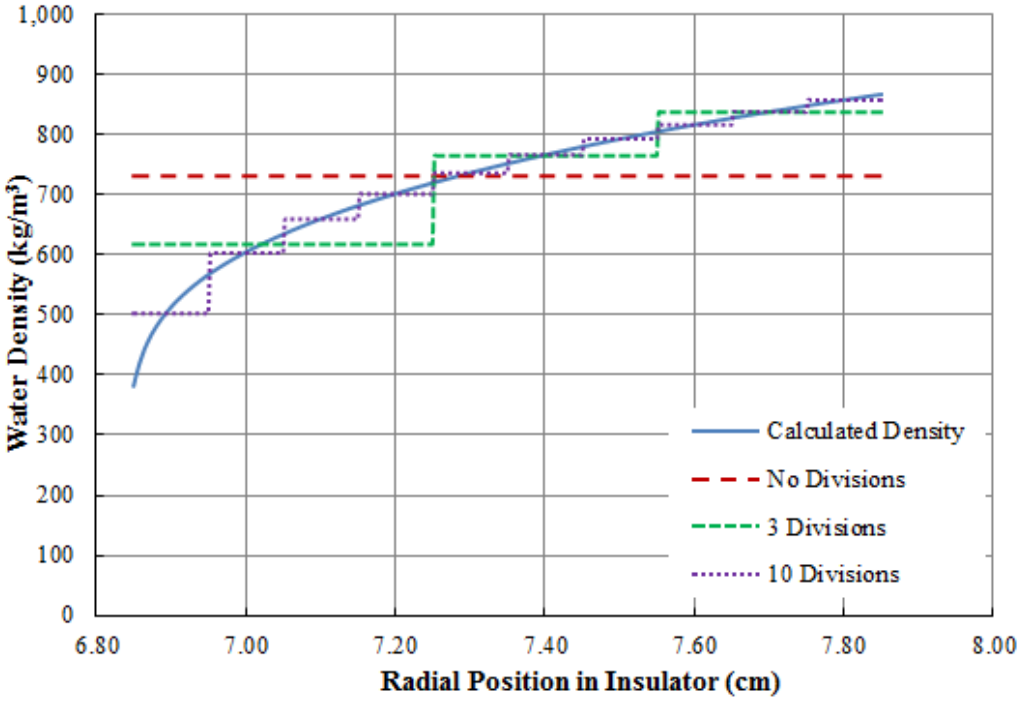

Figure C.4: Calculated density curve with model k(constant) at 1.5m

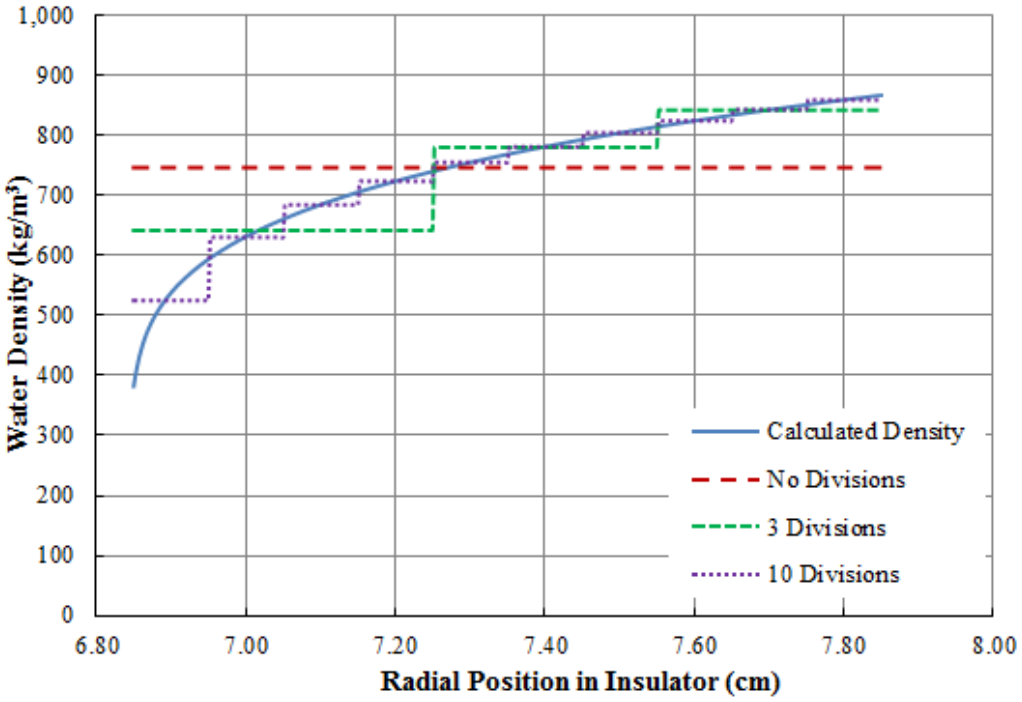

Figure C.5: Calculated density curve with model k(Water) at 1.5m

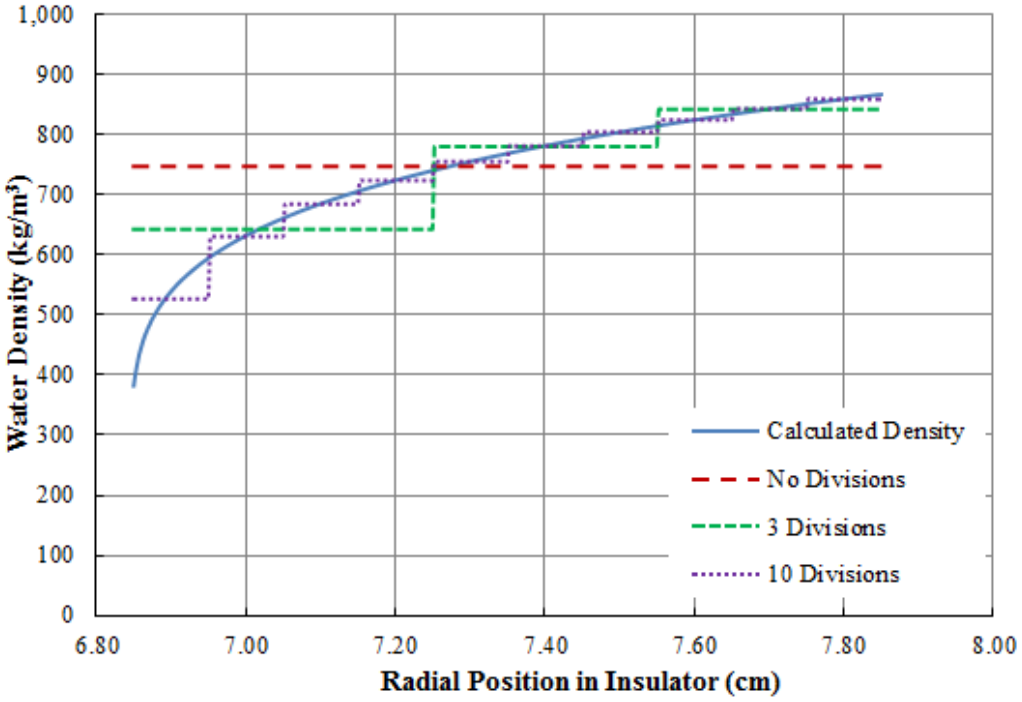

Figure C.6: Calculated density curve with model k(Water-YSZ) at 1.5m

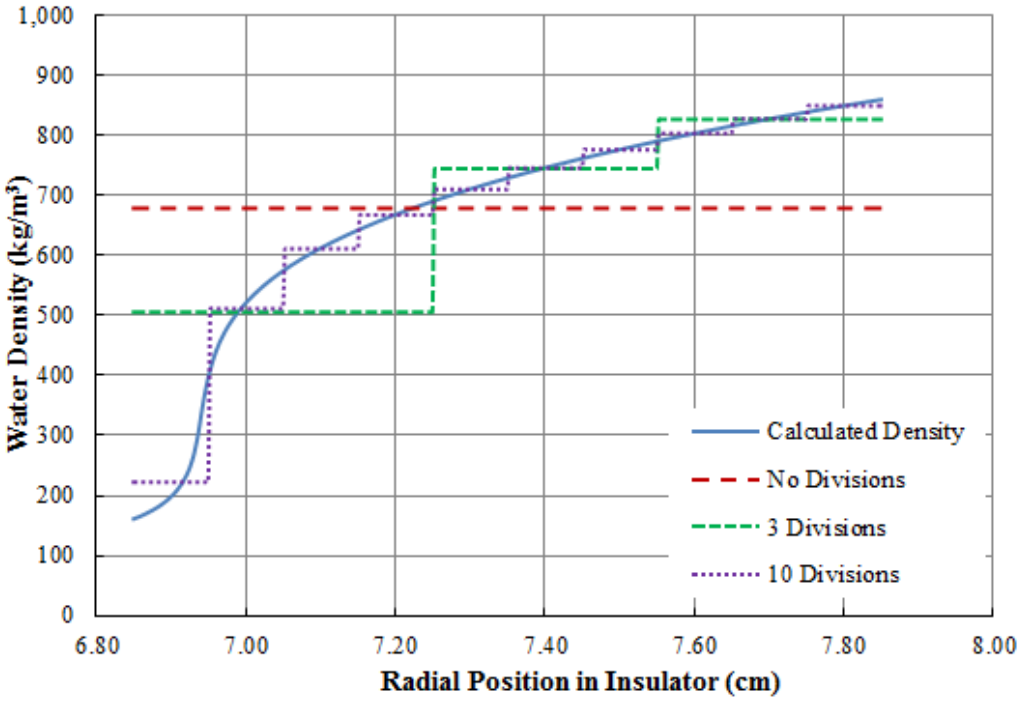

Figure C.7: Calculated density curve with model k(constant) at 2.5m

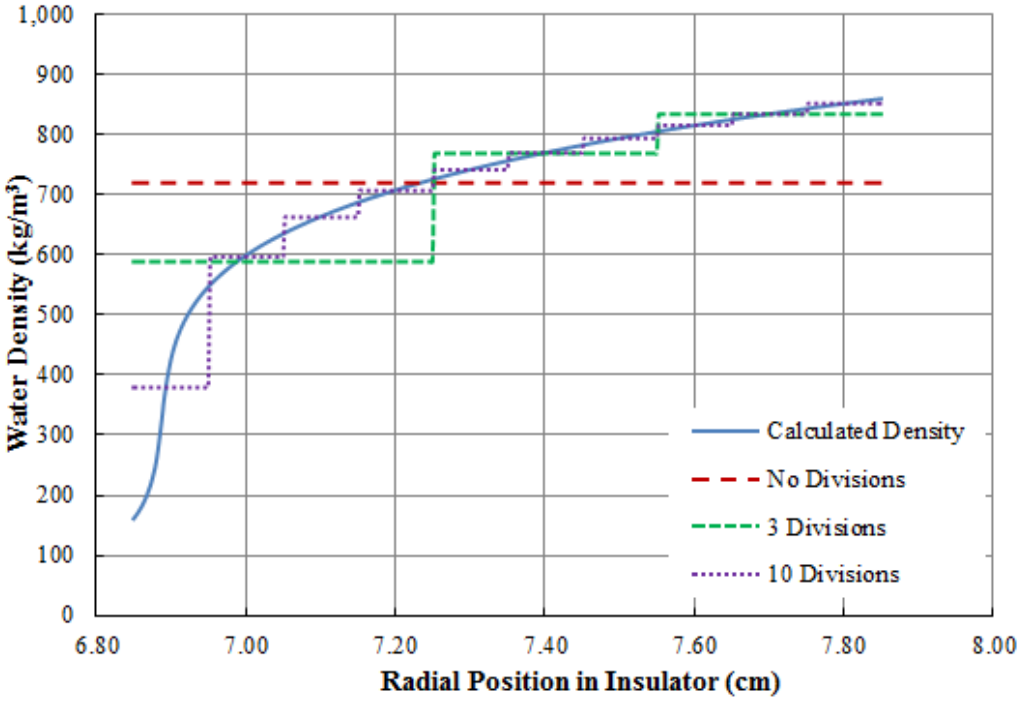

Figure C.8: Calculated density curve with model k(Water) at 2.5m

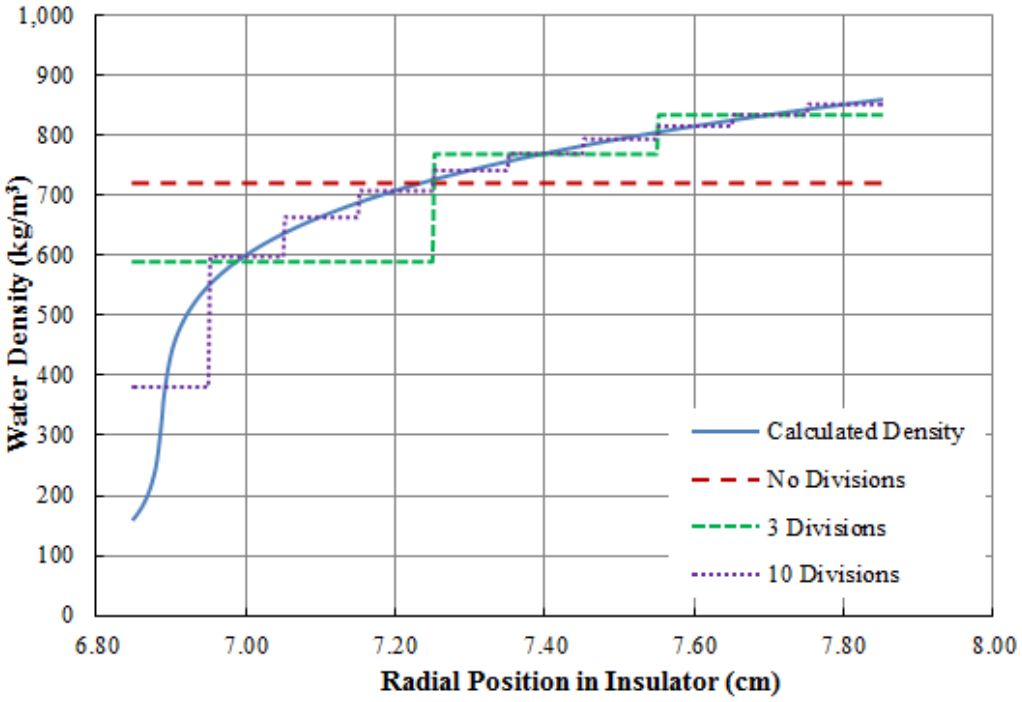

Figure C.9: Calculated density curve with model k(Water-YSZ) at 2.5m

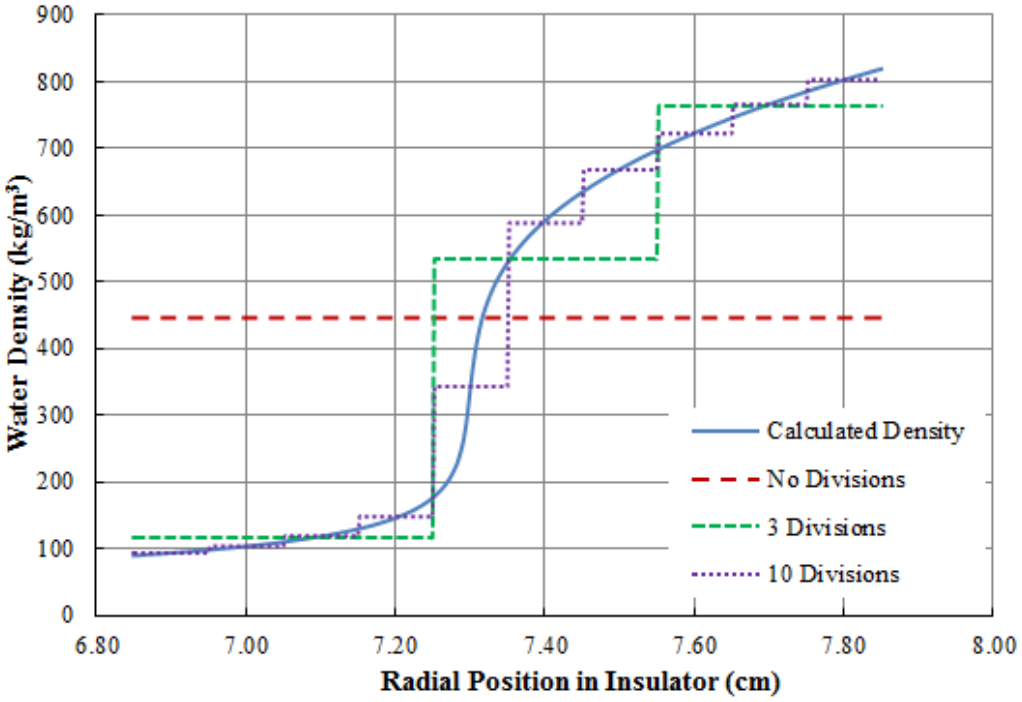

Figure C.10: Calculated density curve with model k(constant) at 3.5m

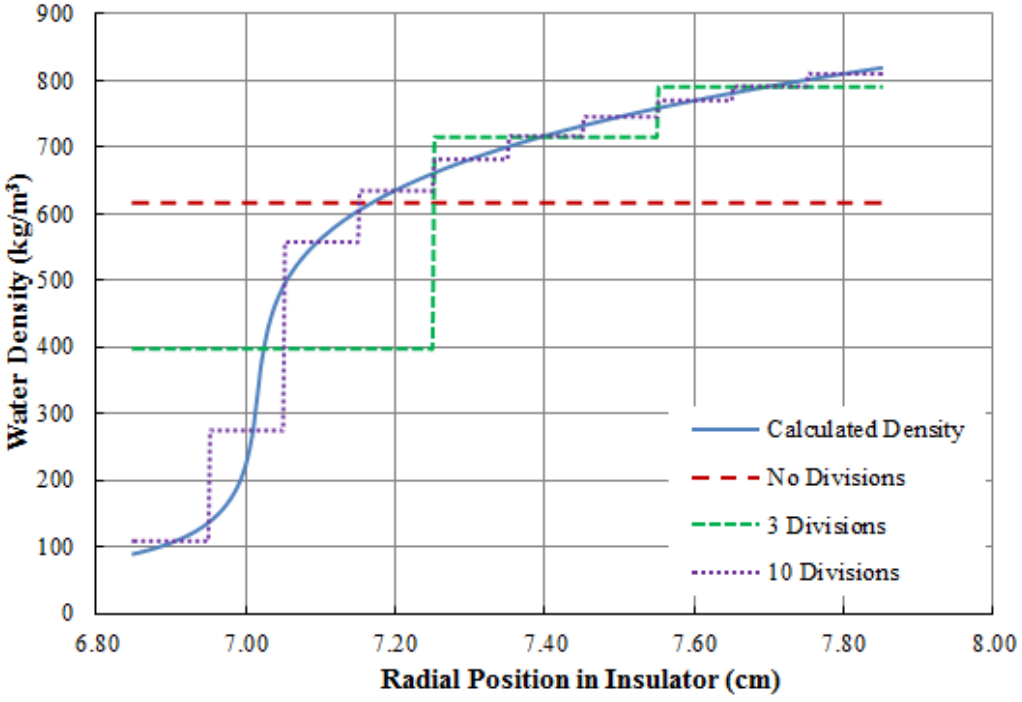

Figure C.11: Calculated density curve with model k(Water) at 3.5m

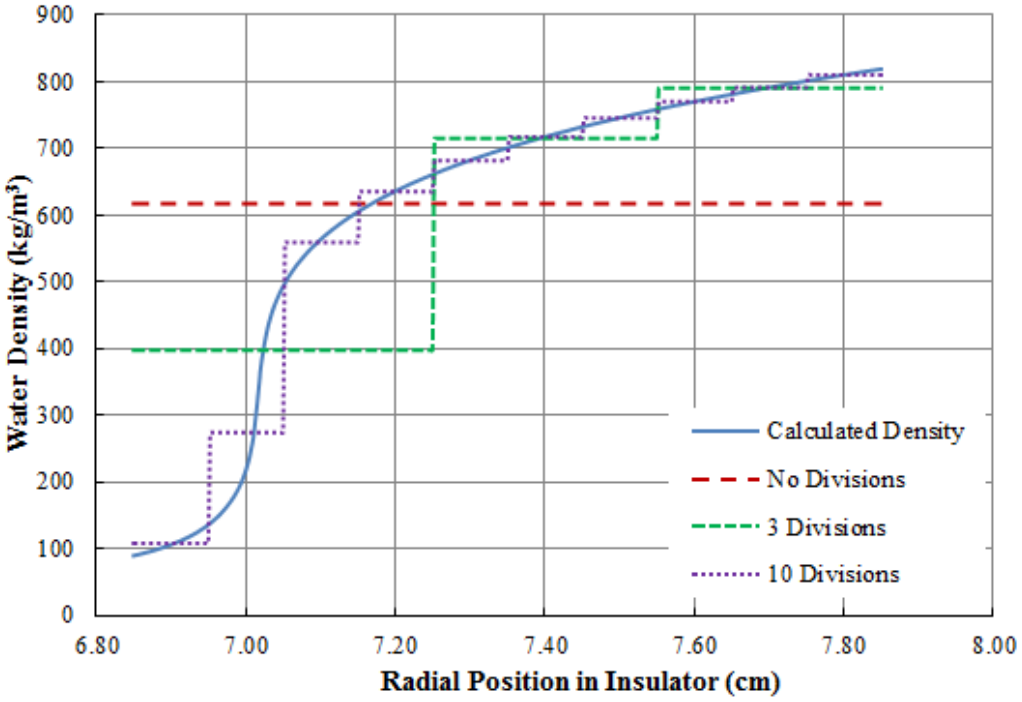

Figure C.12: Calculated density curve with model k(Water-YSZ) at 3.5m

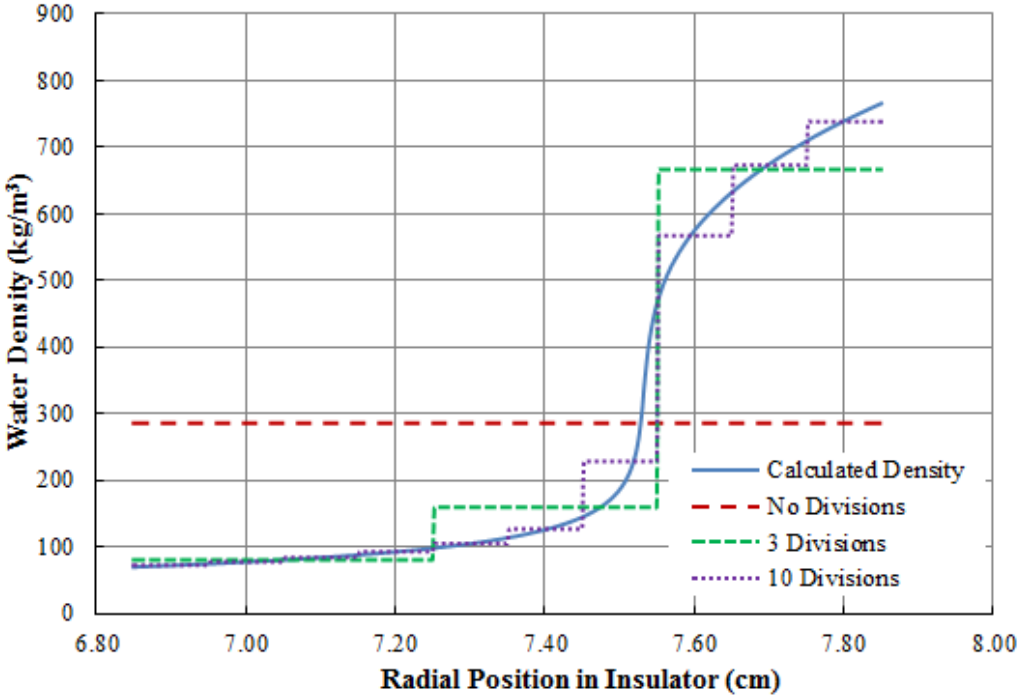

Figure C.13: Calculated density curve with model k(constant) at 4.5m

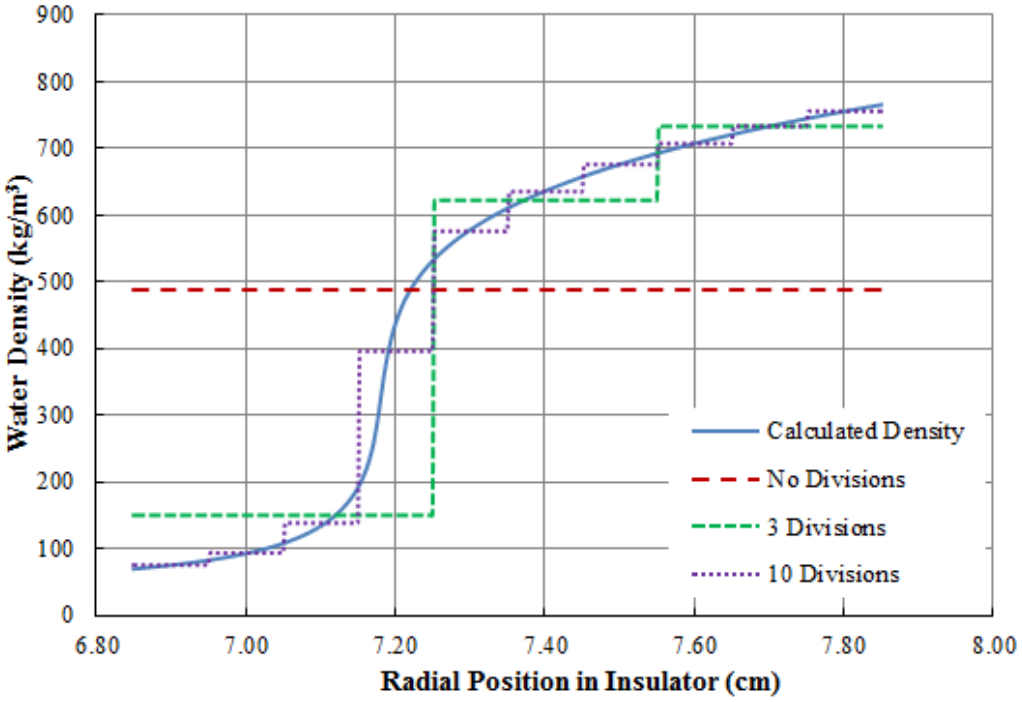

Figure C.14: Calculated density curve with model k(Water) at 4.5m

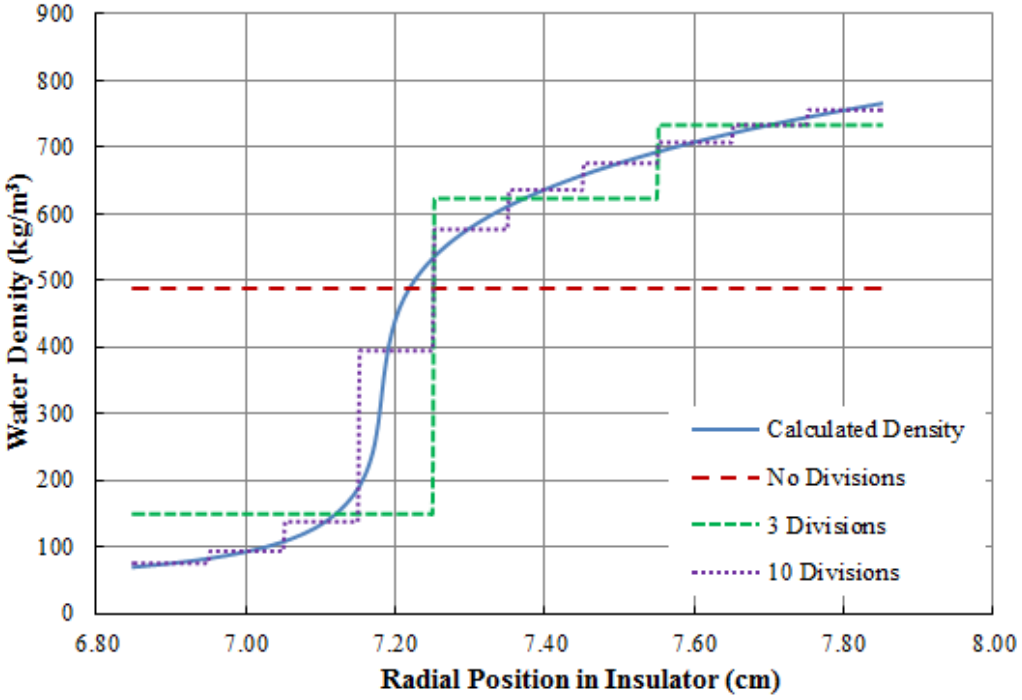

Figure C.15: Calculated density curve with model k(Water-YSZ) at 4.5m

Appendix D

Excel Interpolation

Temperature(K)	Density(kg/cm3)
570	748.69
590	710.18
610	663.56
630	601.64
641	552.69
643	541.36
645	528.78
647	514.59
649	498.19
651	478.47
653	453.08
655	416.56
656	391.30
657	358.91
658	318.86
659	282.76
660	257.66
661	240.04
662	226.88
663	216.55
665	201.00
667	189.55
669	180.55
671	173.18
673	166.96
675	161.60
677	156.89
679	152.70
690	135.62
710	117.11
720	110.74
730	105.46
740	100.98
750	97.098
760	93.681
770	90.637
780	87.896
790	85.408
800	83.132
900	67.367
1000	57.899
1100	51.256
1200	46.213
1300	42.198

Appendix E

Serpent Input Files

E.1 Chapter 3 Input File

```
% ——— SCWR cluster ——————————————————————————————————————————

set title ”SCWR”

% ——— Fuel pin:

pin 1
fuel1  0.62
clad  0.68
cool

pin 2
fuel2  0.62
clad  0.68
cool

pin 3
fuel3  0.35
clad  0.41
cool

pin 4
PINCEN 2.82
clad2 2.88
cool

% ————————————————
% Rings description
% ————————————————
lat      10   4   0.0   0.0   1   % Central pin
1    0.0    0.0          4

lat      11   4   0.0   0.0   1   % Inner ring
15   3.66   15.0         1 1 1 1 1 1 1 1 1 1 1 1 1 1 1

lat      12   4   0.0   0.0   1   % Middle ring
21   5.11   10.0         2 2 2 2 2 2 2 2 2 2 2 2 2 2 2 2 2 2 2 2 2

lat      13   4   0.0   0.0   1   % Outer ring
42   6.30   7.5          3 3 3 3 3 3 3 3 3 3 3 3 3 3 3 3 3 3 3 3 3 3 3 3 3 3 3 3 3 3
3 3 3 3 3 3 3 3 3 3 3 3

% ———————————————
% Cell description
% ———————————————
surf 1  cyl  0.0  0.0    2.930   % Virtual surface bwt Central Pin and Inner Ring
surf 2  cyl  0.0  0.0    4.385   % Virtual surface bwt Inner Ring and Middle Ring
surf 3  cyl  0.0  0.0    5.840   % Virtual surface bwt Middle Ring and Outer Ring
surf 4  cyl  0.0  0.0    6.800   % Liner tube inner radius
surf 5  cyl  0.0  0.0    6.850   % Liner tube outer radius / Insulator inner radius
surf 6  cyl  0.0  0.0    7.850   % Insulator outer radius  / Pressure tube inner radius
surf 7  cyl  0.0  0.0    9.050   % Pressure tube outer radius
surf 8  sqc  0.0  0.0   12.500   % 25 cm square lattice pitch

cell 1 0 fill 10          −1  % Central pin
cell 2 0 fill 11       1  −2  % Inner ring
cell 3 0 fill 12       2  −3  % Middle ring
cell 4 0 fill 13       3  −4  % Outer ring
cell 5 0 liner         4  −5  % Liner tube
cell 6 0 ins           5  −6  % Insulator region
cell 7 0 Ptube         6  −7  % Pressure tube
cell 8 0 moder         7  −8  % Moderator
cell 9 0 outside       8      % Outside world
```

```
% PINCEN

mat PINCEN   -5.37
40000.06c  -72.3
8016.06c   -27.6884985883
8017.06c   -0.0115014117

% --- Fuel (Pt/Th Mixture):

mat fuel1     -9.88
 8016.09c     -12.042
 8017.09c     -0.005
90232.09c     -76.456
94238.09c     -0.315
94239.09c     -5.959
94240.09c     -2.633
94241.09c     -1.747
94242.09c     -0.814

mat fuel2     -9.88
 8016.09c     -12.042
 8017.09c     -0.005
90232.09c     -76.456
94238.09c     -0.315
94239.09c     -5.959
94240.09c     -2.633
94241.09c     -1.747
94242.09c     -0.814

mat fuel3     -9.88
 8016.09c     -12.042
 8017.09c     -0.005
90232.09c     -76.456
94238.09c     -0.315
94239.09c     -5.959
94240.09c     -2.633
94241.09c     -1.747
94242.09c     -0.814


% --- Cladding SS310:

mat clad      -7.90
6000.09c     -0.034
14000.09c     -0.51
25055.09c    -0.74
15031.09c    -0.016
16000.09c    -0.0020
28000.09c    -20.82
24000.09c    -25.04
26000.09c    -51.738
42000.09c    -0.51
40000.09c    -0.59

mat clad2      -7.90
6000.06c     -0.034
14000.06c     -0.51
25055.06c    -0.74
15031.06c    -0.016
16000.06c    -0.0020
28000.06c    -20.82
24000.06c    -25.04
26000.06c    -51.738
42000.06c    -0.51
40000.06c    -0.59

% Liner Tube
mat liner      -7.90
6000.06c     -0.034
14000.06c     -0.51
25055.06c    -0.74
15031.06c    -0.016
16000.06c    -0.0020
28000.06c    -20.82
24000.06c    -25.04
26000.06c    -51.738
42000.06c    -0.51
40000.06c    -0.59

% Insulator Already Porous
mat ins     -1.29
40000.06c  -72.3
8016.06c   -27.6884985883
8017.06c   -0.0115014117

% --- Pressure tube:
```

```
mat Ptube      -6.52
40000.06c     -94.9
42000.06c     -0.8
50000.06c     -3.5
41093.06c     -0.8

% --- Coolant water:

mat cool      -0.59254     moder lwtrC 1001
1001.06c -0.111912491
8016.06c -0.887727175
8017.06c -0.000360

% --- Moderator water:

mat moder     -1.0851     moder lwtrM 1001 moder hwtrM 1002
 8016.03c     -0.7986846986
 8017.03c     -0.0003317624
 1002.03c     -0.200796688
 1001.03c     -0.000186851

% --- Thermal scattering data for light and heavy water:

therm lwtrC lwe7.12t
therm lwtrM lwe7.00t
therm hwtrM hwe7.00t

% --- Cross section data library file path:

set acelib "/home/michael/Desktop/SERPENT1.17/endfb7/sss_endfb7u.xsdata"
set powdens 29.2
set bc 2
set sym  0

set pop 5000 5000 300

% --- Geometry and mesh plots:

plot 3 500 500
mesh 3 500 500

% ------------------------------------------------------------------
%--------------------
% Detector in the FuelInner
%--------------------
det 1 dm fuel1  dr -6 void    % Total fission rate
det 2 dm fuel1  dr -7 void    % Total fission neutron production
det 3 dm fuel1  dr -8 void    % Total fission energy deposition (Power)

%--------------------
% Detector in the FuelMiddle
%--------------------
det 4 dm fuel2  dr -6 void    % Total fission rate
det 5 dm fuel2  dr -7 void    % Total fission neutron production
det 6 dm fuel2  dr -8 void    % Total fission energy deposition (Power)

%--------------------
% Detector in the FuelOuter
%--------------------
det 7 dm fuel3  dr -6 void    % Total fission rate
det 8 dm fuel3  dr -7 void    % Total fission neutron production
det 9 dm fuel3  dr -8 void    % Total fission energy deposition (Power)
```

E.2 Chapter 4 Input File

```
% --- SCWR cluster ------------------------------------------

set title "SCWR"

%k(Water) model
%10 insulator subregions
%Axial Position 0.5m

% --- Fuel pin:

pin 1
fuel1  0.62
clad  0.68
cool

pin 2
```

```
fuel2   0.62
clad   0.68
cool

pin 3
fuel3   0.35
clad   0.41
cool

pin 4
PINCEN 2.82
clad 2.88
cool

% ------------------
% Rings description
% ------------------
lat      10    4    0.0    0.0    1    % Central pin
1     0.0     0.0           4

lat      11    4    0.0    0.0    1    % Inner ring
15    3.66    15.0          1 1 1 1 1 1 1 1 1 1 1 1 1 1 1

lat      12    4    0.0    0.0    1    % Middle ring
21    5.11    10.0          2 2 2 2 2 2 2 2 2 2 2 2 2 2 2 2 2 2 2 2 2

lat      13    4    0.0    0.0    1    % Outer ring
42    6.30    7.5           3 3 3 3 3 3 3 3 3 3 3 3 3 3 3 3 3 3 3 3 3 3
                            3 3 3 3 3 3 3 3 3 3 3 3 3 3 3 3 3 3 3 3 3 3

% ------------------
% Cell description
% ------------------
surf 1   cyl   0.0   0.0     2.930    % Virtual surface
surf 2   cyl   0.0   0.0     4.385    % Virtual surface
surf 3   cyl   0.0   0.0     5.840    % Virtual surface
surf 4   cyl   0.0   0.0     6.800    % Liner tube inner radius
surf 5   cyl   0.0   0.0     6.850    % Liner tube outer radius / Insulator inner radius
surf 6   cyl 0.0 0.0 6.95000  % i-ii
surf 7   cyl 0.0 0.0 7.05000  % ii-iii
surf 8   cyl 0.0 0.0 7.15000  % iii-iv
surf 9   cyl 0.0 0.0 7.25000  % iv-v
surf 10   cyl 0.0 0.0 7.35000  % v-vi
surf 11   cyl 0.0 0.0 7.45000  % vi-vii
surf 12   cyl 0.0 0.0 7.55000  % vii-viii
surf 13   cyl 0.0 0.0 7.65000  % viii-ix
surf 14   cyl 0.0 0.0 7.75000  % ix-x
surf 15   cyl   0.0   0.0    7.850    % Insulator outer radius  / Pressure tube inner radius
surf 16   cyl   0.0   0.0     9.050    % Pressure tube outer radius
surf 17   sqc   0.0   0.0    12.500    % 25 cm square lattice pitch

cell 1 0 fill 10           -1  % Central pin
cell 2 0 fill 11        1  -2  % Inner ring
cell 3 0 fill 12        2  -3  % Middle ring
cell 4 0 fill 13        3  -4  % Outer ring
cell 5 0 liner          4  -5  % Liner tube
cell 6 0 ins            5  -6  % Insulator
cell 7 0 insii          6  -7
cell 8 0 insiii         7  -8
cell 9 0 insiv          8  -9
cell 10 0 insv          9  -10
cell 11 0 insvi         10  -11
cell 12 0 insvii        11  -12
cell 13 0 insviii       12  -13
cell 14 0 insix         13  -14
cell 15 0 insx          14  -15
cell 16 0 Ptube          15  -16  % Pressure tube
cell 17 0 moder          16  -17  % Moderator
cell 18 0 outside        17      % Outside world

% PINCEN

mat PINCEN  -5.83
40000.06c  -66.63
39089.06c  -7.87
8016.06c  -25.4897
8017.06c  -1.03E-2

% --- Fuel (Pt/Th Mixture):

mat fuel1     -9.88
 8016.09c     -1.21E+1
 8017.09c     -4.87E-3
90232.09c     -7.65E+1
94238.09c     -3.15E-1
94239.09c     -5.96E+0
94240.09c     -2.63E+0
```

```
94241.09c     -1.75E+0
94242.09c     -8.14E-1

mat fuel2     -9.88
 8016.09c     -1.21E+1
 8017.09c     -4.87E-3
90232.09c     -7.65E+1
94238.09c     -3.15E-1
94239.09c     -5.96E+0
94240.09c     -2.63E+0
94241.09c     -1.75E+0
94242.09c     -8.14E-1

mat fuel3     -9.88
 8016.09c     -1.21E+1
 8017.09c     -4.87E-3
90232.09c     -7.65E+1
94238.09c     -3.15E-1
94239.09c     -5.96E+0
94240.09c     -2.63E+0
94241.09c     -1.75E+0
94242.09c     -8.14E-1

% --- Cladding SS310:

mat clad      -7.90
6000.06c     -0.034
14000.06c     -0.51
25055.06c    -0.74
15031.06c    -0.016
16000.06c    -0.0020
28000.06c    -20.82
24000.06c    -25.04
26000.06c    -51.738
42000.06c    -0.51
40000.06c    -0.59

% Liner Tube
mat liner    -2.482644 moder lwtrC 1001
6000.06c     -0.034
14000.06c    -0.51049
25055.06c    -0.73999
15031.06c    -0.016
16000.06c    -0.002
28000.06c    -20.8236
24000.06c    -25.0835
26000.06c    -51.69
42000.06c    -51.009
40000.06c    -0.59039
8016.06c     -4.21929
8017.06c     -0.00171
1001.06c     -0.53191

% Insulator Already Porous
mat ins     -1.6872952407 moder lwtrC 1001
40000.06c  -66.616461797
39089.06c  -7.870763464
8016.06c  -43.7807737795
8017.06c  -0.017720275
1001.06c  -2.304277875

mat insii   -1.8528350215 moder lwtrC 1001
40000.06c  -66.616461797
39089.06c  -7.870763464
8016.06c  -54.2835011945
8017.06c  -0.0219833974
1001.06c  -3.6283179857

mat insiii  -1.9032205999 moder lwtrC 1001
40000.06c  -66.616461797
39089.06c  -7.870763464
8016.06c  -57.4802312638
8017.06c  -0.02328097
1001.06c  -4.0313179559

mat insiv   -1.9369873184 moder lwtrC 1001
40000.06c  -66.616461797
39089.06c  -7.870763464
8016.06c  -59.6225721505
8017.06c  -0.0241505595
1001.06c  -4.3013949705

mat insv    -1.9630687575 moder lwtrC 1001
40000.06c  -66.616461797
39089.06c  -7.870763464
8016.06c  -61.2773178771
8017.06c  -0.0248222311
```

```
1001.06c -4.5100026615

mat insvi   -1.9845730478 moder lwtrC 1001
40000.06c -66.616461797
39089.06c -7.870763464
8016.06c -62.6416648564
8017.06c -0.0253760281
1001.06c -4.6820008534


mat insvii -2.0030047954 moder lwtrC 1001
40000.06c -66.616461797
39089.06c -7.870763464
8016.06c -63.8110733161
8017.06c -0.0258506982
1001.06c -4.8294238651


mat insviii -2.019210589 moder lwtrC 1001
40000.06c -66.616461797
39089.06c -7.870763464
8016.06c -64.8392553736
8017.06c -0.0262680437
1001.06c -4.9590429851


mat insix   -2.0337141368 moder lwtrC 1001
40000.06c -66.616461797
39089.06c -7.870763464
8016.06c -65.7594378755
8017.06c -0.0266415515
1001.06c -5.0750469995


mat insx    -2.0468620771 moder lwtrC 1001
40000.06c -66.616461797
39089.06c -7.870763464
8016.06c -66.5936133951
8017.06c -0.0269801486
1001.06c -5.1802084307



% --- Pressure tube:

mat Ptube      -6.52
40000.03c     -94.9
42000.03c     -0.8
50000.03c     -3.5
41093.03c     -0.8

% --- Coolant water:

mat cool      -0.16092     moder lwtrC 1001
 8016.06c     -0.8884464
 8017.06c     -0.0003606
 1001.06c     -0.111912

% --- Moderator water:

mat moder     -1.0851     moder lwtrM 1001 moder hwtrM 1002
 8016.03c     -79.857086
 8017.03c     -0.0324145
 1002.03c     -2.01016E+1
 1001.03c     -8.96000E-3

% --- Thermal scattering data for light and heavy water:

therm lwtrC lwe7.12t
therm lwtrM lwe7.00t
therm hwtrM hwe7.00t

% --- Cross section data library file path:

set acelib "/home/michael/Desktop/SERPENT1.17/endfb7/sss_endfb7u.xsdata"
set bc 2
set sym  0

% --- Neutron population and criticality cycles:
set pop 5000 5000 300

% --- Geometry and mesh plots:
plot 3 500 500
mesh 3 500 500

% ------------------------------------------------------------
%------------------
```

```
% Detector in the FuelInner
%-----------------
det 1 dm fuel1  dr -6 void    % Total fission rate
det 2 dm fuel1  dr -7 void      % Total fission neutron prodection
det 3 dm fuel1  dr -8 void    % Total fission energy deposition (Power)

%-----------------
% Detector in the FuelMiddle
%-----------------
det 4 dm fuel2  dr -6 void    % Total fission rate
det 5 dm fuel2  dr -7 void    % Total fission neutron prodection
det 6 dm fuel2  dr -8 void    % Total fission energy deposition (Power)

%-----------------
% Detector in the FuelOuter
%-----------------
det 7 dm fuel3  dr -6 void    % Total fission rate
det 8 dm fuel3  dr -7 void      % Total fission neutron prodection
det 9 dm fuel3  dr -8 void    % Total fission energy deposition (Power)
```

Appendix F

Other Programs Used

mini-REFPROP is a sample program of REFPROP, which is intended as a teaching aide for thermodynamic properties. It contains properties for a number of pure fluids, and is used here to provide the properties of super-critical water at a high precision [44]. It provides the thermal conductivity, density and temperature for water, even in the supercritical transitional regions to a high degree of accuracy. It is provided by the National Institute of Standards and Technology, and uses a NIST database as reference for the data.[44].

FlexPDE 5.0 is multi-purpose software for calculating numerical solutions to partial differential equations. It is used in this thesis to solve the second-order Ordinary Differential Equations in Chapter 4.1 [45]. It is used to obtain a numerical solution using the discrete output from mini-REFPROP to generate a fine result with 401 points from $r = 6.85$cm to $r = 7.85$cm.